DEVELOPMENT OF UBIQUITIN VARIANTS WITH SELECTIVITY FOR THE UBIQUITIN C-TERMINAL HYDROLSE SUBFAMILY OF DEUBIQUITINASES

by

Chad Steven Hewitt

A Dissertation

Submitted to the Faculty of Purdue University

In Partial Fulfillment of the Requirements for the degree of

Doctor of Philosophy

Department of Medicinal Chemistry and Molecular Pharmacology

West Lafayette, Indiana

December 2021

THE PURDUE UNIVERSITY GRADUATE SCHOOL
STATEMENT OF COMMITTEE APPROVAL

Dr. Daniel P. Flaherty, Chair

Department of Medicinal Chemistry and Molecular Pharmacology

Dr. Darci J. Trader

Department of Medicinal Chemistry and Molecular Pharmacology

Dr. Jean-Christophe Rochet

Department of Medicinal Chemistry and Molecular Pharmacology

Dr. Chittaranjan Das

Department of Chemistry

Approved by:

Dr. Andy Hudmon

To my family Steve, Martine, Evan, Carly, and Shane (along with Fletcher and Ninja) – Thank you for all your love and support throughout the years.

To the many friends I have had the opportunity to meet – Thank you for all the scientific (and non-scientific) discussions. They have helped immensely in collecting data and writing throughout my graduate school as well as aided getting me through the tough times. I will forever be grateful.

To my mentor, Daniel P. Flaherty, thank you for the continual support, great mentorship, and allowing me the opportunity to supplement my graduate school experience with career development outside of science.

To my girlfriend, Lauren Orr, thank you for all the scientific discussions about PROTACs and amide couplings. Love you! :)

TABLE OF CONTENTS

LIST OF TABLES

LIST OF FIGURES

ABBREVIATIONS

ABP – Activity based probe

AD – Alzheimer's disease

ATP – Adenosine triphosphate

BAP1 – BRCA 1 associated protein

BCA – Bicinchoninic acid

BLI – Biolayer interferometry

C90A – Cysteine 90 to alanine mutation

CI – Confidence interval

CSF – Cerebrospinal fluid

DIPEA – N, N-Diisopropylethylamine

DMEM – Dulbecco's Modified Eagle Medium

DMF – Dimethylformamide

DMSO – Dimethyl sulfoxide

DTT – Dithiothreitol

DUB – Deubiquitinase

E. coli – Escherchia coli

EDTA – Ethylenediaminetetraacetic acid

FBS – Fetal bovine serum

FDA – Food and Drug Administration

FMK – Fluoromethylketone

H_2O – Water

HA – Hemagglutinin

HA-Ub-VME – Hemagglutinin-tagged ubiquitin vinylmethylester

IC_{50} – Half-maximal inhibition concentration

IPTG – Isopropyl β-d-1-thiogalactopyranoside

JAMM – Jab1/Mov34/Mpr1 Pad1 N-terminal+

KCl – Potassium Chloride

K_d – Dissociation constant

K_I – Inhibition constant

k_{inact} – Rate of inactivation at saturation

k_{obs} – Observed rated of inactivation

MD – Molecular Dynamics

MeOH – Methanol

MESNa – 2-ethanesulfonic acid sodium salt

mg – Milligram

$MgCl_2$ – Magnesium Chloride

MINDY – motif interacting with Ub-containing novel DUB family

MJD – Machado-Josephin domain

mM Millimolar

MM-GBSA – Molecular mechanics - generalized Born and surface area

mmol – Millimoles

mTOR – Mammalian target of Rapamycin

MW – Molecular weight

Na_2SO_4 – Sodium sulfate

NaCl – Sodium Chloride

$NaHCO_3$ – Sodium Bicarbonate

NaOH – Sodium hydroxide

Ni-NTA – Nickel nitriloacetic acid

nM – Nanomolar

NP-40 – Nonidet P-40

NSCLC – Non-small cell lung cancer

OTU – Ovarian Tumor Protease

PBS – Phosphate buffered saline

PD – Parkinson's disease

PDB – Protein Data Bank

ppm – Parts per million

PRG – Propargylamine

R_g – Radius of Gyration

SAR – Structure-activity relationship

SCLC – Small cell lung cancer

SDS – Sodium dodecyl sulfate

SDS-PAGE – Sodium dodecyl sulfate – gel electrophoresis

TBS – Tris buffered saline

tBuOH – Tert-butyl alcohol

TCEP – Tris(2-carboxyethyl)phosphine

TFA – Trifluoroacetic acid

TIPS – Triisopropylsilane

TMS – Tetramethylsilane

TNBC – Triple negative breast cancer

TRIS – Tris(hydroxymethyl)aminomethane

Trt – Triphenylmethyl

Ub – Ubiqutin

Ub-AMC – Ubiquitin aminomethyl coumarin

Ub-Rho – Ubiquitin Rhodamine 110G

Ub-VME – Ubiquitin Vinylmethylester

UbV – Ubiquitin variant

UCH – Ubiquitin C-terminal Hydrolase

UCHL1 – Ubiquitin C-terminal Hydrolase L1

UCHL3 – Ubiquitin C-terminal Hydrolase L3

UCHL5 – Ubiquitin C-terminal Hydrolase L5

UPS – Ubiquitin Proteasome System

USP – Ubiquitin specific protease

UV – Ultraviolet

VAEFMK – Benzyloxycarbonyl-Val-Ala-Glu(gamma-methoxy)-fluoromethylketone

VME – Vinylmethylester

WT – Wild type

ZUFSP – Zinc finger containing ubiquitin peptidase 1

µM – Micromolar

ABSTRACT

There are over 100 deubiquitinating enzymes (DUBs) that account for seven distinct DUB subfamilies, each having different functions and binding topology to ubiquitin. One of these subfamilies, the ubiquitin C-terminal hydrolases (UCHs), contain four DUBs including the two structurally homologous enzymes UCHL1 and UCHL3. Both UCHL1 and UCHL3 have been described as cancer targets in literature, however development of small molecule probes to study their enzymatic activity in cancerous disease states remains difficult due to active site similarities between not only the UCHs but also all DUBs. This necessitates a novel method of probe development for DUBs. Due to this need, the endogenous substrate, ubiquitin has been utilized to develop macromolecular based probes for DUB enzymes.

UCHL1 and UCHL3 have an intrinsically high binding affinity for ubiquitin, which our lab utilized to our advantage in designing selective mono-ubiquitin variants (UbVs) and UbV-activity based probes containing mutations at amino acid residue sites that perturb binding to other DUBs were designed. Structural data, computational methods, as well as previous literature precedent on UbVs developed for other DUB subfamilies were utilized to derive highly selective mono-UbV for UCHL1 (Chapter 2), a UCHL1/UCHL3 UbV-activity based probe (Chapter 2), as well as a highly selective UbV-activity based probe for UCHL3 (Chapter 3).

Mechanistic studies were completed on Ub:UCHL1 complex formation and provide a novel interpretation of Ub:DUB binding as a whole as the negatively charged catalytic cysteine residue may be providing electrostatic repulsion to the negatively charged C-terminus of Ub post cleavage (Chapter 4). While development of a selective small molecule inhibitor for UCHL1 has proven difficult, a UCHL1 peptide-based inhibitor VAEFMK has yet to be characterized. VAEFMK and analogs display selectivity toward UCHL1 over UCHL3 but require high concentrations to fully inhibit UCHL1 in cells (Chapter 4). Conclusions and future directions to research on the ubiquitin variant projects will be presented in Chapter 5.

CHAPTER 1. INTRODUCTION

1.1 Overview of Ubiquitin and Ubiquitin-Proteasome Pathway

Protein function, structure, and distribution in cells is often regulated by post translational modifications (PTMs). One such PTM, ubiquitination, involves the addition of a 76 amino acid signaling protein, ubiquitin (Ub), to substrate proteins via E1, E2, E3 enzymatic cascade. E1 enzymes are responsible for activating Ub through an ATP-dependent process.[1–3] The Ub protein is then transferred to an E2 conjugating enzyme, which subsequently binds to an E3 ligase enzyme that in turn mediates or directly catalyzes the transfer of Ub to the substrate protein. The result of this enzymatic cascade is a mono-ubiquitinated substrate protein containing an isopeptide bond between the C-terminus of Ub and a lysine residue on the substrate protein. Ub itself contains seven lysine residues and one N-terminal methionine residue (Figure 1.1) on which the E1, E2 and E3 cascade can attach additional Ubs to yield poly-ubiquitinated branched (different linkage points on Ub) or linear (same linkage points on Ub) chains.[4] The branched and linear Ub chain architectures confer different physiological roles, such as protein trafficking, protein degradation, cell cycle progression, DNA damage response, and chromatin remodeling.

Although the function of many poly-ubiquitinated Ub chains have not been rigorously studied, a few canonical descriptions of the function of poly-ubiquitinated states exist. For example, linear chains of Ub linked via K48 is primarily a signal for proteolysis through the proteasome.[5] Additionally, K63 Ub linear chains are associated with DNA damage response and NF-κB signaling.[6,7] Branched chains with known physiological function include K11/K48, K29/K48, and K48/K63.[8] K11/K48 branched chains bestow proteolytic function on substrate proteins. Branched K48/K63 chains play a role in NF-kB signaling.[9]

1.1.1 Monoubiquitin Structure

The ubiquitin monomer is a 76 amino acid protein consisting of an alpha helix, a short 3_{10} helix, and a mixed beta-sheet that contains five strands and seven reverse turns.[10] Ub's core structure consists of a beta-grasp fold also known as a ubiquitin like fold. Monoubiquitin is generally recognized through a hydrophobic surface that consists of Leu8, Ile44, His68, and Val70. As previously mentioned, the seven lysine residues as well as one N-terminal methionine serve as

sites of polymerization of Ub chains. Except for K27, all other residues are surface exposed with K6 and K27 located on the most dynamic portions of the Ub monomer (Figure 1.1).

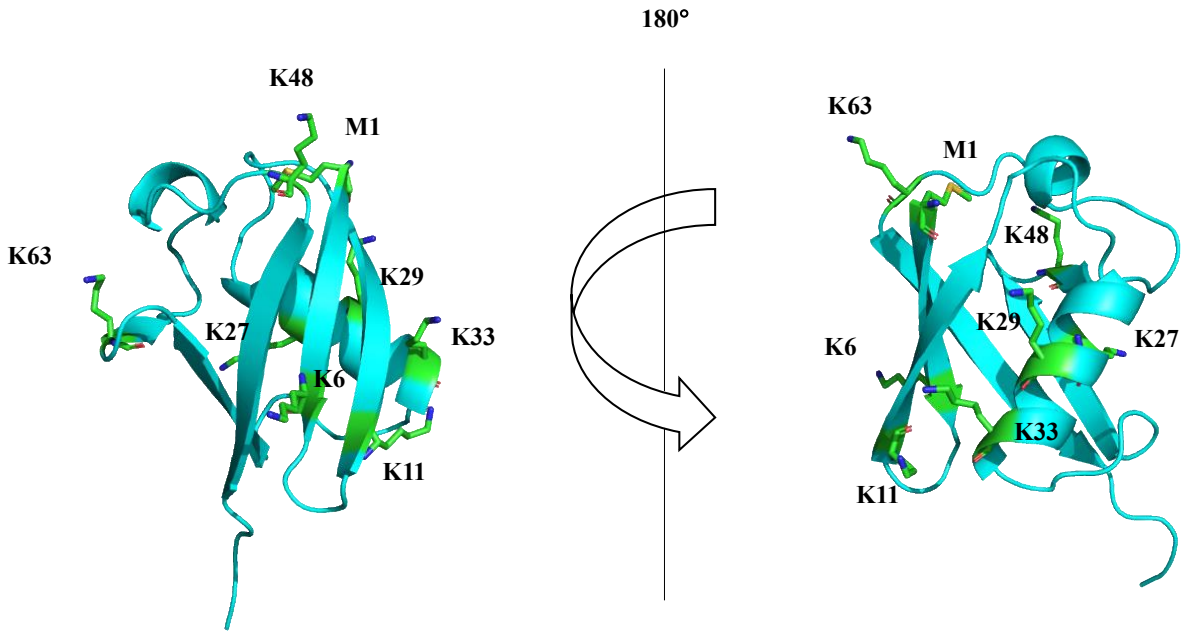

Figure 1.1 Ubiquitin Structure.Methionine and lysine residues where ubiquitin chains can be polymerized by the E1, E2, E3 ligase cascade. Modified from PDB: 1UBQ.

1.1.2 Polyubiquitin Chain Conformations

Polyubiquitinated chains adopt different conformations depending on the linkages and surrounding conditions. These conformations are typically described as compact or open. K48, K6, and K11 linked chains form compact conformations, where distal residues on Ub subunits interact with each other.[11–17] M1 and K63 form open conformations where the only interaction is the isopeptide bond formed by the E3 ligase.[18–20] The linkages and conformations of poly-Ub chains affect their recognition by various enzymes, including many deubiquitinating enzymes (DUBs, the general enzymatic class discussed in this thesis) and downstream effects on the substrate protein.

1.2 Overview of Deubiquitinating Enzymes

Deubiquitinating enzymes (DUBs) regulate substrate proteins in the cellular environment by removing Ub from mono and poly-ubiquitinated chains on these proteins. In total there are over 100 DUBs expressed in the human proteome. Each DUB falls into one of seven different subfamilies that have been identified based on their activity, recognition, domains present, and topological interaction with mono or poly Ub chains. These subfamilies include ubiquitin specific proteases (USPs), ubiquitin C-terminal hydrolases (UCHs), Machado Josephin domain proteases (MJDs), ovarian tumor proteases (OTU), Jab1/MPN domain- associated metalloisopeptide (JAMM) proteases, and the recently identified ZUP1 and MINDY subfamilies.[21–23] Most of these enzymes are cysteine proteases with the exception for the JAMM proteases, which require a metal cofactor for their activity.

Research studies on several DUB subfamilies have been performed to elucidate their ubiquitin linkage/substrate protein specificity. The USPs, which make up >50% of all DUBs, are largely non-specific to Ub linkages but are selective for certain substrate enzymes.[24,25] In contrast, JAMM proteases are selective for K63 linkages.[26]

The UCH subfamily consists of four members, each having an N-terminal C12 peptidase domain formed from: 1) a knotted backbone, 2) a C-terminal extension, and 3) an unstructured loop that limits access to the active site.[27] The topic of this thesis will focus on developing ubiquitin-based mutant probes selective for two homologous DUBs in the UCH subfamily, Ubiquitin C-Terminal Hydrolase 1 (UCHL1) and Ubiquitin C-Terminal Hydrolase 3 (UCHL3), which will be discussed below.

1.3 Ubiquitin C-Terminal Hydrolase L1 (UCHL1) Structure, Function, and Distribution

Ubiquitin C-Terminal Hydrolase L1 (UCHL1) is a 223 amino acid DUB primarily expressed in the central nervous system where it makes up 1-5% of the soluble protein.[28,29] The five crossings of the C12 polypeptide backbone form a 5_2 knot, which is thought to have evolved to protect the enzyme from proteasomal unfolding and degradation.[29] The active site consists of a catalytic triad (His161, Asp176, and Cys90). The Asp176 stabilizes the His161, which deprotonates the Cys90 when in an active conformation. In the apo-structure of UCHL1 (PDB: 2ETL) the distance between His161 and Cys90 is approximately 8 Å, which is too far for the His

to deprotonate the catalytic Cys (Figure 1.2A).[30] This results in apo-UCHL1 residing in an inactive conformation. X-ray crystallography studies (PDB: 3KW5), as well as molecular dynamic simulations, have shown that upon Ub-binding to UCHL1 the protein-protein interaction (PPI) sets off a cross-talk of two UCHL1 phenylalanine residues, Phe214 and Phe53, that subsequently push His161 closer to Cys90 rendering the active conformation (Figure 1.2B).[30,31]

UCHL1 is primarily expressed in the central nervous system (CNS) under normal physiological conditions.[28,29] Thus, the physiological effects of point mutations and post translational modifications that have been identified in UCHL1 that lead to alterations in disease progression have affected the CNS. For example, UCHL1 Glu7Ala causes early onset neurodegeneration and was shown that Glu7 on UCHL1 is required for binding to Ub.[32] Additionally, the UCHL1 Ile93Met mutation an autosomal dominant genetic variant and is thought to lead to early-onset Parkinson's disease known as *PARK5*.[10] The crystal structure of the Ile93Met mutant (PDB: 3IRT) maintains the same structural features as wild-type yet has a reduced catalytic efficiency.[30,33] The exact mechanism for how the UCHL1 Ile93Met mutation mediated early onset PD is not yet known although it is hypothesized to be through a toxic gain of function.[34,35, 36] UCHL1 Ser18Tyr mutation appears to exhibit neuroprotective effects.[37] Moreover, traumatic head injury studies have shown UCHL1 can be modified by injury factors such as cyclopentenone prostaglandins and 4-hydroxynonenal oxidative modification of Cys152 leads to loss of solubility.[38,39] These PTMs may also contribute to cell death after brain injury.

Another structural component on UCHL1 that appears to play a role in substrate selectivity is the presences of a ~10 amino acid loop that crosses over the active site (Figure 1.2). This is believed to restrict access to the active site and limits the size of UCHL1 substrate proteins. Substrates that have been hypothesized for UCHL1 largely consist of small C-terminal adducts that are capable of fitting into the active site. Additionally, the strength of the Ub-UCHL1 PPI is among the strongest for Ub with any other interacting partner; thus, under normal physiological conditions UCHL1 is thought to serve as a sink to stabilize the intracellular pool of mono-Ub.[40,35,41]

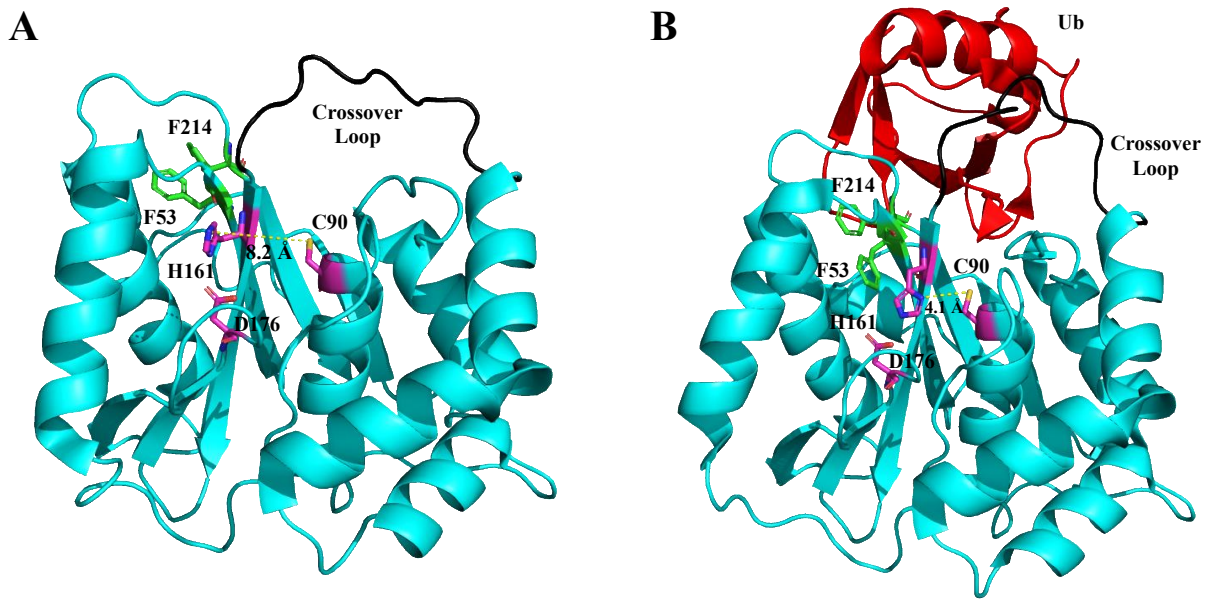

Figure 1.2 Ubiquitin C-terminal Hydrolase L1 Structure in A) inactive apo state and B) active Ub bound state. Residues comprising the catalytic triad are colored magenta, with the cross talking phenylalanine residues colored green and the crossover loop colored black. Modified form PDB structure 2ETL and 3KW5, respectively.

1.3.1 UCHL1 in Cancer

While UCHL1 is primarily expressed in the CNS under normal physiological conditions it can also have a role in disease progression in the periphery. UCHL1 is observed to be an oncogene in many cancers including glioma[42], B-cell lymphoma[43,44], and small and non-small cell lung cancer[45,46]. Transgenic mice expressing UCHL1 outside of the CNS exhibit heavy spontaneous lymphoma and lung tumor burden.[44] UCHL1 has been shown to be required for MYC-driven lymphomas.[47] It has been determined that UCHL1 abrogates HIF-1α ubiquitination leading to development of metastasis in murine pulmonary cancer models.[48] Also, UCHL1 antagonizes the ubiquitination of raptor by destabilizing the DDB1-CUL4 E3 ubiquitin ligase complex. This in turn leads to deregulation of mTORC1 and mTORC2 levels leading to increases in malignancy.[49] In addition, UCHL1 promotes the AKT pathway by directly binding to AKT2 and activating cancer invasion pathways in the MCF-7 breast cancer cell model.[50] UCHL1 also promotes cancer cell invasion by up-regulating hydrogen peroxide levels via deubiquitination of NADPH oxidase 4.[51]

While it is known the UCHL1 is an oncogene for many cancers, in ovarian and prostate cancer, there is evidence of UCHL1 being both a tumor suppressor and a tumor promoter. For instance, methylation

of the promoter region and therefore silencing of the UCHL1 gene was observed in seven ovarian cancer cell models.[52] In the same study, inhibition of UCHL1's activity promoted ovarian cancer cell proliferation.[52] However, in high-grade serous ovarian cancer, UCHL1 inhibition reduced cell proliferation, invasion, and metastatic growth in in vivo xenograft models.[53] In a prostate cancer context, high UCHL1 levels display p53 accumulation due to upregulation of p14ARF.[54] p14ARF decreases the activity of MDM E3 ubiquitin ligase which decreases degradation of MDM's known substrate p53. However, UCHL1 has also displayed expression-linked increases in epithelial to mesenchymal transition (EMT) in prostate cancer.[55] These results could be indicative of UCHL1 having a differential effect depending on the stage of the cancer.

1.3.2 UCHL1 Small Molecule Inhibitors

UCHL1's prominent role in cancer necessitates the development of small molecule inhibitors as molecular probes. A high throughput screen was conducted in 2003 using the fluorogenic substrate Ub-aminomethylcoumarin (Ub-AMC) and a library of small molecules against UCHL1.[56] A series of isatins with single digit micromolar inhibition constants against UCHL1 were discovered and through optimization, LDN-57444 was developed (Figure 1.3). This compound was shown to be a competitive inhibitor that bound to UCHL1's active site and had 28-fold selectivity for UCHL1 (IC_{50} = 0.88 μM, K_I = 0.40 μM) over UCHL3.

LDN-57444 has been the gold standard UCHL1 inhibitor since its discovery and used in >100 peer-reviewed papers. However, questions on the reliability of data generated from use of this inhibitor have been raised. In our lab's hands, LDN-57444 is unable to inhibit UCHL1 in biochemical assays.[57,28] Additional experiments indicated that LDN-57444 degraded over 30 minutes in Dulbecco's Modified Eagle Medium (DMEM), suggesting that this inhibitor is unstable during cell treatments and likely has off target effects (data not shown). Therefore, the use of LDN-57444 should receive more scrutiny and data generated with this inhibitor could very well be confounding.

LDN-91946 was developed from molecules in the same high throughput screen as LDN-57444, but the mechanism for its inhibition was not published until 2007.[58] This inhibitor has a 7 fold selectivity window for UCHL1 (K_I = 2.8 μM) over UCHL3 and was determined to bind to the Michaelis complex of the UCHL1 enzyme through steady state kinetics experiments, providing ample evidence toward a new inhibitory mechanism for UCHL1.

Although reversible inhibitors work well for a majority of DUBs that have binding affinities for Ub in the micromolar range, UCHL1 has one of the tightest K_ds with Ub among all DUBs at around 140 nM and thus necessitating a very high binding affinity reversible inhibitor to out compete Ub and inhibit UCHL1.[31,41] Thus, covalent modification of UCHL1's active site cysteine has received attention as an alternative strategy to inhibit the DUB. The co-crystal structure with a covalent inhibitor Z-VAE(OMe)-Fluoromethyl ketone (VAEFMK) bound to UCHL1's active site cysteine was published in 2012.[59] This inhibitor was discovered serendipitously in a high throughput counter screen against a viral cysteine protease and was counter screened against UCHL1 and was shown to inhibit. Follow-up assays demonstrated VAEFMK was selective over UCHL3 and UCHL5.

Cyanopyrrolidine inhibitors have gained traction as covalent inhibitors against UCHL1 in recent years.[60,61] Mission Therapeutics submitted patents on this class of inhibitors toward UCHL1, but these patents lacked any inhibition data in cellular assays and biochemical contexts.[62,63]. Building off of these, our group and others developed and characterized second generation cyanopyrrolidine inhibitors.[60,61]. Although the one developed by our group does display some off target effects, the inhibitor developed by Panyain et al. does display in vivo selectivity toward the UCHL1 target.[61]

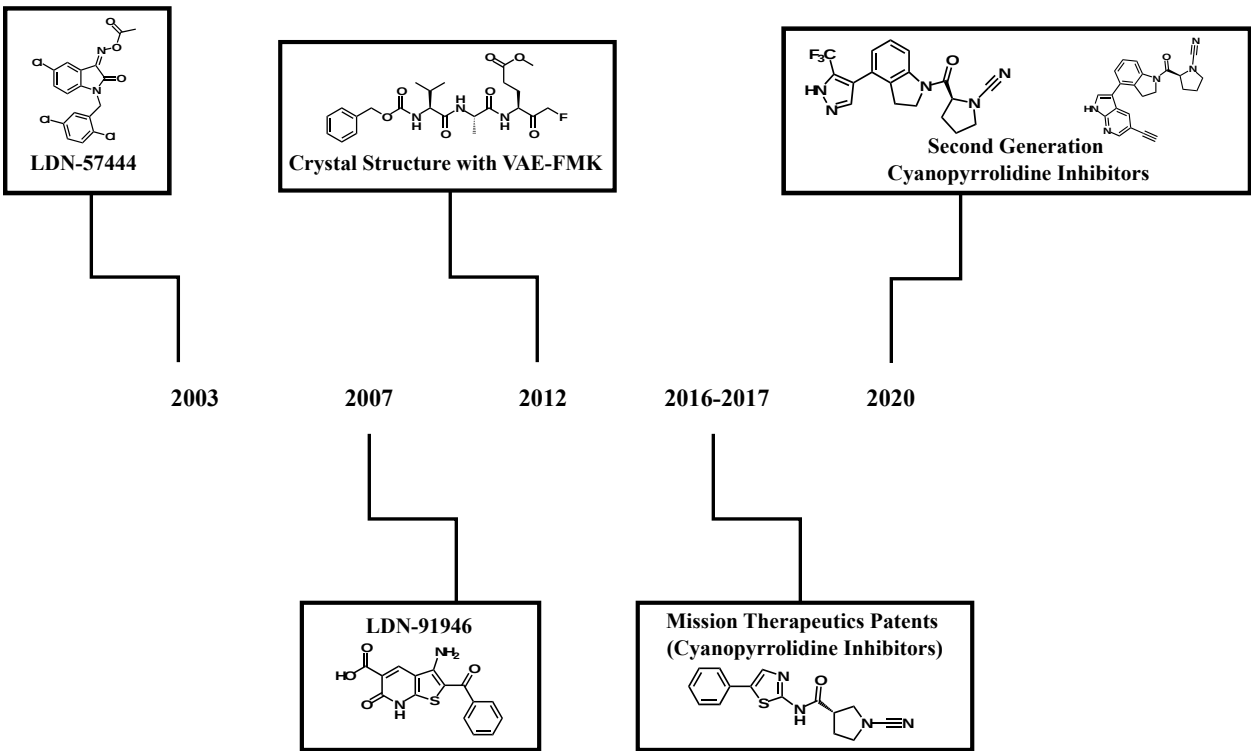

Figure 1.3 UCHL1 Small Molecule Inhibitor Timeline

1.4 Ubiquitin C-Terminal Hydrolase L3 (UCHL3) Structure, Distribution, and Function

Ubiquitin C-terminal hydrolase L3 (UCHL3) is a 230 amino acid protein that has a high degree of structural homology to UCHL1. The catalytic triad of this enzyme consists of Cys95, His169, and Asp184. UCHL3 contains a longer crossover loop ~20 amino acids, similar to the smaller crossover loop present in UCHL1. UCHL3's catalytic triad remains in an active state due to the proximity of the His 169 and Cys95 in the apo and Ub-bound UCHL3 structures, which have been reported (PDB: apo 1UCH and Ub-bound 1XD3, respectively). This contributes to the relatively high UCHL3 cellular and recombinant activity of the protein in comparison to UCHL1.

The apo-UCHL3 and the Ub-bound UCHL3 structural data also allow for analysis of conformational changes that occur upon Ub binding.[64,65] The apo-structure shows the crossover loop as unstructured and is therefore unresolved, but the Ub-bound structure contains a resolved structure for the crossover loop suggesting there is more stability for the crossover loop when Ub is bound. Therefore, using these crystal structures along with computational docking of Ub, a proposed mechanism of catalysis can be ascertained. In this mechanism the crossover loop is pushed away upon Ub substrate binding. This allows the catalytic triad to perform catalysis and enter into a Ub bound state. After catalysis, the conformation of the crossover loop changes into a locked state as was solved in the 1XD3 crystal structure (Figure 1.4) in which the Ub protein is freed from UCHL3 at the end of the catalytic reaction. However, the internal diameter of the crossover loop is ~ 15 angstroms, and this space does not account for large, structured substrates on which Ub is cleaved.

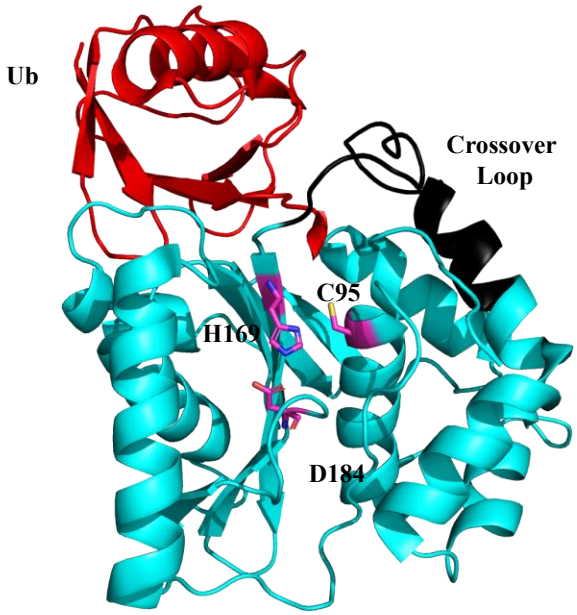

Figure 1.4 UCHL3 Ub-Bound Structure (PDB: 1XD3)

1.4.1 UCHL3 in Cancer

The role of UCHL3 in cancer is only recently being investigated. UCHL3 overexpression has been implicated in numerous cancers for the hypothesized role in augmenting DNA repair pathways. Specifically, UCHL3 has been identified as a deubiquitinase that controls the

proteostasis of tyrosyl DNA phosphodiesterase 1 (TDP1), the enzyme responsible for hydrolyzing the covalent bond between type 1 topoisomerases (TOP1) and the 3-prime phosphate of DNA.[66] Depletion of UCHL3 in rhabdomyosarcoma cells markedly reduced the levels of TDP1 as well as sensitizing the cells to TOP1 poisons. UCHL3 has additionally been implicated in DNA double stranded break repair pathway by deubiquitinating Ku proteins, which sense broken DNA by binding to chromatin and helping to initiate non-homologous end joining (NHEJ).[67] Ubiquitination of Ku proteins is important for Ku protein removal from chromatin after NHEJ has completed. Reduced levels of UCHL3 sensitized cells to ionizing radiation and decreased NHEJ efficiencies in an osteosarcoma model system. Other examples include findings from a recent paper that UCHL3 is responsible for deubiquitinating lymphoid-specific helicase (LSH), a chromatin modifier, linked to migration, invasion, and tumor formation in non-small cell lung cancer (NSCLC).[68] Furthermore, overexpression of UCHL3 has also been seen in breast cancer and is well correlated with poor survival rates.[69] Additionally, UCHL3 deubiquitinates and therefore stabilizes forkhead box M1 (FOXM1), a key transcription factor and regulator of cell cycle progression in pancreatic cancer leading to cancer progression.[70] Finally, UCHL3 overexpression has been shown to promote ovarian cancer by stabilizing TRAF2 to activate the NF- κB inflammation signaling pathway, leading to poor prognosis for patients.[71,72]

1.4.2 UCHL3 Small Molecule Inhibitors

While UCHL3 is growing in potential importance relating to cancer, there have been only two small molecule inhibitors reported in the literature (Figure 1.5). The first reported UCHL3 inhibitor 4,5,6,7-Tetrachloro-1*H*-Indene-1,3(2*H*)-dione, or TCID, was identified serendipitously in a high throughput screen to inhibit UCHL3.[56] However, this was only demonstrated *in vitro* and the molecule has not been fully validated to inhibit UCHL3 in cells. More recently, perifosine has been suggested to inhibit UCHL3 in breast cancer cell lines.[72] However, this effect was demonstrated by deubiquitination of the protein RAD51 in cells by Ub-immunoblot and did not show on-target engagement of perifosine with UCHL3.[72,73] Furthermore, the molecule does not inhibit UCHL3 *in vitro* in the standard Ub-AMC enzymatic assays. Based on the lack of UCHL3 chemical probes with validated on-target activity in cells there is a clear need for an alternative strategy to elucidate UCHL3 activity in cancer.

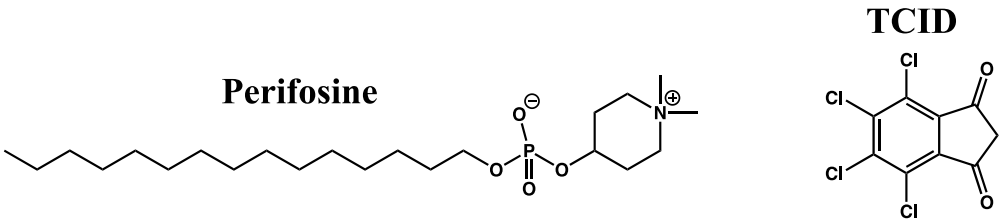

Figure 1.5 UCHL3 Small Molecule Inhibitors

1.5 Introduction to Ubiquitin Variants

With the lack of effective small molecule inhibitors for UCHL1 and UCHL3, a novel method for inhibition and probing of these enzymes is necessary to decipher their roles in cancer and other disease states. One alternative approach would be to employ Ub as the "hit" molecule and design variants of the protein to bind selectively to DUBs. These variants have been demonstrated to have utility in elucidating complex pathways involving other DUB isoforms and used as activity-based probes. Yet this approach has never been applied to UCH family DUBs such as UCHL1 or UCHL3.

1.5.1 Ubiquitin Variant History

Deciphering the role DUBs play in both normal and disease states is of enormous interest. DUB inhibitor development has been slow resulting in a need to identify alternative strategies to probe the enzymes in cellular and disease-relevant contexts.[63,74–76] Sachdev Sidhu's lab published a seminal manuscript which provided a novel strategy for manufacturing selective DUB inhibitors by modifying residues of the ubiquitin protein, leveraging the non-conserved residues on DUB enzymes that contribute to Ub binding.[77] The paper focuses on development of selective ubiquitin mutants (called ubiquitin variants or UbVs) by phage display for the USP subfamily of DUBs (USP8, USP21, and USP2a specifically), although UbVs selective for both OTUB1, an OTU DUB, and BRISC protein complex, a JAMM DUB were also isolated.

Around the same time, Genentech utilized phage display and computational design of UbVs and focused on mutating the core of the Ub protein to stabilize the conformation of the protein to make it selective for USP7.[41] Both laboratories identified UbVs *in vitro* and confirmed binding affinity to the targets of interest as well as selectivity over other DUBs. After these studies were published, efforts were underway to utilize phage-display to generate selective UbVs for various DUBs, mostly USPs. In 2016 Sachdev Sidhu revealed common Ub hotspots for binding to USP2

and USP21.[78] In that same year, Zhihao Zhuang's group revealed divergence in ubiquitin interaction and catalysis among USPs.[79] In 2017 Sachdev Sidhu's group generated selective UbV inhibitors for USP7 and USP10.[80] In 2019 that same group characterized UbV inhibitors of USP15.[81] Even with this advancement in probing technology for DUBs there were still limitations in the approach as variants needed to be used in cell lysates or plasmids carrying the new UbV needed to be transfected into cells and overexpressed. Nonetheless, UbV provided avenues for probing DUBs that had previously been undruggable.

1.5.2 Ubiquitin Variants as Chemical Tools

Huib Ovaa and colleagues expanded on this USP7 selective UbV and generated one of the first selective DUB UbV activity-based covalent probe by appending a propargyl group to the C-terminus.[82] This novel technique built on previous research in his lab, and in other labs, that used wild-type Ub activity-based probes (Ub-ABPs) for proteomic and mechanistic profiling of novel DUBs in various disease relevant cells and tissues.[83–86] Ovaa's approach combined the selectivity of the UbV with the utility of the Ub-ABPs to further elucidate USP7 activity. This probe also contained a lysine-linked biotin, for neutravidin pull-down assays, and an N-terminal rhodamine for in-gel fluorescence to characterize the USP7 selectivity. USP7 selectivity was further validated using LCMS/MS on pull-down samples to characterize the modified residues on USP7 locations to define the UbV as an activity-based probe. This result paved the way for a portion of this thesis project, developing UbVs-ABPs selective for UCHL1 and UCHL3.

1.6 Project Summary

My thesis project focuses on development and characterization of the first UbVs and UbV activity-based probes (UbV-ABPs) selective for UCHL1 and UCHL3. Specifically, Chapter 2 will demonstrate the computational and rational design of UCHL1 specific mono-UbVs and the development of UCH sub-family specific UbV-ABPs. Chapter 3 will extend upon this approach and apply it to the production of a UCHL3 selective UbV-ABP and provide UbV-ABP cell permeable proof of concept studies. Chapter 4 will focus on the collaborative projects I have been a part of which include characterization of small molecule inhibitors for UCHL1 as well as

mechanistic studies of Ub-DUB binding. Future directions and conclusions will be presented in Chapter 5.

CHAPTER 2. DEVELOPMENT OF UBIQUITIN VARIANTS WITH SELECTIVITY FOR UBIQUITIN C-TERMINAL HYDRAOLSE DEUBIQUITINASES

The following chapter was adapted with permission from Hewitt, C. S., Krabill A. D., Das C., and Flaherty D. P., Biochemistry 2020, 59, 37, 3447-3462, © 2020 American Chemical Society. DOI:10.1021/acs.biochem.9b01076.

2.1 Introduction

Ubiquitin (Ub) is a highly conserved protein of 76 amino acids that is used for signaling within the eukaryotic cellular compartment.[87] Protein ubiquitination is an important post-translational modification that plays a role in many cellular processes including protein degradation, cell cycle regulation, and transcriptional regulation among others.[87] Protein ubiquitination events involve covalent linking of Lys residues side chains of target proteins to the terminal carboxylate group on Gly76 of Ub via an isopeptide bond. This attachment is catalyzed by three enzymes, an ATP-dependent Ub-activating E1 enzyme, a Ub-conjugating E2 enzyme, and a Ub E3 ligase. Ub can be appended to protein targets or attached to other Ubs to form poly-Ub chains, which function as biological signals that traffic substrate proteins toward various cellular pathways, with different lengths and linkages of poly-Ub chains regulating various phenotypic outcomes.[88] Ubiquitination events are regulated by deubiquitinating enzymes (DUBs) that hydrolyze the isopeptide bond linking Ub in a poly-Ub chain or to the protein target. A vast majority of the DUBs are cysteine-proteases, which through their roles in controlling ubiquitination events function as key players in disease-relevant pathways.[89] Indeed, over 90 DUBs have been identified that interact with Ub, either in mono- or poly-ubiquitinated states, with varying degrees of affinity and interaction topologies. Moreover, DUBs are emerging as promising drug targets for numerous disease states including auto-immune,[90] neurodegenerative disease,[91] and cancer.[92–94]

Seven subfamilies of DUBs have been identified and include ubiquitin specific proteases (USPs), ubiquitin C-terminal hydrolases (UCHs), Machado Josephin domain proteases (MJDs), ovarian tumor proteases (OTU), Jab1/MPN domain associated metalloisopeptide (JAMM) proteases, and more recently the ZUP1 and MINDY subfamilies.[22,23,95] Of these subfamilies, the USPs are the largest and most studied with > 50 members, while both the UCH and MJD subfamilies only contain four members.[93] A member of the UCH subfamily, ubiquitin C-terminal

hydrolase L1 (UCHL1), is primarily expressed in the central nervous system where it makes up anywhere from 1 – 5% of the total soluble protein content.[28,96] UCHL1 is genetically linked to Parkinson's disease (PD) as the single-point I93M mutation leads to early onset PD known as *PARK5*.[34] The DUB is also implicated in the progression of sporadic Parkinson's[97,98] and Alzheimer's disease.[99–101] Additionally, UCHL1 is considered an oncotarget for many forms of cancer as aberrant expression strongly correlates to increased metastatic behavior.[47,102] The small molecule pharmacological probe, LDN-57444,[56] has long been used to study UCHL1s role in these disease pathways; however, it suffers from significant shortcomings including chemical instability, low-solubility and lack of target engagement in cells.[60,103] Our group and others have recently reported on a cyanopyrrolidine scaffold that has promise to serve as a UCHL1 probe.[103,25] However, the majority of investigation into UCHL1s role in disease pathogenesis is carried out using time-consuming and laborious genetic methods to control UCHL1 protein levels in both cellular and animal models.

Small molecule inhibitor design targeting DUBs is still in its infancy compared to other enzyme families such as kinases. These enzymes were once considered difficult drug targets as the Ub-binding sites are conserved within subfamilies making development of selective small molecule inhibitors within a sub-family has been challenging.[76,104,105] However, recent progress has shown that small molecules are capable of providing the selectivity desired to probe DUB biology and covalent inhibitors are becoming more prevalent.[76] Alternatively, groups have leveraged Ub as a scaffold using phage display libraries[77,106,107] or computational[108] approaches to develop potent and selective Ub-variant (UbV) modulators of USP family DUBs. Ub covers a larger surface area at the Ub-binding domain of DUBs compared to small molecules and may provide more vectors for design of selective mutants to inhibit these protein-protein interactions (PPIs).

To address the lack of reliable UCHL1 pharmacological probes we set out to develop first-in-class UCHL1 selective UbVs that could ultimately lead to novel UCHL1 modulatory agents. A selective UbV could assist in the role of studying UCHL1's specific function in neurodegenerative disease and cancer. Our approach includes utilizing the Ub-bound crystal structures of UCHL1[109] and the closest structurally homologous protein UCHL3[110] (PDB ID: 3KW5 and 1XD3, respectively) to computationally predict Ub mutations that may impart selectivity, both binding and inhibition, for the UCHL1 PPI over the UCHL3 PPI. Predicted UCHL1 selective UbVs were

expressed recombinantly in *E. coli* and purified. *In vitro* binding was assessed toward UCHL1 and UCHL3 using both biolayer interferometry (BLI) and the UbVs ability to inhibit UCHL1 enzymatic activity was determined using the Ub-rhodamine110 (Ub-Rho) biochemical assay.[111] Finally, the prioritized UbVs were converted into activity-based probes (ABPs) and assessed for UCHL1 reaction selectivity in *in vitro* covalent binding assays and in cell lysates. The details presented herein provide evidence for utilizing a computational design approach to develop DUB selective UbVs.

2.2 Results

2.2.1 Computational Design of Ubiquitin Variants Selective for UCHL1

Rather than perform directed evolution or mutational scanning of residues on Ub to identify variants that would provide selectivity toward UCHL1, we sought to rapidly predict mutants using computational methods to narrow down the number that would be tested experimentally. For this, two computational approaches to predict mutations on Ub that would impart greater binding selectivity for UCHL1 over UCHL3, along with all other DUBs, were pursued. These methods approach the prediction of mutants in different ways. The first utilized the FoldX forcefield[112–114] to predict mutations beneficial for binding selectivity. This forcefield was developed to determine the mutational free energy changes of unfolding of a protein or protein complex rapidly and accurately. It simplifies the calculation of protein stability by following a linear combination of empirical terms that contribute to the energy of unfolding (energy of solvation, hydrogen bonds, electrostatic interactions, etc.) to calculate the change in free energy for mutations.[112] The second program utilized was RosettaDesign, specifically the affinity protocol algorithm, to predict affinity enhancing mutations.[37] This program performs energy calculations on the sequence using a fixed backbone followed by running Monte Carlo optimization and simulated annealing to predict mutations that are favorable to the overall free energy of the complex. Both programs have been applied successfully to predict mutations that improve the free energy of binding between two interacting protein partners[108,116–118].

Given that the Ub-UCHL1 PPI binding affinity is already intrinsically strong the goal for the design was not necessarily improvement of the binding affinity but improvement of binding selectivity since we intend to install a covalent electrophile to the C-terminus of any selective UbV.

Thus, even with reduced affinity toward UCHL1 the incorporation of an irreversible covalent bond forming electrophilic group would reduce the potential for off-competition in cellular environment by the endogenous Ub. UCHL1 and UCHL3 share over 50% sequence identity and a high degree of structural homology (Figure 2.1). To assess the influence of Ub residues on the binding to UCHL1, and to narrow down locations that would be subjected to position scanning, an alanine scan of Ub was performed *in silico*. The goal was to identify individual residues at the Ub-UCHL1 interface, that when mutated to alanine, did not significantly perturb the binding interaction.

A

```
# Length: 231
# Identity:     123/231 (53.2%)
# Similarity:   169/231 (73.2%)
# Gaps:           9/231 ( 3.9%)
# Score: 661.5
#
#
#=======================================

UCHL1_HUMAN        1 ---MQLKPMEINPEMLNKVLSRLGVAGQWRFVDVLGLEEESLGSVPAPAC     47
                        .:..|:|.|||:.|:.|.:||:...|:||||.|::.|.|..||.|.|
UCHL3_HUMAN        1 MEGQRWLPLEANPEVTNQFLKQLGLHPNWQFVDVYGMDPELLSMVPRPVC     50

UCHL1_HUMAN       48 ALLLLFPLTAQHENFRKKQIEELK--GQEVSPKVYFMKQTIGNSCGTIGL     95
                     |:|||||:|.::|.||.::.|::|  ||:|:..||||||||.|:||||||
UCHL3_HUMAN       51 AVLLLFPITEKYEVFRTEEEEKIKSQGQDVTSSVYFMKQTISNACGTIGL    100

UCHL1_HUMAN       96 IHAVANNQDKLGFEDGSVLKQFLSETEKMSPEDRAKCFEKNEAIQAAHDA    145
                     |||:|||:||:.||.||.||:||.|:..||||:||:..|..:||:..|:.
UCHL3_HUMAN      101 IHAIANNKDKMHFESGSTLKKFLEESVSMSPEERARYLENYDAIRVTHET    150

UCHL1_HUMAN      146 VAQEGQCR---VDDKVNFHFILFNNVDGHLYELDGRMPFPVNHGASSEDT    192
                     .|.|||..   :|:||:.|||...:||||||||||.|||:|||.:|::|
UCHL3_HUMAN      151 SAHEGQTEAPSIDEKVDLHFIALVHVDGHLYELDGRKPFPINHGETSDET    200

UCHL1_HUMAN      193 LLKDAAKVCREFTEREQGEVRFSAVALCKAA    223
                     ||:||.:||::|.||:..|:||:|:||..|
UCHL3_HUMAN      201 LLEDAIEVCKKFMERDPDELRFNAIALSAA-    230
```

B

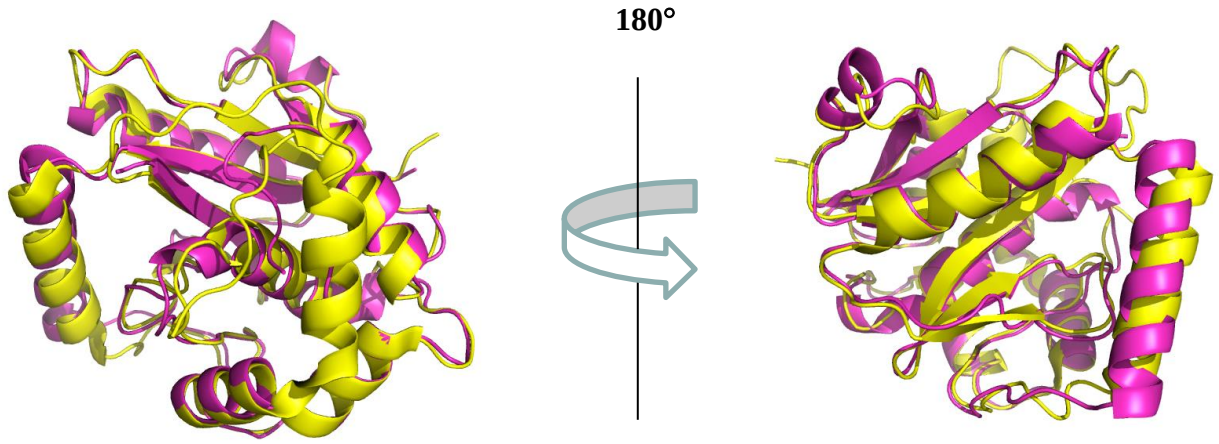

Figure 2.1 UCHL1 and UCHL3 Sequence and Structural Homology A) EMBOSS Needle Global Alignment of UCHL1 and UCHL3 protein sequences B) Structural homology of UCHL1 (yellow) and UCHL3 (magenta) crystal structures (PDB: 2ETL and 1UCH).

Previous literature demonstrates the standard deviation of a FoldX calculation is approximately 1.78 kcal/mol,[119] and suggests a cutoff of $\Delta\Delta G > +1$ kcal/mol to consider a mutation to be destabilizing and < -0.78 kcal/mol for it to be considered as stabilizing the complex.[112,120] Thus, we calculated predicted energy differences in binding to UCHL1 for each Ub-alanine mutant ($\Delta\Delta G_{Ub\text{-}UCHL1} = \Delta G_{WT\text{-}Ub} - \Delta G_{Ala\text{-}Ub}$) to narrow residues that were predicted to be amenable to mutation. We prioritized residues that were at the UCHL1-Ub interface and had a predicted $\Delta\Delta G_{Ub\text{-}UCHL1} < +1$ kcal/mol for position scanning. Tabular results for the predicted $\Delta\Delta G_{Ub\text{-}UCHL1}$ for each Ub-alanine mutant are reported in Table 2.1. Ub residues at the UCHL1-Ub PPI interface that had predicted $\Delta\Delta G_{Ub\text{-}UCHL1} > +1$ kcal/mol, and thus would destabilize the complex if mutated, were deprioritized from further analysis.

Next, these prioritized residues underwent *in silico* position scanning in FoldX, cycling through all 20 natural amino acid side chains while predicting the change in binding energy of the Ub-UCHL1 PPI. The predicted $\Delta\Delta G_{UCHL1} = \Delta G_{WT\text{-}Ub} - \Delta G_{X\text{-}Ub}$, where *X* corresponds to each respective amino acid side chain mutation at each particular residue, was calculated. The same calculation was performed using the Ub-UCHL3 crystal structure to provide $\Delta\Delta G_{UCHL3}$. To predict UbVs that would impart the largest degree of binding selectivity for UCHL1 over UCHL3 the difference in $\Delta\Delta G$'s was determined for each mutant ($\Delta\Delta\Delta G_{sel} = \Delta\Delta G_{UCHL1} - \Delta\Delta G_{UCHL3}$). Mutants that had the largest predicted $\Delta\Delta\Delta G_{sel}$ were prioritized for recombinant bacterial expression and data collection. Ub residues Thr9, Lys11, Asp39, and Gln40 provided the most mutants with predicted $\Delta\Delta\Delta G_{sel} < -1.0$ kcal/mol (Tables 2.2-2.5).

Table 2.1 Predicted Changes to Gibb's Free Energy of Binding for Ub-UCHL1 upon Alanine Mutation to Ub.The predicted differences in Gibb's free energy of binding between WT-Ub and each respective Ub alanine mutant with UCHL1 ($\Delta\Delta\Delta G = \Delta\Delta G_{WT\text{-}Ub} - \Delta\Delta G_{Ala\text{-}Ub}$) from FoldX alanine scan. Residues that have sidechain interactions at the Ub-UCHL1 PPI interface highlighted in yellow. Residues where alanine mutation is predicted to: 1) increase binding affinity or modestly reduce binding affinity up to 1 kcal/mol in green, or 2) reduce binding affinity by greater than 1 kcal/mol in red.

Ub-Residue/number	$\Delta\Delta G_{Ub\text{-}UCHL1}$ (kcal/mol)	Ub-Residue/number	$\Delta\Delta G_{Ub\text{-}UCHL1}$ (kcal/mol)
Met1	1.25	**Asp39**	-0.39
Gln2	0.14	**Gln40**	-1.77
Ile3	4.56	Gln41	0.47
Phe4	1.29	**Arg42**	-0.41
Val5	4.56	Leu43	4.68
Lys6	-0.16	**Ile44**	2.19
Thr7	1.57	Phe45	2.30
Leu8	2.11	Ala46	0
Thr9	0.32	Gly47	2.25
Gly10	3.25	Lys48	0.18
Lys11	0.07	Gln49	-0.46
Thr12	0.58	Leu50	4.26
Ile13	2.97	Glu51	-0.44
Thr14	-0.08	Asp52	-0.28
Leu15	3.89	Gly53	2.84
Glu16	-0.66	Arg54	-0.36
Val17	3.61	Thr55	-2.68
Glu18	-0.49	Leu56	3.47
Pro19	2.26	Ser57	-0.86
Ser20	-0.20	Asp58	-1.35
Asp21	-1.75	Tyr59	1.31
Thr22	-1.39	Asn60	0.12
Ile23	2.42	Ile61	3.55
Glu24	-0.33	Gln62	-0.46
Asn25	-2.11	Lys63	-1.08
Val26	2.95	Glu64	-0.22
Lys27	-0.30	Ser65	-0.85
Ala28	0	Thr66	0.38
Lys29	0.34	Leu67	4.30
Ile30	3.39	His68	-0.67
Gln31	-0.34	Leu69	4.63
Asp32	-1.67	**Val70**	1.62
Lys33	1.80	**Leu71**	3.58
Glu34	1.80	**Arg72**	-0.57
Gly35	3.22	**Leu73**	3.49
Ile36	3.10	**Arg74**	-1.37
Pro37	1.97	**Gly75**	3.10
Pro38	2.07		

Table 2.2 FoldX Position Scanning at Thr9.Predicted changes to Gibb's free energy of binding for Ub-UCHL1 ($\Delta\Delta G_{UCHL1}$) and Ub-UCHL3 ($\Delta\Delta G_{UCHL3}$) for each mutant at Thr9. The predicted selectivity ($\Delta\Delta\Delta G_{Sel}$) was calculated from the difference between $\Delta\Delta G_{UCHL1}$ and $\Delta\Delta G_{UCHL3}$. Residues prioritized for site-directed mutagenesis and recombinant purification highlighted in green.

Thr9(X); X =	**$\Delta\Delta G_{UCHL1}$ (kcal/mol)**	**$\Delta\Delta G_{UCHL3}$ (kcal/mol)**	**$\Delta\Delta\Delta G_{Sel}$ (kcal/mol)**
His	-22.4	-1.8	-20.6
Lys	-4.3	2.1	-6.4
Arg	-2.8	1.2	-4.0
Trp	-4.1	-1.2	-2.9
Tyr	-3.7	-0.9	-2.8
Phe	-3.2	-0.8	-2.4
Glu	-4.1	-1.8	-2.3
Leu	-1.1	0.8	-1.9
Gln	-2.6	-1.0	-1.6
Met	-0.6	0.9	-1.5
Asn	-1.8	-0.8	-1.0
Asp	-3.0	-2.2	-0.8
Ile	-0.3	0.5	-0.8
Ser	-1.6	-0.9	-0.7
Gly	-2.3	-1.7	-0.6
Cys	-0.8	-0.5	-0.3
Ala	-1.0	-0.7	-0.3
Pro	0.95	1.0	-0.05
Thr	-0.01	-0.01	0
Val	0.4	0.2	0.2

Table 2.3 FoldX Position Scanning at Lys11.Predicted changes to Gibb's free energy of binding for Ub-UCHL1 ($\Delta\Delta G_{UCHL1}$) and Ub-UCHL3 ($\Delta\Delta G_{UCHL3}$) for each mutant at Lys11. The predicted selectivity ($\Delta\Delta\Delta G_{Sel}$) was calculated from the difference between $\Delta\Delta G_{UCHL1}$ and $\Delta\Delta G_{UCHL3}$. Residues prioritized for site-directed mutagenesis and recombinant purification highlighted in green. Residues prioritized for mutations found through RosettaDesign are highlighted in yellow.

Lys11(X); X =	**$\Delta\Delta G_{UCHL1}$ (kcal/mol)**	**$\Delta\Delta G_{UCHL3}$ (kcal/mol)**	**$\Delta\Delta\Delta G_{Sel}$ (kcal/mol)**
Tyr	-0.5	0.9	-1.4
Arg	-0.4	0.5	-0.9
Met	0.1	0.9	-0.8
Glu	-1.2	-0.8	-0.4
Val	-0.8	-0.4	-0.4
Ala	-1.0	-0.6	-0.4
Ser	-1.5	-1.1	-0.4
His	-1.1	-0.7	-0.4
Thr	-1.3	-1.0	-0.3
Asp	-1.2	-1.1	-0.1
Pro	-3.2	-3.2	0
Asn	-1.0	-1.0	0
Leu	0.3	0.3	0
Gln	-0.7	-0.7	0
Gly	-1.7	-1.7	0
Lys	0	0	0
Cys	-0.8	-1.0	0.2
Phe	0.6	0.4	0.2
Trp	-0.5	-0.9	0.4
Ile	0.1	-0.4	0.5

Table 2.4 FoldX Position Scanning at Asp39.Predicted changes to Gibb's free energy of binding for Ub-UCHL1 ($\Delta\Delta G_{UCHL1}$) and Ub-UCHL3 ($\Delta\Delta G_{UCHL3}$) for each mutant at Asp39. The predicted selectivity ($\Delta\Delta\Delta G_{Sel}$) was calculated from the difference between $\Delta\Delta G_{UCHL1}$ and $\Delta\Delta G_{UCHL3}$. Residues prioritized and found in RosettaDesign for site-directed mutagenesis and recombinant purification highlighted in yellow.

Asp39(X); X =	**$\Delta\Delta G_{UCHL1}$ (kcal/mol)**	**$\Delta\Delta G_{UCHL3}$ (kcal/mol)**	**$\Delta\Delta\Delta G_{Sel}$ (kcal/mol)**
Ser	-0.76	0.48	-1.24
Asn	-0.50	0.68	-1.18
Thr	-0.27	0.88	-1.15
Pro	0.34	1.31	-0.98
Arg	0.76	1.59	-0.82
His	-0.36	0.42	-0.78
Leu	0.14	0.89	-0.76
Ala	-0.13	0.54	-0.67
Lys	0.88	1.42	-0.54
Tyr	0.19	0.56	-0.37
Phe	0.31	0.61	-0.30
Gln	0.91	1.20	-0.29
Gly	-0.59	-0.33	-0.26
Cys	0.09	0.30	-0.21
Val	0.46	0.66	-0.20
Trp	0.31	0.50	-0.18
Asp	-0.11	-0.01	-0.11
Met	1.47	1.58	-0.10
Glu	1.09	1.11	-0.02
Ile	1.62	1.05	0.56

Table 2.5 FoldX Position Scanning at Gln40.Predicted changes to Gibb's free energy of binding for Ub-UCHL1 ($\Delta\Delta G_{UCHL1}$) and Ub-UCHL3 ($\Delta\Delta G_{UCHL3}$) for each mutant at .Gln40. The predicted selectivity ($\Delta\Delta\Delta G_{Sel}$) was calculated from the difference between $\Delta\Delta G_{UCHL1}$ and $\Delta\Delta G_{UCHL3}$. Residues prioritized for site-directed mutagenesis and recombinant purification highlighted in green.

Gln40(X); X =	$\Delta\Delta G_{UCHL1}$ (kcal/mol)	$\Delta\Delta G_{UCHL3}$ (kcal/mol)	$\Delta\Delta\Delta G_{Sel}$ (kcal/mol)
Trp	-14.7	-1.0	-13.7
Tyr	-10.2	0.5	-9.7
Phe	-5.6	0.9	-6.5
His	-3.6	0.5	-4.1
Pro	-2.5	-0.02	-2.5
Leu	-0.7	0.9	-1.6
Lys	-1.2	0.2	-1.4
Arg	-0.9	0.5	-1.4
Glu	-2.3	-1.5	-0.8
Met	1.2	1.4	-0.2
Ile	-1.1	-0.9	-0.2
Gln	-0.1	-0.01	-0.09
Ser	-0.7	-0.7	0
Thr	-0.3	-0.4	0.1
Asn	0.1	-0.2	0.3
Asp	-2.4	-2.7	0.3
Val	-0.6	-0.9	0.3
Ala	-0.2	-0.8	0.6
Gly	-1.6	-2.4	0.8
Cys	0.2	-0.6	0.8

Alternatively, we employed the affinity protocol method using the RosettaDesign server. Both Ub-UCHL1 and Ub-UCHL3 crystal structure PDB files were uploaded into the server and the increase binding affinity protocol was selected. This method provided fewer potential mutations as the goal of the protocol is to simply improve the PPI binding affinity. The RosettaDesign affinity protocol method predicted K11I, K11W, and D39M as beneficial Ub mutations that would increase affinity toward UCHL1. Alternatively, only D39M was predicted to improve Ub binding affinity toward UCHL3. FoldX predicted T9E, T9F, T9H, T9K, T9R, T9W, T9Y, K11Y, Q40Y and Q40W as mutants that would improve binding toward UCHL1 while increasing binding selectivity over UCHL3. Both FoldX and RosettaDesign identified Lys11 and Asp39 as sites to improve Ub-UCHL1 binding affinity, however, there was some discrepancy. For example, RosettaDesign predicted D39M to improve Ub affinity to UCHL1 while FoldX predicted this mutation would reduce the stability of the Ub-UCHL1 complex (Table 2.4). In total 13 individual Ub mutants were selected for recombinant expression and experimental evaluation based on the combined computational methods. Those were: T9E, T9F, T9H, T9K, T9R, T9W,

T9Y, K11I, K11Y, K11W, D39M, Q40Y, and Q40W. Additionally, one mutant that was predicted to exhibit binding selectivity toward UCHL3, V70F was selected to further validate the design strategy.

2.2.2 Binding Analysis of Ubiquitin Variants to UCHL1 and UCHL3

Two orthogonal assays to assess binding of UbVs were performed against both UCHL1 and UCHL3. The first method utilized biolayer interferometry (BLI) to measure binding affinity for each UbV toward UCHL1 and UCHL3 and these data are presented in Table 2.6. Our BLI measurements of WT-Ub binding to UCHL1 ($K_d = 0.14 \pm 0.01$ μM) and UCHL3 ($K_d = 0.43 \pm 0.04$ μM) are comparable with previously reported K_d values[108] (Figure 2.2 and Table 2.6).

Mutations to Ub residue Thr9 displayed the greatest binding selectivity difference when mutated to an aromatic (Phe or Trp) or basic residue (Lys or Arg). Interestingly, when Thr9 was mutated to a Glu, a negatively charged amino acid residue under BLI assay conditions, the K_d to both UCHL1 and UCHL3 greatly increased (Table 2.6). The UbV^{D39M} predicted by RosettaDesign displayed ~2-fold stronger binding affinity when compared to WT-Ub. UbV^{K11I}, UbV^{K11W}, and UbV^{K11Y} were predicted to have increased binding affinity to UCHL1 but rather displayed comparable affinity to WT-Ub and slightly reduced affinity toward UCHL3. The UbV^{V70F} mutant predicted to impart binding selectivity for UCHL3 was equipotent against both UCHL1 and UCHL3 in the BLI assays. BLI association/dissociation curves and the steady-state plots for all UbVs tested presented in the appendix (Figure A.1 – Figure A.18)

An orthogonal UCH inhibitory assay was performed with each UbV to determine the IC_{50} of the UbVs when added to solutions with UCHL1 or UCHL3 and Ub-Rho. The IC_{50}s for the Thr9 UbVs remained largely consistent with the BLI data discussed previously (Table 2.7). UbV^{D39M} exhibited an IC_{50} that indicates increased inhibition for UCHL1 and UCHL3 when compared to WT-Ub, and is comparable to the K_d determined through BLI. Lys11 UbVs display reduced potency when compared to WT-Ub, consistent with the BLI K_d determination. UbV^{V70F} displayed significant inhibition selectivity for UCHL3 in the biochemical assay, a result that was expected from the *in silico* FoldX screening but not observed to the same degree in the binding affinity studies. UbV^{T9F} displayed the largest IC_{50} inhibition selectivity for UCHL1 of all the UbVs tested, with nearly 35-fold inhibition selectivity (Figure 2.3) over UCHL3. IC_{50} curves for all UbVs are included in the appendix (Figure A.19–A.20).

Table 2.6 Biolayer Interferometry K_d Values for UbVs Binding to His-UCHL1 and His-UCHL3

UbV	L1 K_d (μM)[a]	L3 K_d (μM)[a]	Binding Selectivity[c]	UbV	L1 K_d (μM)[a]	L3 K_d (μM)[a]	Binding Selectivity[c]
WT	0.14 ± 0.01 (0.1)[b]	0.43 ± 0.04 (0.42)[b]	3.1	**K11I**	0.33 ± 0.02	4.4 ± 0.3	13.3
T9E	110 ± 10	>200	< 1.8	**K11Y**	0.19 ± 0.004	0.50 ± 0.2	2.6
T9F	3.0 ± 0.9	18 ± 5	6.0	**K11W**	0.28 ± 0.05	1.1 ± 0.3	4.0
T9H	4.3 ± 0.3	24 ± 10	5.6	**D39M**	0.08 ± 0.01	0.14 ± 0.002	1.7
T9K	0.75 ± 0.02	8.0 ± 1	10.7	**Q40Y**	0.19 ± 0.03	0.77 ± 0.1	4.1
T9R	0.37 ± 0.04	2.5 ± 0.4	6.8	**Q40W**	0.15 ± 0.04	0.23 ± 0.06	1.5
T9W	2.1 ± 0.3	35 ± 10	16.7	**V70F**	8.3 ± 0.1	7.2 ± 0.5	0.87
T9Y	2.7 ± 0.003	19 ± 3	7.0				

[a]Experiments were performed in duplicate or triplicate and averages (and standard errors) are reported. L1 = His-UCHL1 and L3 = His-UCHL3. [b]Reported Kd values from Zhang et al.[41] [c]Binding selectivity = L3 Kd/L1 Kd.

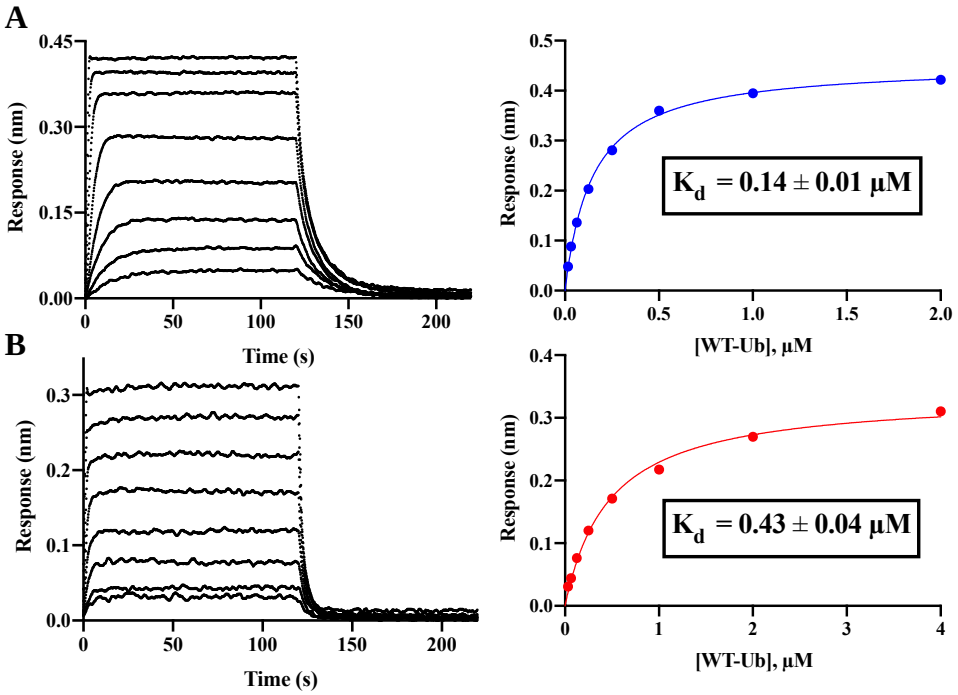

Figure 2.2 WT Ubiquitin K_d Determinations Utilizing Biolayer Interferometry.(A) Association/dissociation and steady-state binding data for His-UCHL1 and 1:1 serial dilutions of 2 μM WT-Ub in BLI assay buffer. (B) Association/dissociation and steady-state binding data for His-UCHL3 and 1:1 serial dilutions of 4 μM WT-Ub in BLI assay buffer.

Table 2.7 Ub-Rho Inhibitory Assay UbV IC_{50} Values for His-UCHL1 and His-UCHL3

UbV	L1 IC_{50} (μM)[a]	L3 IC_{50} (μM)[a]	Inhibition Selectivity[b]	UbV	L1 IC_{50} (μM)	L3 IC_{50} (μM)	Inhibition Selectivity[a]
WT	0.41 ± 0.03	0.82 ± 0.09	2.0	**K11I**	1.1 ± 0.2	3.0 ± 0.3	2.72
T9E	>100	>50	>2	**K11Y**	1.2 ± 0.1	4.9 ± 0.7	4.08
T9F	2.0 ± 0.3	70 ± 10	35.0	**K11W**	1.2 ± 0.1	7.2 ± 0.9	6.0
T9H	23 ± 4	>50	>2.2	**D39M**	0.18 ± 0.01	0.16 ± 0.01	0.89
T9K	0.90 ± 0.1	9.8 ± 2	10.9	**Q40Y**	1.0 ± 0.06	2.2 ± 0.3	2.2
T9R	1.1 ± 0.1	3.3 ± 0.9	3.0	**Q40W**	0.59 ± 0.04	0.35 ± 0.04	0.59
T9W	16 ± 3	>50	> 3.1	**V70F**	>100	0.54 ± 0.1	0.01
T9Y	13 ± 2	7.2 ± 2	0.55				

[a]Experiments were performed in duplicate or triplicate and averages (and standard errors) are reported. L1 = His-UCHL1 and L3 = His-UCHL3. [b]Inhibition selectivity = L3 IC_{50}/L1 IC_{50}.

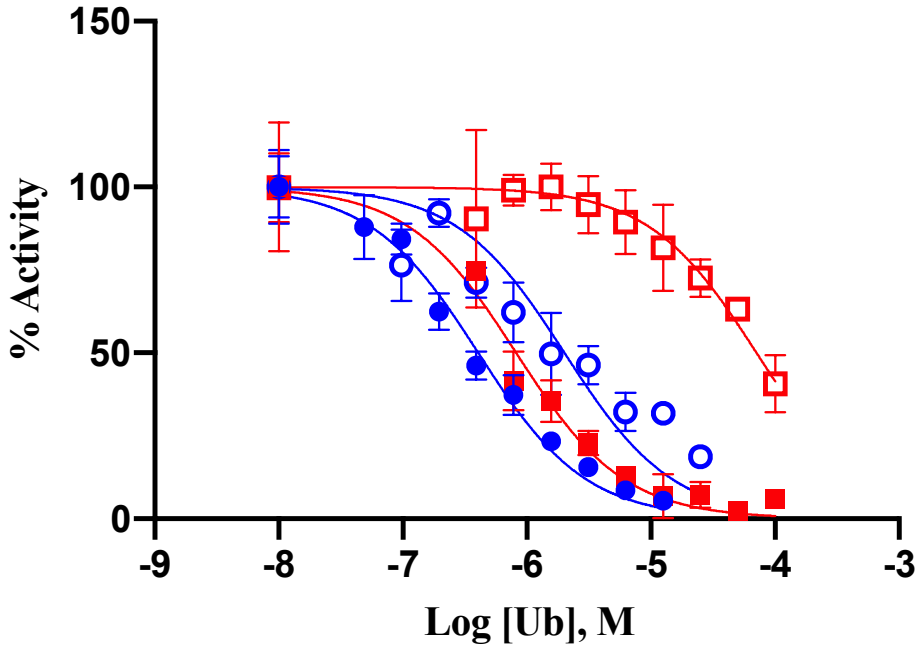

Figure 2.4 UbV^{T9F} Displays Increased Inhibition Selectivity for UCHL1 Compared to WT-Ub in Ub-Rho Inhibitory Assay. Inhibition curves for UCHL1 (blue circles) and UCHL3 (red squares) with WT-Ub (closed shapes) and UbV^{T9F} (open shapes).

2.2.3 Design of a Multi-Mutant Ubiquitin Variant

Determining the K_ds and IC_{50}s for UbVs with UCHL1 and UCHL3 provided a baseline for binding and inhibition selectivity for UCHL1. With over 90 DUBs expressed in human cells among seven known subfamilies we sought to add a second mutation onb to impart binding selectivity over non-UCH subfamily DUBs. The UbV^{T9F} was chosen as the representative UCHL1 selective mutant due to the binding selectivity it displayed in the Ub-Rho inhibitory assay (35-fold over UCHL3) as this was a readout of the UbVs ability to inhibit the enzyme catalytic turnover as opposed to strictly binding affinity. Literature search of other reported Ub mutant studies for DUB binding revealed that USP family DUBs are susceptible to Thr66 mutation.[79] A closer look at the Ub-bound structures for these DUBs indicated the Thr side chain forms a productive hydrogen bond with a conserved Lys, such as Lys391 in the case of USP7 (Figure 2.4A, PDB: 1NBF).[121] In fact, a basic amino acid is well conserved at this position as many USPs have either a lysine or arginine that form direct interactions with Thr66 (examples for USP2-Ub PDB: 2HD5[122]; USP14-Ub PDB: 2AYO[123]; USP21-Ub PDB: 3I3T[124]). Both the FoldX Ub alanine scan and previous literature suggest that mutation to Thr66 mutation would have no effect on UCHL1 binding as this residue has no surface interactions with the DUB (Table 2.1, Figure 2.4B). Thus, we hypothesized that substitution of a lysine at position 66 on Ub (T66K) would provide electrostatic repulsion when the positively charged side-chains come into proximity with the conserved lysine, in turn providing UbV binding selectivity over USP family DUBs. Based on these observations, the T9F/T66K double mutant UbV ($UbV^{T9F/T66K}$) was prioritized for recombinant expression.

Once $UbV^{T9F/T66K}$ was in hand it was tested in both BLI binding and Ub-Rho inhibition assays. The double mutant exhibited comparable binding affinities and IC_{50}s to both UCHL1 and UCHL3 as the UbV^{T9F} single mutant indicating the T66K mutation had little to no effect on UCH binding, as expected (Figure 2.5 and Table 2.8).

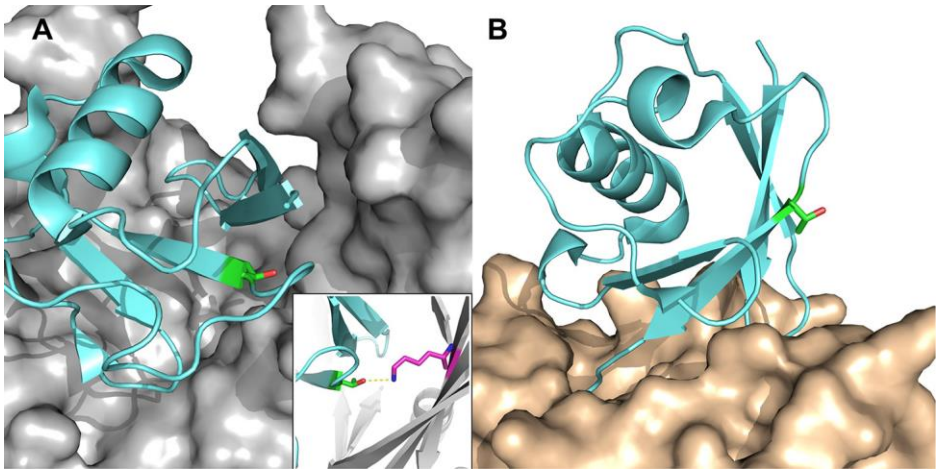

Figure 2.5 Ub-Binding Interface for USP vs UCH DUBs.(A) The Ub (cyan)-USP7 (gray surface) bound crystal structure (PDB entry 1NBF) shows Thr66 (green sticks) buried in a cleft between the fingers and palm domains. The inset depicts the hydrogen bond (yellow dashed line) formed between the Thr66 side chain of Ub (green sticks) and the Lys391 side chain of USP7 (magenta sticks). (B) The Ub (cyan)-UCHL1 (gold surface) bound crystal structure (PDB entry 3KW5) shows Thr66 (green sticks) solvent exposed and forming no interactions with UCHL1. Images were created using PyMol version 2.3.3. Figure created with BioRender.com.

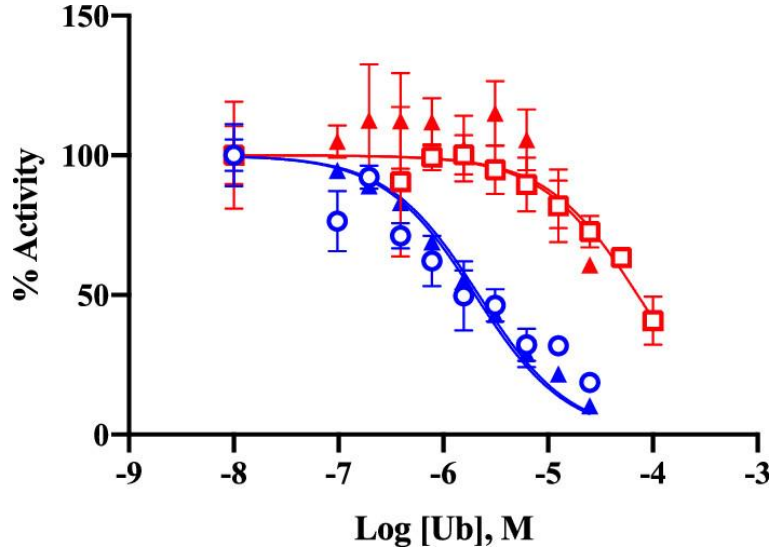

Figure 2.6 Inhibition Curves for UbV^{T9F} and $UbV^{T9F/T66K}$ vs UCHL1 and UCHL3

Table 2.8 BLI and Ub-Rho Inhibitory Assay Data with UbV^{T9F} and $UbV^{T9F/T66K}$

UbV	L1 K_d	L3 K_d	L1 IC_{50}	L3 IC_{50}
T9F	3.0 ± 0.9	18 ± 4	2.0 ± 0.3	70 ± 10
T9F/T66K	1.3 ± 0.1	43 ± 6	2.2 ± 0.1	>25[a]

All values in μM. K_ds are averages from duplicate experiments with standard errors reported. IC_{50}s were performed in technical triplicate with standard errors reported. K_ds and IC_{50}s are in μM. [a] Highest concentration tested was 25 μM. L1 = His-UCHL1 and L3 = His-UCHL3

2.2.4 Cell Lysate Western Blots with Ubiquitin Variant Activity Based Probes

An established method to assess broad DUB selectivity in cells is to convert UbVs to HA-tagged activity-based probes (ABPs) and treat lysates followed by blotting for HA.[125–127] To develop activity-based probes (ABPs) for UCHL1, HA-UbVs containing a C-terminal intein sequence were expressed to allow for attachment of vinyl methyl ester (VME) and propargylamine (PRG) groups to the C-terminus of the HA-UbVs. These groups form covalent adducts with the active site cysteine of DUBs, allowing for assessment of reactivity of our UbVs utilizing western blot molecular weight shift assays with cell lysates. Two different electrophiles were selected for these studies as it has been demonstrated previously that some electrophiles exhibit selectivity among DUBs. To this point VME has been shown to be more reactive and less selective while PRG has been shown to be less reactive and more selective.[86,127] Development of selective UbV-ABPs will likely require a balance of binding selectivity with electrophile reactivity. $UbV^{T9F/T66K}$ was assessed for broad DUB selectivity via time course western blots in small cell lung cancer (SW1271) cell lysates using HA-$UbV^{T9F/T66K}$-VME and HA-$UbV^{T9F/T66K}$-PRG. The time-dependent western blots for SW1271 cell lysates dosed with VME and PRG are presented in Figure 2.6 and Figure 2.7**,** respectively. UCHL1 is a low molecular weight DUB (25 kDa) while other DUBs, namely USPs have higher molecular weight. Thus, it is expected that the selective UbVs would display reduced HA signal in the higher molecular weight regions compared the WT-Ub control. The HA blots show that HA-$UbV^{T9F/T66K}$-VME and HA-$UbV^{T9F/T66K}$-PRG are highly selective for the UCH family (UCHL1, UCHL3, and UCHL5) over USPs (Figure 2.6A and Figure 2.7A). Blotting for each individual UCH in the different samples confirm the reactivity of the HA-$UbV^{T9F/T66K}$-VME and PRG with UCH family DUBs (Figure 2.6B and Figure 2.7B).

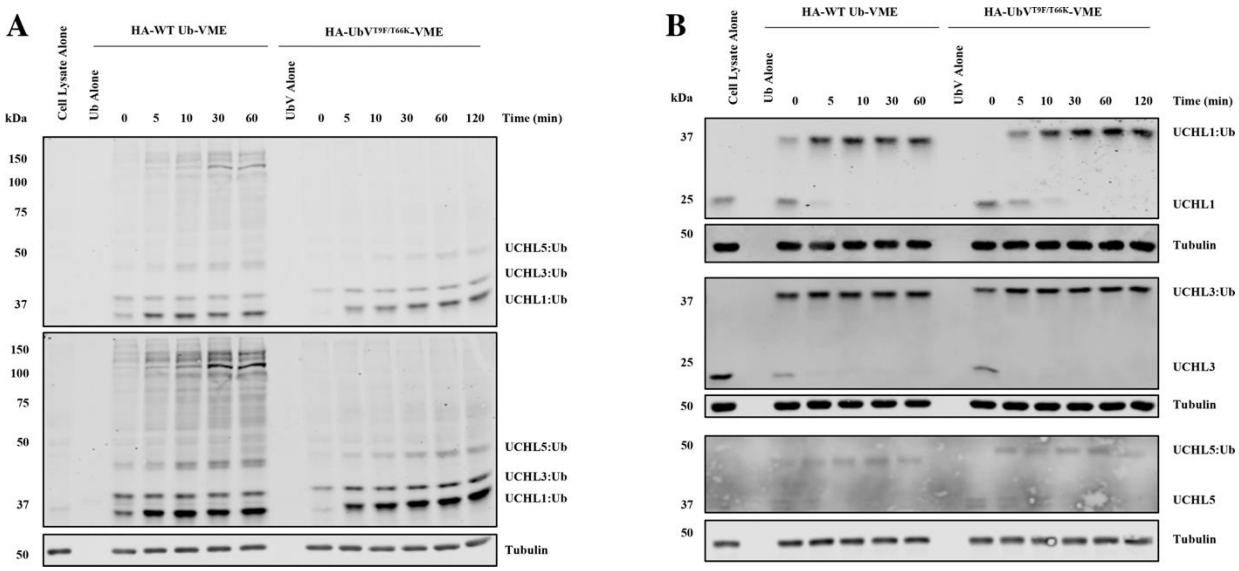

Figure 2.7 SW1271 Cell Lysate Time Course Western Blots Display UCH Selectivity of HA-UbV$^{T9F/T66K}$-VME.HA-WT-Ub-VME (0.5 μM) and HA-UbV$^{T9F/T66K}$-VME (0.5 μM) were incubated with 0.5 mg/mL SW1271 cell lysate for the times stated above the lanes at 37 °C. (A) HA immunoblots with low brightness (top) and high brightness (bottom). (B) UCHL1 (top), UCHL3 (middle), and UCHL5 (bottom) immunoblots.

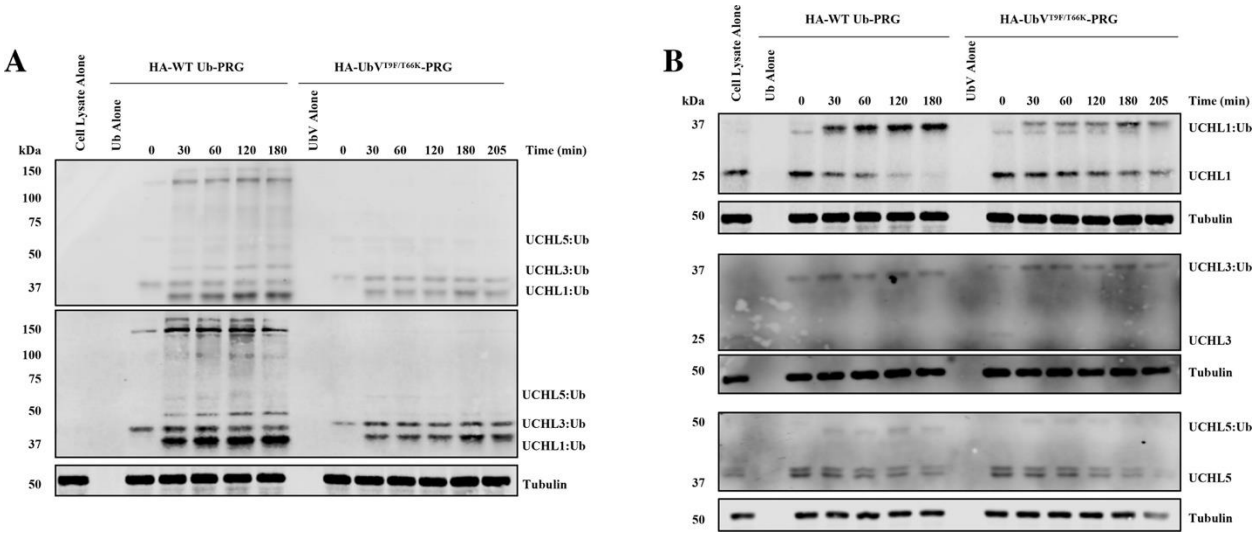

Figure 2.8 SW1271 Cell Lysate Time Course Western Blots Display UCH selectivity of HA-UbV$^{T9F/T66K}$-PRG.HA-WT-Ub-PRG (0.5 μM) and HA-UbV$^{T9F/T66K}$-PRG (0.5 μM) were incubated with 0.5 mg/mL SW1271 cell lysate for the times stated above the lanes at 37 °C. (A) HA immunoblots with low brightness (top) and high brightness (bottom). (B) UCHL1 (top), UCHL3 (middle), and UCHL5 (bottom) immunoblots.

Although our data would suggest that UbV$^{T9F/T66K}$ has UCHL1 binding selectivity over UCHL3 based on our *in vitro* binding assays this property did not translate to the lysate-based assay when tested at single UbV-ABP concentrations. The reactivity of the active site cysteine will also play a role in the overall reaction selectivity in lysates as the *in vitro* binding assays do not take into account the catalytic reactivity of the DUBs with the C-terminal electrophile on the ABPs. The previous time dependent western blots were all been performed at 0.5 μM Ub-ABP, however, we sought to determine if the reaction-selectivity was dose dependent. Thus, western blots were performed with increacting doses of either HA-WT-Ub-ABPs and HA-UbV$^{T9F/T66K}$-ABPs incubating with SW1271 cell lysates for 10 minutes in the case of VME and 30 minutes for PRG. The reactions were quenched at these time points and analyzed via western blot. HA-UbV$^{T9F/T66K}$-VME displayed dose-dependent reaction selectivity for UCHL1 over UCHL5 at the 10 minute time point as the HA-UbV$^{T9F/T66K}$ -UCHL1 adduct was fully formed at the 1 μM while UCHL5 required at least 5 μM of HA-UbV$^{T9F/T66K}$-VME for prominent adduct formation although it did not fully react as there are still trace amounts of unreacted UCHL5 present (Figure 2.8B). UCHL3 fully reacted with both HA-WT-Ub-VME and HA-UbV$^{T9F/T66K}$-VME at all concentrations at the 10 minute time point, indicating that even though the UbV may have a lower binding affinity for UCHL3 it still forms a covalent adduct with the VME at a greater rate than UCHL1 in cell lysates (Figure 2.8B). The reactive selectivity for UCHL3 is further supported in the dose dependent PRG blots (Figure 2.9) as UCHL3 reacted fully with HA-UbV$^{T9F/T66K}$-PRG at all concentrations tested. The PRG electrophile reduced the lysate-based activity versus UCHL1 as approximately ~ 50% of the UCHL1 formed adducts with the UbV-PRG at 5 μM concentration. There was negligible adduct formation with UCHL5 at 5 μM (Figure 2.9B). Interestingly, HA- UbV$^{T9F/T66K}$-PRG is highly selective for UCHL3 in SW1271 cell lysate at 0.1 μM concentration as no other DUBs appear to interact for 30 minutes (Figure 2.9A).

We hypothesized mutating Ub residue Thr66 to a lysine would mitigate interactions with many USPs, including USP7. Although the aforementioned time-dependent and dose-dependent western blots provide evidence that HA-UbV$^{T9F/T66K}$-VME and HA-UbV$^{T9F/T66K}$-PRG abrogate interactions with many DUBs outside the UCH subfamily relative to WT-Ub-ABPs, specific selectivity over USPs has not been provided. To investigate USP7 reaction selectivity, dose dependent USP7:HA co-localization western blots were completed (Figure 2.10). Both HA-WT-Ub-ABPs show interaction with USP7 at concentrations > 0.1 μM depicted by the band shift in

the USP7 blot and the yellow colocalization signals in the USP7:HA plots (Figure 2.10). As expected, the HA-UbV$^{T9F/T66K}$-ABPs displayed no interaction with USP7 at concentrations up to 5 µM HA-UbV$^{T9F/T66K}$-ABP treatments. Comparing these dose dependent western blots with the corresponding time-dependent western blots (Figure 2.8A and 2.9A) indicate no interaction with USP7 when treated with 0.5 µM HA-UbV$^{T9F/T66K}$-VME and HA-UbV$^{T9F/T66K}$-PRG. This selectivity is likely to be applicable to all USPs as the interaction of Ub Thr66 to the a conserved Lys or Arg is prevalent among all USPs. However, further analysis is necessary to confirm this hypothesis.

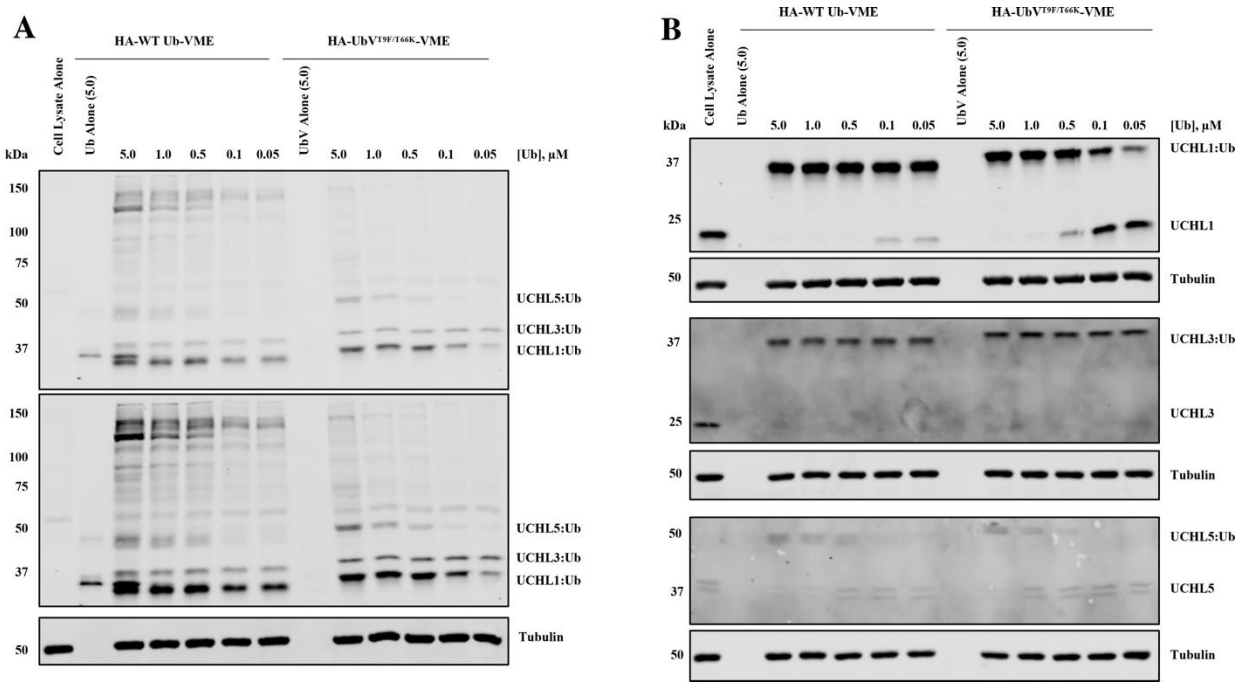

Figure 2.9 SW1271 Cell Lysate Dose-Dependent Western Blots Display UCH Selectivity of HA-UbV$^{T9F/T66K}$-VME.HA-WT-Ub-VME and HA-UbV$^{T9F/T66K}$-VME were incubated with 0.5 mg/mL SW1271 cell lysate at doses stated above the lanes at 37 °C for 10 min. (A) HA immunoblots with low brightness (top) and high brightness (bottom). (B) UCHL1 (top), UCHL3 (middle), and UCHL5 (bottom) immunoblots.

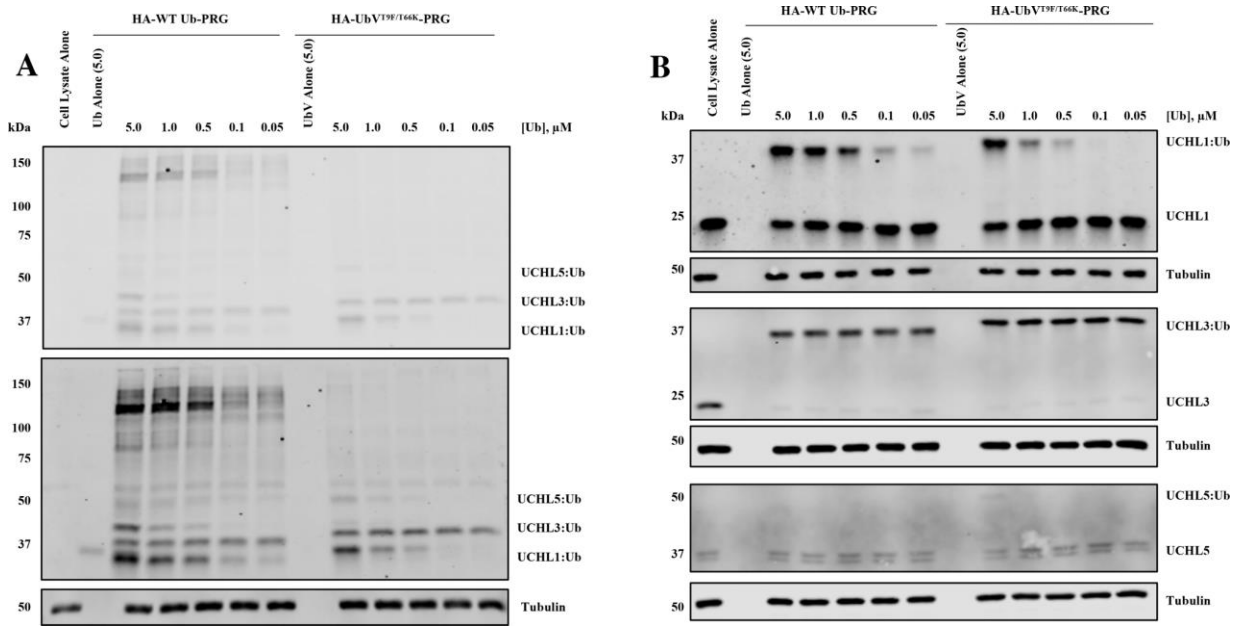

Figure 2.10 SW1271 Cell Lysate Dose-Dependent Western Blots Display UCH Selectivity of HA- UbV$^{T9F/T66K}$-PRG.HA-WT-Ub-PRG and HA-UbV$^{T9F/T66K}$-PRG were incubated with 0.5 mg/mL SW1271 cell lysate at doses stated above the lanes at 37 °C for 30 min. (A) HA immunoblots with low brightness (top) and high brightness (bottom). (B) UCHL1 (top), UCHL3 (middle), and UCHL5 (bottom) immunoblots.

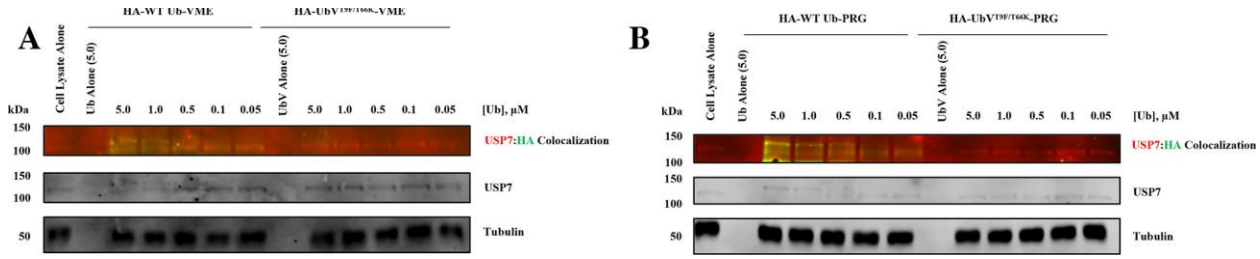

Figure 2.11 Dose Dependent USP7 Western Blot with HA-UbV$^{T9F/T66K}$-VME and -PRG.HA-UbV$^{T9F/T66K}$-VME and -PRG exhibit no interaction with USP7 in SW1271 cell lysates. (A) HA-WT-Ub-VME and HA-UbV$^{T9F/T66K}$-VME were incubated with SW1271 cell lysate at a protein concentration of 0.5 mg/mL at concentrations stated above the lanes at 37 °C for 10 min. (B) HA-WT-Ub-PRG and HA-UbV$^{T9F/T66K}$-PRG were incubated with SW1271 cell lysate at a protein concentration of 0.5 mg/mL at concentrations stated above the lanes at 37 °C for 30 min. Green for the HA tag, red for USP7.

2.2.5 Kinetics of Covalent Inhibition for UbV-ABPs versus UCHL1 and UCHL3

Together, the data above suggest that the reactivity of the active site cysteine with the electrophile of the Ub-ABP is a significant contributing factor in determining reaction selectivity of the UbV-ABPs. To confirm this k_{inact}/K_I studies were performed assessing the inactivation efficiencies of each Ub-ABP. As seen in Table 2.9, recombinant UCHL3 formed covalent adducts more efficiently with k_{inact}/K_I values 2-4 orders of magnitude greater than UCHL1 for all Ub-ABPs tested. These results corroborate previous literature showing UCHL3 is more catalytically active than UCHL1.[128] HA-UbV$^{T9F/T66K}$-VME and HA-UbV$^{T9F/T66K}$-PRG were approximately 5x slower at deactivating UCHL1 compared to WT-Ub counterparts. The kinetic data explain the reduced inactivation rates for UCHL1 and reaction selectivity for UCHL3 observed in the lysate-based experiments. Progress curve graphs from which the k_{inact}/K_I data was derived are included in the appendix (**Figure A.21-A.22**).

Table 2.9 kinact/KI values for ABPs versus UCHL1 and UCHL3
akinact/KI data was extracted from linear regression slopes of [Ub-ABP] vs kobs graphs. kobs values were extracted from a Michalis Menten-like fit of progress curve incubated with varying [Ub- ABPs]. All Ub-ABPs contain HA tag. Progress curves and linear fits can be found in appendix Figure A.21 – A.22.

Enzyme	Activity Based Probe	k_{inact}/K_I ($M^{-1}s^{-1}$)[a]
UCHL1	WT-Ub-VME	6.70×10^3
	UbV$^{T9F/T66K}$ -VME	1.38×10^3
	WT-Ub-PRG	1.28×10^2
	UbV$^{T9F/T66K}$-PRG	2.81×10^1
UCHL3	WT-Ub-VME	1.60×10^6
	UbV$^{T9F/T66K}$-VME	1.33×10^7
	WT-Ub-PRG	4.79×10^6
	UbV$^{T9F/T66K}$-PRG	6.44×10^3

2.2.6 Modeling of Ub^{T9F} Mutant Binding to UCHL1 and UCHL3

To investigate the role the T9F mutation may have on both binding to UCHL1 and UCHL3, as well as modulation of the inactivation rate that was observed, we performed molecular dynamics

(MD) simulations in Desmond (D.E. Shaw Research) and protein-protein interaction analysis in BioLuminate (Schrödinger, LLC). Several Ub and UCH complexes were analyzed including WT-Ub with apo-UCHL1 from the crystal structure PDB: 2ETL (Ub:UCHL1 (2ETL)), WT-Ub bound to UCHL1 from the Ub-bound crystal structure PDB: 3KW5 (Ub:UCHL1 (3KW5)), UbV^{T9F} with UCHL1 from the apo-crystal structure (UbV^{T9F}:UCHL1 (2ETL)), UbV^{T9F} with UCHL1 from the Ub-bound crystal structure (UbV^{T9F}:UCHL1 (3KW5)), and UbV^{T9F} with UCHL3 from the crystal structure PDB: 1XD3 (UbV^{T9F}:UCHL3). In the Ub crystal structure (PDB: 1UBQ) the β1-β2 loop is in a bent conformation resulting from side chain hydrogen bond interactions between Thr7 and Thr9.[10] This same loop configuration is maintained upon Ub binding to UCHL1[109] and UCHL3[110] as shown in the Ub-bound crystal structures (PDB: 3KW5 and 1XD3, respectively). The MD simulation of the Ub:UCHL1 (2ETL) complex recapitulates this same loop configuration observed in the experimental crystal structure (Figure 2.11A, cyan). In substituting Phe for Thr at this position the hydrogen bond interaction is no longer available. The MD simulation of the UbV^{T9F}:UCHL1 (2ETL) complex suggests in the absence of the Thr7-Thr9 side chain hydrogen bond interaction that this loop may, at least initially, adopt an extended configuration (Figure 2.11A, gray).

Frames were isolated at 5 and 9 nanoseconds (ns) into the UbV^{T9F}:UCHL1 (2ETL) simulation, both time points in which the β1-β2 loop was extended and were analyzed in BioLuminate with the protein-protein interaction analysis task. The extended configuration of that loop appears to provide access to additional productive contacts between the β1-β2 loop and UCHL1 in the UbV^{T9F}:UCHL1 complex that are not present in the same analysis of either the MD simulation of Ub:UCHL1 (2ETL) complex or the crystal structure of Ub-UCHL1 complex (PDB: 3KW5). In particular, the backbone carbonyl of Leu8 on UbV^{T9F} is within proximity to the backbone amide of Leu34 on UCHL1 and may form a new hydrogen-bond (Figure 2.11B). Additionally, the backbone amide of Gly10 on UbV^{T9F} is predicted to form a hydrogen bond with the side chain of Glu35, while the side chain of Lys6 is predicted to form hydrogen. bonds to the side chains of both Glu35 and Glu37 from UCHL1 (Figure 2.11B). As the simulation matures the Phe9 sidechain of UbV^{T9F} is predicted to rotate upward toward Thr7 where the aromatic side chain appears to rest near the alcohol of Thr7 for the remainder of the simulation (Figure 2.11C) perhaps stabilized by a lone-pair ••• p interaction.[129] Frames were taken at 25 and 35 ns into the UbV^{T9F}:UCHL1 (2ETL) complex simulation, in which the β1-β2 loop is now bent similar to apo-Ub, and submitted to

interaction analysis. These were no longer predicted to have the contacts describe above, but rather form no polar interactions between UbV^{T9F} and UCHL1 in this loop region consistent with the same analysis of the Ub:UCHL1 (3KW5). Thus, the reduced affinity for UbV^{T9F} compared to WT-Ub for UCHL1 may be attributed to the interplay of predicted productive contacts formed from the extended configuration balanced with a potential entropic penalty that may be incurred upon the β1-β2 loop re-configuring into the bent conformation to maintain binding to UCHL1.

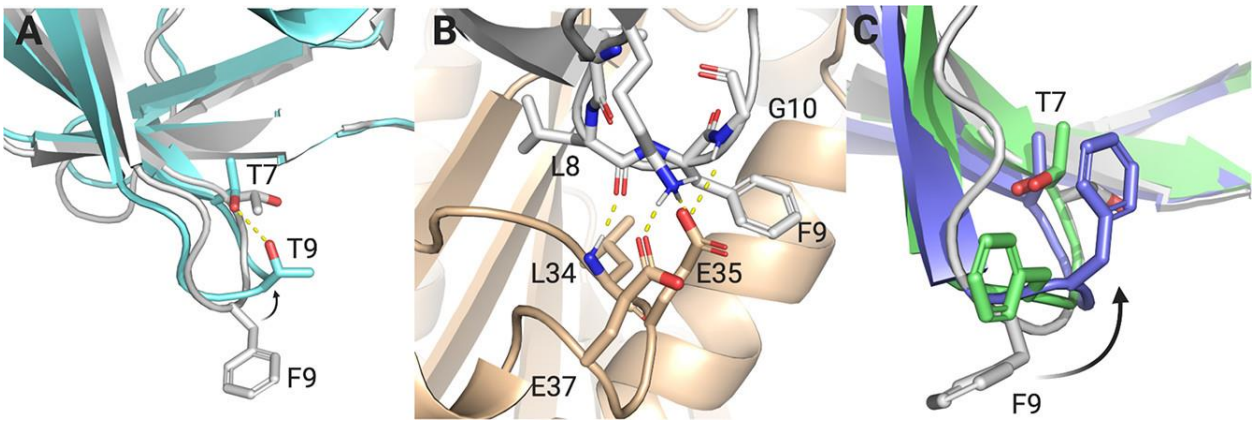

Figure 2.12 β1−β2 Loop Dynamics and Predicted Interactions with UCHL1.(A) Frames from MD simulations of Ub:UCHL1 (cyan) and UbV^{T9F}:UCHL1 (gray) complexes (PDB entry 2ETL was used; not shown in panel A for the sake of clarity). The black arrow depicts a change in the loop position. Interactions between side chains of Thr7 and Thr9 on Ub are shown with yellow dashed lines. (B) Predicted binding interactions of the UbV^{T9F}:UCHL1 complex (yellow dashed lines) with UbV^{T9F} (gray) and UCHL1 (gold) shown at the 9 ns time point of the MD simulation. (C) Predicted UbVT9F β1−β2 loop conformational change of the UbV^{T9F}:UCHL1 complex during binding at 9 ns (gray), 18 ns (green), and 25 ns (purple). UCHL1 not shown for the sake of clarity to provide focus on the loop. The black arrow depicts movement of the loop as time progressed to a final state that resembles the β1−β2 loop conformation in apo-Ub.

The same exercise was performed with UCHL3. The β1-β2 loop in the crystal structure of Ub-UCHL3 (PDB: 1XD3) has the same configuration as both unbound Ub and Ub bound to UCHL1. The MD simulation of UbV^{T9F}:UCHL3 (1XD3) complex predicts the β1-β2 loop of UbV^{T9F} may unravel during the binding event, opposite of the loop dynamics in UbV^{T9F}:UCHL1 complex (Figure 2.12). BioLuminate protein-protein interaction analysis of the UbV^{T9F}:UCHL3 complex suggests Lys6 of UbV^{T9F} forms a hydrogen bond with Asp38 of UCHL3, an interaction that is not present in the analysis of Ub-UCHL3 crystal structure (PDB: 1XD3). This residue corresponds to Glu37 of UCHL1 suggesting this interaction to the acidic side chain may be conserved between the two enzymes and UbV^{T9F}. However, UCHL1 contains a second acidic side chain in Glu35 that also is predicted to partake in a hydrogen bond with Lys6 of UbV^{T9F}, whereas the corresponding residue on UCHL3 is Gly36, which is incapable of forming the extra interaction with UbV^{T9F}. Moreover, protein-protein interaction analysis from time points throughout the duration of the MD simulation predict no additional contacts formed between UbV^{T9F} and UCHL3. These key differences in the proposed interaction framework on UbV^{T9F} binding to both UCHL1 and UCHL3 may provide the basis for the observed binding selectivity of the variant for UCHL1. Additional studies are necessary to fully elucidate the impact the T9F mutation has on Ub binding to UCHL1 and UCHL3, including structural and calorimetric analysis. Nonetheless, the MD simulations help to formulate a hypothesis for the role T9F plays in Ub binding to UCHL1 and may provide insight into the observed binding selectivity of UbV^{T9F} for UCHL1 or UCHL3.

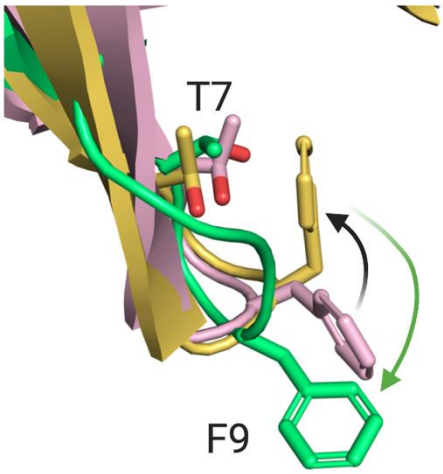

Figure 2.13 Molecular Dynamics Simulation of β1-β2 loop of UbV^{T9F} Upon Binding to UCHL3(PDB: 1XD3, not shown in figure). 19 ns (purple), 30 ns (yellow), and 92 ns (green) times point shown. Black arrow depicts movement of Phe9 from 19 – 30 ns during the binding event to UCHL3. Green arrow depicts movement of Phe9 from 30 – 92 ns during the binding event to UCHL3 as predicted by MD simulation.

As described above, the binding selectivity for the UbV^{T9F} mutant favors UCHL1 over UCHL3; however, the reaction selectivity favors UCHL3 over UCHL1. It has been previously reported that the catalytic triad (Asp176, His161 and Cys90) of apo-UCHL1 is misaligned in the active site and upon Ub binding the enzyme undergoes a conformational change shifting the triad

into alignment, in turn activating the catalytic Cys90.[109] Alternatively, the catalytic triad of UCHL3 is always aligned and the catalytic cysteine is activated for catalysis.[65,110] It is this variance between the two enzymes that accounts for the difference in catalytic rates. This can be seen when overlaying the apo-UCHL1 crystal structure with the Ub-bound UCHL1 structure (Figure 2.13A). When Ub binds to UCHL1 both Leu8-Thr9 on the β1-β2 loop of Ub displaces Phe214 of UCHL1. Phe214 flips and subsequently displaces Phe53, which in turn, shifts His161 into a position required for a properly aligned catalytic triad. Thus, only when Phe214 is displaced to set off this cross-talk event can Cys90 be activated for reaction. According to the kinetics of covalent inhibition data presented above the T9F mutation results in reduced overall activity-based probe reactivity of UCHL1 compared to WT-Ub (Table 2.9) suggesting the Phe9 of UbV^{T9F} does not activate UCHL1 as efficiently as Thr9 does for WT-Ub.

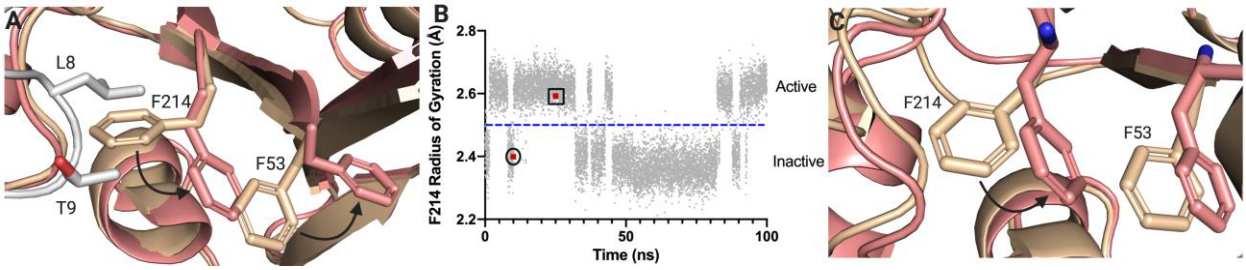

Figure 2.14 Dynamics of Phe214 upon Binding of UbV^{T9F}.(A) Overlaid crystal structures of UCHL1 (PDB entry 2ETL, gold) and Ub-bound UCHL1 (PDB entry 3KW5, salmon) zoomed in on the interaction of the Ub β1−β2 loop with F214 and F53. Black arrows depict the conformational change of F214 upon Ub binding from the inactive (gold) to the active (salmon) state and subsequent cross-talk that flips F53. (B) Plot of Rg values for F214 vs time of the MD simulation for the UbVT9F:UCHL1 complex (PDB entry 2ETL). The blue dashed line is inserted as a point of reference between Rg values for the inactive state and values for the active state. The Rg value at 10 ns is shown in a circle (inactive) and 25 ns in a box (active). (C) Overlay of MD simulation frames from 10 ns (gold) and 25 ns (salmon) that correspond to the values highlighted in the plot of Rg vs time. The position of F214 at 10 ns closely resembles that of the inactive conformation from apo-UCHL1, while the position of F214 at 25 ns resembles the active conformation. The black arrow depicts the change in position of F214. Residues 54–74 and 199–213 have been omitted for the sake of clarity. Images were created in PyMol version 2.3.3. Figure created with BioRender.com.

We again turned to the MD simulation to gain insight into the effect Phe in place of Thr at the 9 position of Ub may have on activation of UCHL1. To do this we tracked the radius of gyration (R_g), which is the root mean square distance of all atoms from the residue's center of mass, of the Phe214 from UCHL1 as a metric to differentiate between the Phe214 in the apo (inactive) conformation and the Ub-bound (active) conformation. We used the reported apo-UCHL1 crystal structure (PDB: 2ETL) and the Ub-UCHL1 crystal structure (PDB: 3KW5) to determine the benchmark R_g for Phe214 in both the inactive and active conformations (Figure 2.14 and 2.15). We then performed MD simulations using both UCHL1 (2ETL) alone and Ub:UCHL1 complex (3KW5) and plotted the R_g for Phe214 as a function of time. Phe214 of unbound UCHL1 was predicted to remain in an inactive conformation for the majority of the simulation, as expected, with the exception of a brief flip into the active configuration at around 62 ns (Figure 2.14). This suggests that even though the catalytic triad remains misaligned UCHL1 may be capable of becoming briefly activated. These results may explain why covalent inhibitors reported for UCHL1 are capable of forming adducts with the active site Cys90 in the absence of Ub.[59,60,103] The MD simulation for Ub:UCHL1 (3KW5) showed Phe214 remained in the active conformation for the entire simulation as expected **(**Figure 2.15). These results provided controls to define the R_g values for both the active and inactive conformations during the MD simulations.

Following the control simulations with UCHL (2ETL) and Ub:UCHL1 (3KW5) we performed a simulation with Ub binding to apo-UCHL1 (2ETL) to determine if the MD calculation would predict the transition of Phe214 from the inactive state to the active state as observed in the crystal structures. Gratifyingly, upon Ub:UCHL1 (2ETL) complex formation the sidechain of Phe214 on UCHL1 quickly rotated from the inactive to the active conformation and remained there for the duration of the simulation (Figure 2.16). These results essentially recapitulate the experimental data from apo- and Ub-bound UCHL1 and provide a benchmark to compare for UbV^{T9F}. Finally, we performed the MD simulation with UbV^{T9F} binding to apo-UCHL1. The results suggest the T9F mutant causes UCHL1 to oscillate between the inactive and active conformations (Figure 2.12), ultimately, spending more time in the inactive state when compare to WT-Ub. This suggests that while the T9F mutation to Ub is capable of activating UCHL1, it may be less efficient at keeping UCHL1 in the active conformation compared to Ub, thus reducing the catalytic reactivity of UCHL1.

Taken together, the MD simulation results provide insight into the effect the T9F mutation has on Ub binding to UCHL1. While the calculations are partly validated by previous experimental data, UCHL1 and Ub-UCHL1 structural data in particular, further investigation is necessary to confirm the new interactions proposed by the simulation. Nonetheless, the combination of both the reduced affinity observed by BLI and predicted effect on UCHL1 activation by UbV^{T9F} from the MD simulation may explain why the $UbV^{T9F/T66K}$-ABPs exhibit reduced efficacy in forming covalent adducts with UCHL1 compared to the WT-Ub-ABPs. Additionally, since the reactivity of Cys90 from UCHL1 is already at a significant disadvantage compared to the UCHL3 counterpart, reducing the reactivity even more with the T9F mutation appears to be too much to overcome to maintain the desired reaction selectivity over UCHL3.

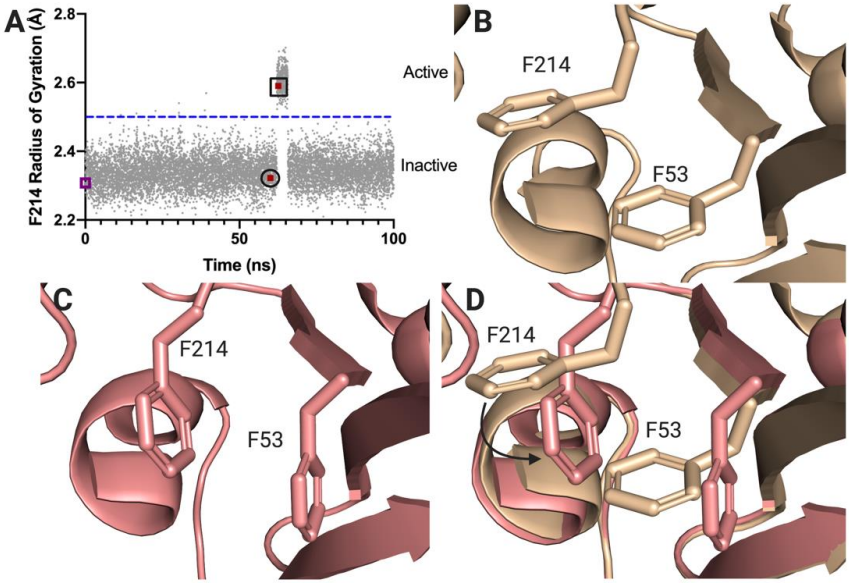

Figure 2.15 Molecular Dynamics of Phe214 of apo-UCHL1 Crystals Structure (PDB: 2ETL) with no Ub Present.(**A**) Plot of R_g values for F214 versus time of the MD simulation for apo-UCHL1 in absence of Ub. Blue dashed line inserted as reference point between R_g values for inactive state and values for active state. R_g value at 60 ns shown in circle (inactive) and 63 ns shown in box (active). Initial R_g value for F214 from apo-UCHL1 crystal structure shown by purple box on Y-axis. (**B**) Orientation of F214 of UCHL1 in the inactive conformation (gold) at 60 ns that corresponds to the R_g value at that time point. (**C**) Orientation of F214 of UCHL1 in the active conformation (salmon) at 63 ns that corresponds to the R_g value at that time point. (**D**) Overlay of MD simulation frames from 60 ns (gold) and 63 ns (salmon) that correspond to the values highlighted in the R_g versus time plot. The position of the F214 at 60 ns closely resembles that of the inactive conformation from apo-UCHL1 while the position of F214 at 63 ns resembles the active conformation. Black arrow depicts the change in position of F214. Residues 54 – 74 and 199 – 213 removed for clarity. Images were created in PyMol version 2.3.3.

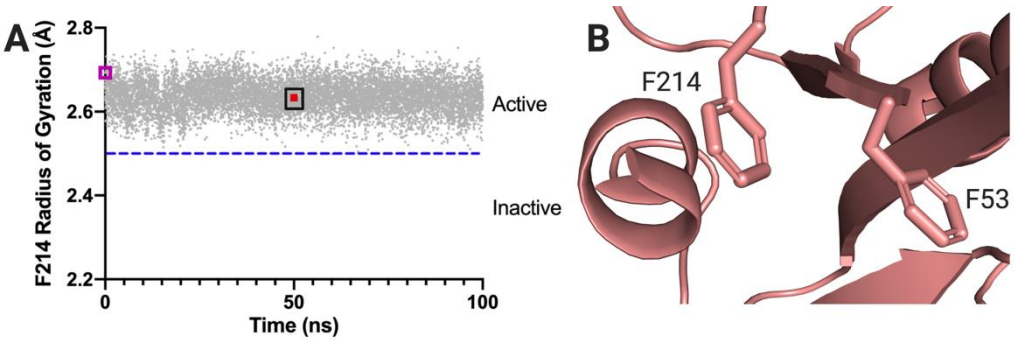

Figure 2.16 Molecular Dynamics of Phe214 from Ub-bound UCHL1 Crystal Structure(PDB: 3KW5). (**A**) Plot of *Rg* values for F214 versus time of the MD simulation for Ub-bound UCHL1. Blue dashed line inserted as reference point between *Rg* values for inactive state and values for active state. *Rg* value at 50 ns shown in circle (inactive). Initial *Rg* value for F214 from Ub-bound - UCHL1 crystal structure shown by purple box on Y-axis. (**B**) Orientation of F214 of UCHL1 in the active conformation (salmon) at 50 ns that corresponds to the *Rg* value at that time point. Residues 54 – 74 and 199 – 213 removed for clarity. Images were created in PyMol version 2.3.3.

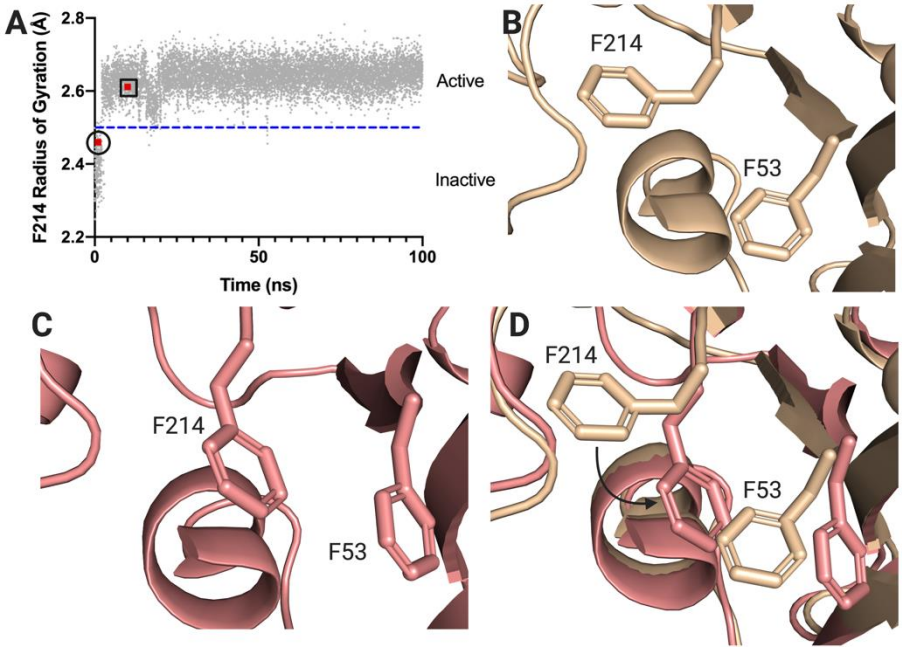

Figure 2.17 Molecular Dynamics of Phe214 of apo-UCHL1 Crystal Structure (PDB: 2ETL) with Ub Present.(**A**) Plot of R_g values for F214 versus time of the MD simulation for apo-UCHL1 in presence of Ub. Blue dashed line inserted as reference point between R_g values for inactive state and values for active state. R_g value at 1 ns shown in circle (inactive) and 10 ns shown in box (active). (**B**) Orientation of F214 of UCHL1 in the inactive conformation (gold sticks) at 1 ns that corresponds to the R_g value at that time point. (**C**) Orientation of F214 of UCHL1 in the active conformation (salmon sticks) at 10 ns that corresponds to the R_g value at that time point. (**D**) Overlay of MD simulation frames from 1 ns (gold sticks) and 10 ns (salmon sticks) that correspond to the values highlighted in the R_g versus time plot. The position of the F214 at 1 ns closely resembles that of the inactive conformation from apo-UCHL1 while the position of F214 at 10 ns resembles the active conformation. Black arrow depicts the change in position of F214. Residues 54 – 74 and 199 – 213 removed for clarity. Images were created in PyMol version 2.3.3.

2.3 Discussion

The predictive potential of FoldX and RosettaDesign along with the feasibility for computational design of UCHL1 selective UbVs was assessed. The $\Delta\Delta G_{Ub\text{-}UCHL1}$ values for mutants obtained from the *in silico* modeling were corroborated by previously reported experimental data from both Tencer et al.[79] and Luchansky et al.[130] Tencer et al. evaluated the effects of alanine mutations on the catalytic turnover of Ub-7-amino-4-methylcoumarin (Ub-AMC) biochemical substrates for a series of DUBs, including UCHL1. In particular, they showed individual alanine mutations at Leu8, Ile44, Val70, Leu71, Arg72, Leu73, and Arg74 significantly reduced the efficiency of UCHL1 catalytic turnover compared to WT-Ub-AMC.[79] The *in silico* predictions for $\Delta\Delta G_{Ub\text{-}UCHL1}$ are mostly in agreement with the experimental data as the alanine mutants at these residues are predicted to have significantly reduced binding to UCHL1, with the exceptions of Arg72 and Arg74 (Table 2.1). Luchansky et al. reported that Leu8 is essential for UCHL1-Ub recognition and the *in silico* alanine scan prediction in the present study also indicated L8A mutation would be detrimental to Ub-UCHL1 binding interaction.[130] With previous literature providing confidence in the *in silico* approach we moved to selecting mutants for improving binding selectivity to UCHL1 over UCHL3. In general, the computational predictions for selective mutants mostly translated to the *in vitro* assays for binding affinity and inhibitory activity. In fact, all but one mutant predicted by both programs displayed between 1.5-16.6-fold selectivity for UCHL1 over UCHL3 in the BLI assay with the lone exception being UbV^{T9E}, which displayed significantly reduced binding to both DUBs. UbV^{T9F} displayed the best combination of both binding and inhibition selectivity for UCHL1 over UCHL3. However, the gain in UCHL1 binding selectivity often came to the detriment of UCHL1 binding affinity. Interestingly, UCHL1 selectivity for the T9Y, D39M, and Q40W mutants did not carry over to the inhibitory assay, although in the case of D39M and Q40W, these mutants were the least selective toward UCHL1 in the binding assay to begin with. It is also interesting to note that even though UbV^{T9E} did not display any measurable binding to UCHL3 in the BLI assay it did in fact inhibit UCHL3 with an IC_{50} value of 6.6 μM. This disconnect between the binding and inhibitory data for UbV^{T9E} and UCHL3 will be part of future investigation. The predictions from RosettaDesign were less selective for UCHL1 in the binding affinity and inhibition assays, however, unlike FoldX where a user can rank order mutants and pick those that may provide selectivity, RosettaDesign only selects

mutants that are predicted to improve affinity toward either UCHL1 or UCHL3. Therefore, it is less likely that selective mutations would be predicted using this program.

MD simulations offered a possible explanation for why FoldX predicted mostly aromatic or basic residues at Thr9. The favor toward aromatic side chains may be attributed to potential for lone-pair ••• π interactions noted in the MD simulation for the UbV^{T9F}:UCHL1 (2ETL) complex. While an MD simulation was not performed for a UbV containing a basic amino acid at position 9, one could envision these side chains participating in hydrogen bond interactions with Thr7, as is observed with Thr9. Alternatively, these basic side chains may extend to form additional productive contacts with the UCHL1 surface. Further investigation is required to elucidate the role these amino acids may have on the selectivity.

Even though these mutations to Thr9 of Ub provided binding selectivity toward UCHL1 in binding and inhibitory assays they did not translate to reaction selectivity between UCHL1 and UCHL3 in lysates. We observed that although the $UbV^{T9F/T66K}$ was selective for UCHL1 over UCHL3 in the binding and inhibition assays, the $UbV^{T9F/T66K}$-VME and PRG reacted very fast with UCHL3 and much slower with UCHL1 in cell lysates, essentially flipping the reaction selectivity in favor of UCHL3. The lack of translation to lysate assays is likely due to the fact that the ABPs incorporate another important step in the inhibition process, which is the rate of covalent bond formation with the catalytic cysteine. This rate is dependent on the intrinsic reactivity of the catalytic cysteine. Therefore, while binding assays are a measure of reversible binding affinity, the greater intrinsic reactivity of UCHL3 over UCHL1 appears to compensate for the selectivity gained in consideration of binding affinity alone. This difference in covalent bond formation was quantified by performing progress curve analysis and deriving the k_{inact}/K_I shown in **Table 2.9**. Of note, all ABPs made were significantly slower at deactivating UCHL1 compared to UCHL3, and since both WT-Ub and $UbV^{T9F/T66K}$ were more selective for UCHL1 over UCHL3 in binding assays the only remaining explanation for the flip in reaction selectivity would be due to the decreased intrinsic reactivity of the UCHL1 catalytic cysteine compared to UCHL3 catalytic cysteine. These results are corroborated by previous reports that UCHL3 is significantly faster in catalytic turnover than UCHL1.

The HA-$UbV^{T9F/T66K}$-ABPs were approximately 5x slower than their WT-Ub counterparts in deactivating UCHL1. One factor that likely contributes to this reduced catalytic inactivation is the 3-fold reduction in binding affinity of UbV^{T9F} for UCHL1 compared to WT-Ub. A second factor

may be that the T9F mutation on the β1-β2 loop of Ub also reduced the efficiency of UCHL1 Cys90 activation. Evidence to support this hypothesis was provided by MD simulation in which the Ub-UCHL1 (2ETL) complex results were able to re-create the activation cross-talk event that has been previously reported for UCHL1 upon Ub binding and suggest this event happens rather quickly upon Ub binding. However, the UbV^{T9F} was less effective at flipping the Phe214 of UCHL1 from the inactive to active conformation and keeping it in the active conformation. The simulation suggests upon binding of UbV^{T9F}, UCHL1 is never fully activated but rather oscillates between the active and inactive conformations. This likely contributes to the overall reduced efficacy of $UbV^{T9F/T66K}$-ABPs to form covalent adducts with UCHL1 compared to WT-Ub-ABPs. This hypothesis will be further explored by structural and biophysical analysis of UbV^{T9F} binding to UCHL1. Nonetheless, it offers insight into future design of selective UCHL1 UbVs. For example, it would likely be beneficial to leave residues on the β1-β2 loop unaltered and focus elsewhere to incorporate selectivity driving mutations. Alternatively, mutations to the loop that may increase the rate of UCHL1 activation compared to WT-Ub may also be useful.

2.4 Conclusion

In conclusion, the computational design approach identified UbV mutations to impart binding and inhibition selectivity toward UCHL1 over UCHL3. The predictions were validated by *in vitro* binding assays with UCHL1 and UCHL3 with the most promising being the UbV^{T9F}. This UbV was selected to move to additional modification to provide broader DUB binding selectivity by incorporating a T66K mutation that was predicted to abrogate binding from other DUB families, including the largest USP family. However, the HA-$UbV^{T9F/T66K}$-ABPs exhibited increased reaction selectivity for UCHL3 over UCHL1, a result that was contrary to the observed binding selectivity. After further analysis it is hypothesized that the intrinsic reactivity of the catalytic cysteines from UCHL1 and UCHL3 play a large role in the reaction selectivity and the high reactivity of UCHL3 can overcome the UCHL1 binding selectivity. Indeed, k_{inact}/K_I studies with each Ub-ABP and enzyme indicate that UCHL3 forms covalent adducts with the ABPs approximately 100-10,000 fold faster than does UCHL1. Nonetheless, even though the $UbV^{T9F/T66K}$ lacked the desired reaction selectivity between UCHL1 and UCHL3 the T66K mutation did provide the desired selectivity over other DUB families in the lysate-based assays. To further investigate the contribution of the T9F mutation on both binding and reaction selectivity

for UCHL1 we turned to MD simulations. The results suggest the dynamics of the β1-β2 loop containing the T9F mutation may briefly provide access to new productive contacts between UCHL1 and also may not activate UCHL1 for covalent adduct formation as efficiently as WT-Ub. This hypothesis will be the basis of future study regarding mutations to this loop. Regardless, these results support the feasibility of computational design for UCHL1 selective UbVs and offer direction for development UbVs to gain reaction selectivity for UCHL1.

2.5 Experimental

2.5.1 Computational Prediction of UCHL1 Selective Ub Mutants

FoldX

The UCHL1 and UCHL3 ubiquitin bound crystal structures (PDB ID: 3KW5 and 1XD3) were loaded into YASARA[131] (version 17.8.15) containing the FoldX plugin[112–114] (http://foldxsuite.crg.eu) and energy minimized using the repair object function under the analyze tab to optimize amino acid side chains by improving torsion angles, removing van der Waal's clashes, and minimizing the energy of the structures as suggested by the FoldX protocol. Next an alanine scan was performed across Ub and the predicted change in binding affinity (ΔΔG) for the alanine mutants versus UCHL1 were calculated. Residue positions on Ub that tolerated mutation to Ala while binding to UCHL1, and were at or near the Ub-UCHL1 interface, were prioritized for subsequent position scanning. A position scan of natural amino acids was completed for each prioritized residue position and the predicted ΔΔG of binding for each UCHL1 and UCHL3 were tabulated ($\Delta\Delta G_{UCHL1}$ and $\Delta\Delta G_{UCHL3}$). The change in free energy for each mutant was subtracted to predict the mutations that would impart the largest degree of binding selectivity for UCHL1 over UCHL3 ($\Delta\Delta\Delta G_{selectivity} = \Delta\Delta G_{UCHL1} - \Delta\Delta G_{UCHL3}$). These ΔΔΔG values were utilized to prioritize recombinant ubiquitin mutants to express in *E. coli*.

Rosetta Design

The Ub-UCHL1 crystal structure PBD file was uploaded into the RosettaDesign[115] server (http://rosettadesign.med.unc.edu/). The "Increase Binding Affinity" protocol was selected on the

server interface then the job was submitted. The output file identified mutations to both UCHL1 and Ub that would provide a predicted improvement in binding affinity compared to WT-Ub. The same procedure was performed using the Ub-UCHL3 structure to ensure that selected Ub mutations predicted to improve affinity did not overlap. This protocol identified three single-point mutations to Ub that were predicted to improve Ub-UCHL1 binding affinity that did not overlap with Ub-UCHL3 predictions.

2.5.2 Generation of Recombinant Proteins

Plasmids, Mutagenesis, and Cloning

All plasmids were ordered from GenScript (Piscataway, NJ) unless otherwise noted. The site-directed mutagenesis and validation of the pRSET-A monoubiquitin plasmid was outsourced to GenScript. Plasmids were transformed into competent BL21(DE3) *Escherichia coli* cells (New England Biolabs, Cat# C2527I) and plated on ampicillin agar plates. Single colonies were picked from the agar plates and grown overnight at 37 °C with shaking at 250 RPM. Glycerol stocks were made from these cultures by mixing 20% glycerol and 80% bacterial culture and stored at -80 °C for future protein expressions.

Recombinant Expression of UCHL1 and UCHL3 Proteins

A pET-15b plasmid construct was used for the expression of both 6x-histidine (His)-tagged UCHL1 and His-UCHL3 in bacterial culture. These plasmids were transformed into competent BL21(DE3) E. coli cells using the procedure previously described. Starter cultures were grown at 37 °C with shaking at 250 RPM overnight. 10 mL of starter culture was inoculated into each liter of autoclaved LB media containing 100 µg/mL ampicillin and grown at 37 °C with shaking at 250 RPM to an OD of 0.4-0.8 before being induced with 300 µL of 1.0 M IPTG. These induced cultures were grown for 18 hours at 18 °C with shaking at 250 RPM. Bacterial cell pellets were spun down at 4000 x g for 20 minutes and resuspended in lysis buffer (1x PBS containing 400 mM KCl). These resuspended bacterial cells were stored in a -80 °C freezer for lysis on a later date or taken directly to lysis by sonication. Lysed bacterial cells were pelleted by centrifugation at 14,000 x g and the supernatant was loaded onto a Nickel-NTA column equilibrated with 1x PBS. After flow through was collected, the column was subject to a 0-500 mM imidazole step gradient and fractions

were collected. Both His-UCHL1 and His-UCHL3 eluted from the column at ~150 mM imidazole as evidenced by SDS-PAGE of fractions collected. Fractions that contained the desired protein were pooled together and dialyzed against 1x PBS containing 400 mM KCl with 1.0 mM DTT. This dialyzed protein sample was concentrated down using Amicon Ultra Centrifugal Filters and purified by size-exclusion chromatography (SEC) on an S200 column using running buffer (50mM Tris, 50 mM NaCl, 1mM DTT, pH 7.6). Fractions that contained the protein of interest were concentrated and placed in -80 °C for future experimental use.

Recombinant Expression of UbV Proteins

Monoubiquitin (herein referred to as ubiquitin or Ub) variants were purified from a pRSET-A vector. The untagged WT-Ub pRSET-A vector construct was obtained from Dr. Chittaranjan Das (Purdue University). This WT-Ub plasmid was sent to GenScript where site-directed mutagenesis was performed and validated. All UbVs were purified as described above with the following changes. The lysis buffer added to the bacterial cell pellets was 50 mM sodium acetate pH = 4.5. After lysis by sonication, the sample was boiled at 80 °C for 5 minutes to precipitate out the undesired proteins. After centrifugation at 14,000 x g, the pH of the supernatant was measured to be ~5 so it was adjusted to 4.5 with glacial acetic acid to further precipitate out undesired proteins. The precipitated proteins were centrifuged down at 4000 x g for 8 minutes. Supernatant was loaded onto a countertop SP SepharoseTM Fast Flow (Mono S) column (GE Healthcare, product number 17-0729-10), flow through was collected and the column was subject to a 0-1.0 M NaCl step gradient to elute out the UbVs. The fractions that contained UbVs (determined through SDS-PAGE analysis) were concentrated and further purified by SEC on an S200 column as described above.

Ubiquitin Intein Chitin Binding Domain Expressions

Variations of ubiquitin-intein-chitin binding domain (Ub-intein-CBD) proteins were expressed in a pTXB1 vector (containing an Mxe intein/chitin binding domain sequence). The process was performed for both WT-Ub and UbV. The WT-Ub-intein-CBD was provided by Dr. Chittaranjan Das (Purdue University, West Lafayette) and additions/mutations were made to this construct and validated by GenScript. Lysis buffer for these expressions was a 300 mM sodium

acetate buffer containing 50 mM mercaptoethanesulfonic acid (MES) at pH 6.0 (herein referred to as equilibration buffer). After lysis by sonication, cell debris was pelleted as described above and the supernatant was run in a column containing chitin resin (New England Biolabs, Catalog number: S6651S). Equilibration of the chitin column consisted of running 3 column volume (CV) of equilibration buffer through the column prior to column loading. Another 4 CV of equilibration buffer was washed through the column after which equilibration buffer containing 50 mM MES sodium salt (MESNa) was added. This was incubated in the column for 18 hours at 37 °C after which the desired protein was eluted out using the same buffer. The eluted Ub-MESNa sample was concentrated down to ~1.5 mL and stored at -80 °C until further use.

Ub activity-based probes (Ub-ABPs) were constructed by reacting excess glycine-vinylmethyester (VME) or propargylamine (PRG) with Ub-MESNa overnight in 1.0 M sodium bicarbonate containing 150 mg *N*-hydroxysuccinimide (NHS) in a total volume of 10 mL at pH 8.0 (to mitigate MESNa hydrolysis). This was dialyzed into 50 mM sodium acetate buffer pH 4.5 and run on a Mono S column to separate out the reacted species. The fractions that contained ubiquitin species of interest were determined by reaction with UCHL1 for 30 minutes at 37 °C and a subsequent SDS PAGE analysis.

2.5.3 Binding Characterization

Binding Affinity Measurements using Biolayer Interferometry

Ub and UbV binding affinity was measured according to a previously reported protocol[108] with minor changes, mainly our method utilized Ni-NTA coated biosensors (Molecular Devices, Part Number 18-5101) rather than streptavidin coated sensors. Initial concentrations of the UCH proteins were determined by A280 on NanoDrop™ (ThermoScientific) after which His-UCHL1 and His-UCHL3 were diluted into BLI buffer (1x PBS containing 0.05% v/v tween 20 and 0.1% w/v bovine serum albumin (BSA)) to concentrations of 25 µg/mL and 100 µg/mL, respectively, to achieve the similar loading in BLI assay. UbVs were buffer exchanged into 1x PBS using 0.5 mL Zeba™ spin desalting columns (ThermoScientific, catalog number 89882). The concentration of the UbVs was determined by BCA assay and diluted to top concentrations into BLI buffer and 1:1 serial dilutions were completed. Top concentrations differed in assay set-ups based on expected K_d from of UbV to UCH protein (for example WT-Ub top concentration was 2 µM for UCHL1

and 4 µM for UCHL3). 40 µL of each solution was added to a 384 tilted-bottom well plate (Molecular Devices, Part Number 18-5080). One Ni-NTA biosensor was used for each K_d measurement, dipping first into BLI buffer (initial baseline, 60 seconds), then the His-UCH protein wells (loading step, 300 seconds), then into BLI buffer alone (baseline step, 60 seconds) followed by dipping into lowest concentration of UbV (association step, 120 seconds) then into buffer alone (dissociation step, 100 seconds). A reference sensor of loaded with protein was dipped into buffer only containing wells to adjust for protein-buffer signals. The association-dissociation was repeated with increasing concentration of UbV. All measurements were taken at 30 °C.

Biacore Data Analysis Software (version 8.2) was used to collect and analyze the raw data for the association and dissociation curves. After subtraction of a reference sensor (loaded sensors dipped into buffer only containing wells), averages of the association responses (in nm response signal from 110 seconds – 115 seconds) was calculated and plotted as a function of UbV concentration in Prism 8. These data were fit to a non-linear regression one site – specific binding model to determine a K_d. Non-specific binding of the sensor to Ub (unloaded sensor tip dipped into Ub containing wells) was checked with WT-Ub. Negligible non-specific signal was observed at a concentration of 2 µM WT-Ub (not shown).

UCH Inhibition Assays

UbVs were buffer exchanged into 50 mM Tris-HCl containing 0.5 mM EDTA pH 7.6 using 0.5 mL Zeba spin desalting columns (ThermoScientific, catalog number 89882). The concentrations of each UbV were determined by BCA assay and were diluted to the 5x top assay concentrations in activity assay buffer (50 mM Tris, 0.5 mM EDTA, 0.1% bovine serum albumin, 5 mM DTT at pH 7.6). For UCHL1 5x top assay concentrations were; WT Ub = 62.5 µM, UbV^{T9E} = 500 µM, UbV^{T9F} = 125 µM, UbV^{T9K} = 500 µM, UbV^{T9R} = 250 µM UbV^{T9W} = 250 µM, UbV^{T9Y} = 250 µM, UbV^{K11I} = 250 µM, UbV^{K11Y} = 500 µM, UbV^{K11W} = 250 µM, UbV^{D39M} = 62.5 µM, UbV^{Q40Y} = 250 µM, UbV^{Q40W} = 500 µM, UbV^{V70F} = 500 µM, and $UbV^{T9F/T66K}$ = 125 µM. For UCHL3 5x top assay concentrations were; WT Ub = 500 µM, UbV^{T9E} = 250 µM, UbV^{T9F} = 500 µM, UbV^{T9K} = 500 µM, UbV^{T9R} = 250 µM, UbV^{T9W} = 250 µM, UbV^{T9Y} = 250 µM, UbV^{K11I} = 250 µM, UbV^{K11Y} = 500 µM, UbV^{K11W} = 250 µM, UbV^{D39M} = 62.5 µM, UbV^{Q40Y} = 250 µM, UbV^{Q40W} = 500 µM, UbV^{V70F} = 62.5 µM, and $UbV^{T9F/T66K}$ = 125 µM. 5x top assay concentrations differed for each UbV based on expected IC50. 1:1 serial dilutions of 5x top assay concentrations

for each UbVs were completed in activity assay buffer. His-UCHL1 and His-UCHL3 proteins were diluted into activity assay buffer and 20 µL of 2.5 nM His-UCHL1 and 0.25 nM His-UCHL3 were added to wells of a black 384-well plate (Fisher Scientific, product number 12566624) and incubated with 10 µL of a 5x concentrations of UbV for 30 minutes. The difference in enzyme concentration was due to activity differences in the enzymes and necessary to obtain a readout in the linear range for analysis. 450 nM stock of ubiquitin rhodamine110 (Ub-Rho) was made and 20 µL of this stock was added to the assay wells directly before fluorescent measurements were recorded using a Synergy Neo2 Multi-Mode Reader (Biotek) at excitation and emission wavelengths = 485 nm and 535 nm, respectively. Initial slopes were identified and plotted using Prism 8. The control (wells containing only activity assay buffer/no ubiquitin inhibitor) was normalized to 100% enzyme activity and the sample wells were calculated at percent activity compared to the control.

2.5.4 DUB Cell Engagement Assays

DUB engagement assays were performed according to previously published protocols with minor changes.[125] Cell pellets were lysed in 50 mM Tris-HCl buffer (pH 7.4) containing 150 mM NaCl, 5 mM $MgCl_2$, 5 mM DTT, 2 mM ATP, 0.5% NP-40, and 10% glycerol (herein referred to as cell lysis buffer) for 30 minutes on ice. Every 10 minutes the incubating cells were vortexed for 10 seconds to ensure homogeneous lysis. Cell lysates were clarified by centrifugation at 13,000 x g for 10 minutes and the supernatant was collected. Protein concentrations of clarified cell lysates were determined using Bradford assay and each sample was brought to a concentration of 0.5 mg/mL in cell lysis buffer. Initial hemagglutinin (HA) tagged Ub-Activity-Based Probe (ABP = vinyl methylester or propargylamine) concentrations were determined by A280 on a NanoDrop™ (ThermoScientific) system and diluted to 10 µM in cell lysis buffer. Concentration determinations by A280 measurements were performed with all HA containing Ub and UbVs because of the higher extinction coefficient provided by the HA sequence (leading to more accurate protein concentrations), relative to the mono-ubiquitins. 1 part of 10 µM HA-Ub-ABP was added to 19 parts of 0.5 mg/mL cell lysate and incubated in a heat block at 37 ºC for the times stated. 4x Laemmli buffer was added to the samples to terminate the reaction at each timepoint. For the dose dependency blots, 1 part of 20x concentration of HA-Ub-ABP was added to 19 parts of 0.5 mg/mL cell lysate and incubated in a heat block at 37 ºC for the times stated. 10 µL of each sample was

loaded onto a 12% SDS-PAGE gel and run at constant 190V for ~ 75 minutes. For the USP7 western blots, SDS-PAGE gels were run at a constant 190V for 130 minutes to achieve band separation of the USP7 and USP7:Ub-ABP. Gels were transferred to a nitrocellulose membrane and subjected to western blot procedures. Primary antibodies used were HA-Tag - 6e2 (Cell Signaling Technologies), C29F4 (Cell Signaling Technologies), Ab18181 (Abcam); UCHL1 - 15C7 mouse hybridoma (University of Iowa Developmental Studies Hybridoma Bank); UCHL3 – D25E6 (Cell Signaling Technologies), Ab126621 (Abcam); UCHL5 – Ab133508 (Abcam); Alpha Tubulin – Ab7291 (Abcam) or Ab176560 (Abcam); USP7 – Ab4080 (Abcam). Fluorescent secondary antibodies (Licor IRDye 680RD Goat anti-Rabbit and Licor IRDye 800CW Goat anti-Mouse) were used. Images were collected on a Licor Odyssey system.

2.5.5 Ubiquitin Activity Based Probe k_{inact}/K_I Assays

The k_{inact}/K_I is a metric that is relevant for irreversible inhibitors as the efficacy of the covalent bond formation is dependent on the rate of the bond forming reaction as well as the ligand binding to the target. The k_{inact}/K_I describes the potency of the first reversible binding event in the inhibition constant (K_I) and the maximum rate of inactivation (k_{inact}). To obtain this data His-UCHL1 and His-UCHL3 enzymes were diluted to 2.5 nM and 0.25 nM stock solutions, respectively, in 50 mM Tris-HCl (pH = 7.6) buffer containing 0.5 mM EDTA, 5 mM DTT, and 0.1% w/v BSA. HA-WT-Ub-ABPs and HA-UbV-ABPs underwent 1:1 serial dilutions from a top concentration in the same buffer. The UCH enzyme concentrations were optimized to obtain a dynamic range for progress curves for k_{obs} determinations. Ub-Rho (Boston Biochem, catalog number U-555) was diluted to 450 nM in the same buffer to make the Ub-Rho stock. 20 µL of Ub-Rho stock solution was first added to each well in a 384-well plate followed by 10 µL of HA-WT Ub ABP or HA-UbV ABP. To initiate the reaction, 20 µL of each respective enzyme stock solution was added and fluorescence measurements were immediately recorded on a Synergy Neo 2 Multi-Mode Reader (BioTek) at excitation and emission wavelengths of 485 nm and 535 nm, respectively. Progress curve raw data was input into Prism 8 and a baseline correction analysis was completed to obtain all the time = 0 points at the origin for fitting purposes. Each progress curve underwent fitting to $Y = V_0*(1-e^{(-kobs*t)})/k_{obs}$.[132] The k_{obs} values for each progress curve was graphed against the concentration of HA-WT Ub-ABP or HA-UbV-ABP. The slope of the linear fit was determined to be the k_{inact}/K_I (the rate constant describing the UbVs inactivation efficiency (covalent bond

formation on the catalytic cysteine) on the UCH enzymes resulting from the potency (K_I) of binding and the maximum potential rate of inactivation (k_{inact}).

2.5.6 Mutational Modeling and Molecular Dynamic Simulations

An initial structural alignment was performed to align the apo-UCHL1 X-ray crystal structure (PDB: 2ETL) to the Ub-bound UCHL1 X-ray crystal structure (PDB: 3KW5) in maestro using protein prep wizard (Schrödinger, LLC). The thioester bond between UCHL1 and Ub was broken, and UCHL1 from the 3KW5 structure was removed, being replaced by UCHL1 from 2ETL and the glycine vinylmethyl ester moiety was built back in to Ub. Preprocessing was completed by generating heteroatom states using Epik[133] (Schrödinger, LLC) for the pH range of 7.4 ± 0.2. Hydrogen bond assignments were optimized using PROPKA (Schrödinger, LLC) at a pH of 7.4. Removal of waters at 3.0 Å beyond heteroatoms and with fewer than 3 H-bonds to non-waters was completed. Initial energy minimization was completed using OPLS3e force field to yield the minimized Ub:UCHL1(2ETL) structure. The T9F mutation was generated by selecting Thr9 and mutating it to a Phe and repeating the protein preparation process as described above yielding a minimized UbV^{T9F}:UCHL1(2ETL) structure. Four more structures were generated in a similar manner, excluding the first alignment step. For these structures, the 3KW5 crystal structure was used to generate the Ub:UCHL1(3KW5) and UbV^{T9F}:UCHL1(3KW5) minimized structures. In an identical manner, the 1XD3 crystal structure was used to generate the Ub:UCHL1 (1XD3) and UbV^{T9F}:UCHL3 (1XD3) minimized structures. Finally, an apo UCHL1 structure was prepared from 2ETL following the process described above, excluding the alignment step.

Each minimized structure was further prepared for molecular dynamics simulation using Desmond (D.E. Shaw Research, release 2020-1) in System Builder (Schrödinger, LLC). The solvent model was set to TIP3P, and orthorhombic was set as the box shape. The box size calculation used was according to buffer, and the volume was minimized. The system was neutralized by adding sodium ions (number of ions was automatically calculated by the System Builder), and salt ions (Na^+ and Cl^-) was added at a concentration of 0.15 M. The system was then minimized using the OPLS3e force field.

The molecular dynamics simulation was performed using the Molecular Dynamics application (D. E. Shaw Research) within Maestro (Schrödinger, LLC). The simulation time was set to 100 ns with 10 ps recording intervals. All other settings were left as default. Phe214 was

selected and the radius of gyration (R_g) was calculated at each recording interval. The R_g was plotted versus time in GraphPad Prism Version 8.3.1.

2.5.7 Interaction Analysis in BioLuminate

Molecular dynamic files were used to extract modified .pdb files (waters and ions deleted) at representative time points for UCHL1 and UCHL3 Ub interactions. Preprocessing was completed by generating heteroatom states using Epik[133] (Schrödinger, LLC) for the pH range of 7.4 ± 2.0. Hydrogen bond assignments were optimized using PROPKA (Schrödinger, LLC) at a pH of 7.4. Removal of waters at 3.0 Å beyond heteroatoms and with fewer than 3 H-bonds to non-waters was completed. Energy minimization was completed using OPLS3e force field to yield the minimized structures for interaction analysis using BioLuminate[134,135] (Schrödinger, LLC).

CHAPTER 3. DEVELOPMENT OF SELECTIVE UBIQUITIN VARIANTS FOR UBIQUITIN C-TERMINAL HYDROLASE L3

3.1 Introduction

Deubiquitinating enzymes (DUBs) are regulatory enzymes for the ubiquitination pathway. These proteins exist in seven distinct sub-families which include the ubiquitin specific proteases (USPs), ubiquitin C-terminal hydrolases (UCHs), Machado Josephin domain proteases (MJDs), ovarian tumor proteases (OTU), Jab1/MPN domain associated metalloisopeptide (JAMM) proteases, and more recently the ZUP1 and MINDY subfamilies.[22,23,95]

UCHL3, a member of the UCH subfamily of DUBs has recently gained traction as a potential cancer target through its effects on DNA repair pathways and upregulated expression in many cancers. Specifically, UCHL3 has been identified as a deubiquitinase that controls the proteostasis of tyrosyl DNA phosphodiesterase 1 (TDP1), the enzyme responsible for hydrolyzing the covalent bond between type 1 topoisomerases (TOP1) and the 3-prime phosphate of DNA.[66] Depletion of UCHL3 in rhabdomyosarcoma cells markedly reduced the levels of TDP1 and increased sensitization of cells to TOP1 poisons. UCHL3 has additionally been implicated in DNA double stranded break repair pathway by deubiquitinating Ku proteins, which sense broken DNA by binding to chromatin and helping to initiate non-homologous end joining (NHEJ).[67] Ubiquitination of Ku proteins is important for Ku protein removal from chromatin after NHEJ has completed.[136,137] Other examples include findings from a recent paper that UCHL3 is responsible for deubiquitinating lymphoid-specific helicase (LSH), a chromatin modifier, linked to migration, invasion, and tumor formation in non-small cell lung cancer (NSCLC).[68] Furthermore, overexpression of UCHL3 has also been seen in breast cancer and is well correlated with poor survival rates.[69] Additionally, UCHL3 deubiquitinates and, therefore, stabilizes forkhead box M1 (FOXM1), a key transcription factor and regulator of cell cycle progression in pancreatic cancer leading to cancer progression.[70] Finally, UCHL3 overexpression has been shown to promote ovarian cancer by stabilizing TRAF2 to activate the NF- κB inflammation signaling pathway, leading to poor prognosis for patients.[71,72]

While UCHL3 is growing in potential importance relating to its identification as a cancer target, there have been only two small molecule inhibitors reported in the literature. The first reported UCHL3 inhibitor 4,5,6,7-Tetrachloro-1*H*-Indene-1,3(2*H*)-dione, or TCID, was identified

serendipitously in a high throughput screen has been reported to inhibit UCHL3.[56] However, this was only demonstrated *in vitro* and the molecule has not been fully validated to inhibit UCHL3 in cells. More recently, perifosine has been suggested to inhibit UCHL3 in breast cancer cell lines.[72] However, this inhibitory effect was demonstrated by deubiquitination of the protein RAD51 in cells by Ub-immunoblot and did not show on-target engagement of perifosine with UCHL3.[72,73] Furthermore, the molecule does not inhibit UCHL3 *in vitro* in the standard Ub-AMC enzymatic assays. Based on the lack of UCHL3 chemical probes with validated on-target activity in cells there is a clear need for an alternative strategy to elucidate UCHL3 activity in cancer.

While the previous chapter focused on deriving selective ubiquitin variants (UbVs) for UCHL1, this chapter will utilize data from the previous chapter along with other computational methods to derive and characterize UCHL3 selective UbVs and UbV-activity based probes (ABPs). Our group utilized biolayer interferometry and Ub-Rho inhibition assays to characterize the UCHL3 binding selectivity of our mono-UbV. In addition, characterization of the UCHL3 reaction selectivity of several UbV-ABPs were experimentally determined using k_{inact}/K_I assays and cell lysate western blot molecular weight gel shift assays. This chapter characterizes the first highly selective UCHL3 selective mono-UbVs and UbV-ABPs that can be utilized for in-cell determination of UCHL3 activity in cancer and other disease states.

3.2 Results

3.2.1 FoldX Computational Design of UbV^{V70F}

The previous chapter discusses the development of a mono-UbV that is selective for UCHL1. To accomplish this goal, our group utilized the Ub-bound crystal structures of UCHL1 to perform a rational structure-based approach for designing our UCHL1 selective UbVs[31]. UCHL3 shares a high degree of structural homology with UCHL1, thus we used the Ub-bound UCHL3 crystal structure to impart selectivity against the closest structural homolog. An alanine scan was initially completed (Table 2.1) to deduce which residues were amenable to mutation. After, several Ub residues underwent a position scan on the computational program FoldX to calculate the ΔΔG stability of the Ub:UCHL1 or Ub:UCHL3 interaction. Ub mutations were prioritized if they exhibited a high degree of UCHL1 binding stability while destabilizing the UCHL3 complex. To provide an additional level of validation for our FoldX methodology for

developing UCHL1 selective mono-UbVs, a mono-UbV that was predicted to be selective for UCHL3 over UCHL1 was prioritized. Based on the FoldX position scan, UbV^{V70F} was chosen as it displayed one of the most stable complex formations based on a $\Delta\Delta G_{UCHL3}$ of -5.4 while providing a large $\Delta\Delta\Delta G_{Sel}$ value providing computational evidence of UCHL3 selectivity against UCHL1 (Table 3.1).

Table 3.1 FoldX Position Scanning at Val70.Predicted changes to Gibb's free energy of binding for Ub-UCHL1 ($\Delta\Delta G_{UCHL1}$) and Ub-UCHL3 ($\Delta\Delta G_{UCHL3}$) for each mutant at Val70. The predicted selectivity ($\Delta\Delta\Delta G_{Sel}$) was calculated from the difference between $\Delta\Delta G_{UCHL1}$ and $\Delta\Delta G_{UCHL3}$. Residues prioritized for site-directed mutagenesis and recombinant purification highlighted in green.

Val70(X); X =	**$\Delta\Delta G_{UCHL1}$ (kcal/mol)**	**$\Delta\Delta G_{UCHL3}$ (kcal/mol)**	**$\Delta\Delta\Delta G_{Sel}$ (kcal/mol)**
Ser	-2.8	-2.3	-0.4
Met	0.1	0.3	-0.1
Leu	0.6	0.7	-0.1
Lys	0.6	0.7	-0.1
Pro	-3.3	-3.2	0.0
Cys	-1.8	-1.9	0.0
Val	0.0	-0.1	0.1
Gly	-3.1	-3.2	0.1
Asn	-1.7	-2.0	0.3
Ala	-1.8	-2.1	0.3
Thr	-1.8	-2.1	0.3
Gln	-0.6	-1.1	0.4
Ile	0.7	0.2	0.5
Asp	-3.4	-3.9	0.5
His	-4.0	-5.0	1.0
Glu	-3.0	-4.2	1.3
Phe	-2.1	-5.4	3.3
Arg	0.8	-2.6	3.4
Tyr	-4.3	-9.1	4.8
Trp	-2.6	-14.8	12.2

3.2.2 UCHL3 Binding Selectivity of UbV^{V70F}

Once UbV^{V70F} was recombinantly expressed, the binding selectivity was tested utilizing biolayer interferometry (BLI) and a Ub-Rho DUB activity assay was performed to determine the K_d and IC_{50}, respectively, against both recombinantly expressed UCHL1 and UCHL3. A similar degree of selectivity was observed upon K_d determinations based on steady state BLI data (Figure 3.1) with UCHL3 K_d = 7.1 ± 0.6 µM and UCHL1 K_d =8.2 ± 1.4 µM. The association and dissociation curves as well as individual BLI measurements are provided in the appendix (Figure A.17). On the other hand, in the Ub-Rho DUB activity assay format, UbV^{V70F} displayed > 180-fold UCHL3 selectivity (UCHL3 IC_{50} = 0.54 µM, UCHL1 IC_{50} = >100 µM, Figure 3.2). This selectivity was greater than the reported small molecule inhibitors, perifosine and TCID (>125 selective). In fact, in our hands neither the perifosine nor TCID molecules inhibit UCHL3 to any degree (up to concentrations of 50 µM and 10 µM, respectively) when using the Ub-Rho assay format (Figure 3.3).

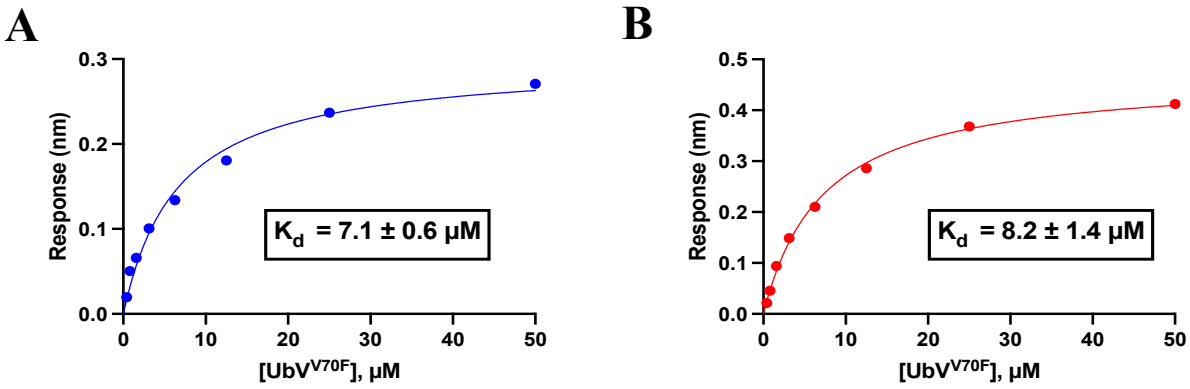

Figure 3.1 Steady State Binding Curves for UbV^{V70F} against UCHL3 and UCHL1. UbV^{V70F} Displays Similar Binding Selectivity to UCHL3 over UCHL1. A) UCHL3 steady state, B) UCHL1. Errors are standard errors over duplicate measurements.

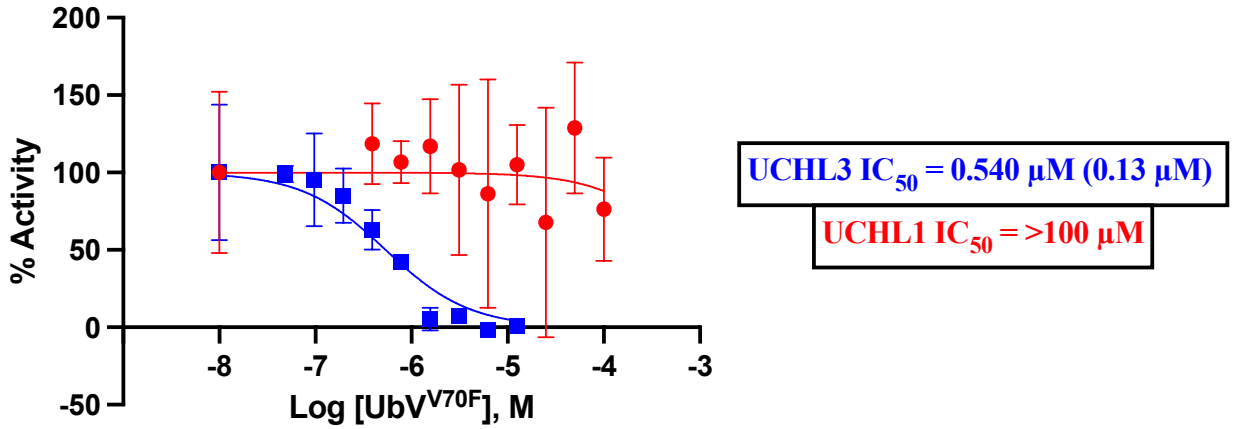

Figure 3.2 UbV^{V70F} Inhibition vs UCHL3 and UCHL1.

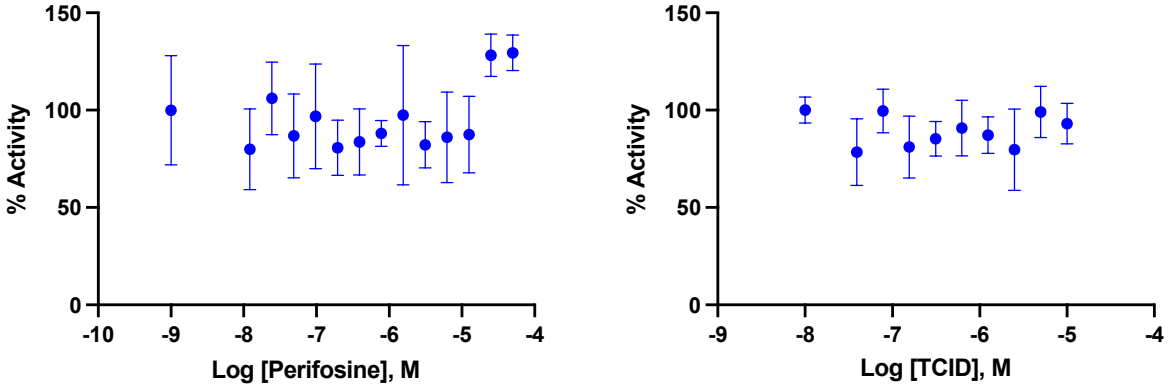

Figure 3.3 Perifosine and TCID Display no Inhibition of UCHL3 in Ub-Rho Assay

3.2.3 Development and UCHL3 Selectivity Characterization of $UbV^{T66K/V70F}$-Activity-Based Probes

In the previous chapter, we utilized ubiquitin specific protease 7 (USP7)-Ub bound crystal structure (PDB:1NBF) to deduce that a Thr66Lys mutation on Ub may provide an electrostatic repulsion against a conserved lysine residue in USPs.[31] Thus, to increase the selectivity of our UbV^{V70F} against USPs, we introduced the Thr66Lys mutation into a plasmid encoding for a C-terminal intein of our Ub to allow expression of $UbV^{T66K/V70F}$-Intein. This intein construct permits the addition of cysteine reactive electrophilic warheads to our $UbV^{T66K/V70F}$ allowing for covalent addition and inactivation of DUBs. Vinyl methylester (VME) and propargylamine (PRG) electrophiles were used to append onto the C-terminus of our UbVs for use as activity-based probes (ABPs). The reaction selectivity against UCHL3 and UCHL1 was characterized using k_{inact}/K_I and is shown below in Table 3.2 with the WT-Ub-ABP k_{inact}/K_I values reported in Hewitt et. al for comparison.[31] Individual progress curves and k_{obs} graphs can be seen in the appendix (Figure A.23). Comparing selectivity for UCHL3 over UCHL1 it was observed that both ABPs were more selective for UCHL3 by orders of magnitude. For example, $UbV^{T66K/V70F}$-VME displayed a k_{inact}/K_I of 1.7 x 10^6 M^{-1} s^{-1} for UCHL3 and 1.38 x 10^2 M^{-1} s^{-1} for UCHL1, a difference of over 12,000-fold in favor of UCHL3. Similarly, the $UbV^{T66K/V70F}$-PRG displayed a k_{inact}/K_I of 4.06 x 10^4 M^{-1} s^{-1} against UCHL3 while it was essentially inactive against UCHL1 (3.78 $M^{-1}s^{-1}$) amounting for >10,000-fold selectivity for UCHL3. Therefore, even though $UbV^{T66K/V70F}$-PRG was less efficient at inactivation of UCHL3 compared to the -VME counterpart, it was prioritized for further characterization studies in HEK-293 cell lysates because of the extremely low inactivation efficiency toward UCHL1.

Table 3.2 k_{inact}/K_I Data for HA-UbV$^{T66K/V70F}$-ABPs against UCHL3 and UCHL1.

Enzyme	Electrophilic Warhead	Ubiquitin	k_{inact}/K_I ($M^{-1}s^{-1}$)
UCHL3	VME	WT-Ub	[a]1.6×10^6
		UbV$^{T66K/V70F}$	1.72×10^6
	PRG	WT-Ub	[a]4.79×10^6
		UbV$^{T66K/V70F}$	4.06×10^4
UCHL1	VME	WT-Ub	[a]6.70×10^3
		UbV$^{T66K/V70F}$	1.38×10^2
	PRG	WT-Ub	[a]1.28×10^2
		UbV$^{T66K/V70F}$	3.78×10^0

[a] Values reported in Hewitt et. al.[31]

3.2.4 Characterizing the UCHL3 Selectivity of UbV$^{T66K/V70F}$-PRG in Cell Lysates

Time-dependent western blot assays were used to assess if ABP-selectivity for UbV$^{T66K/V70F}$-PRG translated from the biochemical assay and if broader DUB selectivity was achieved in a cellular context. To do this, both HA-WT-Ub-PRG and HA-UbV$^{T66K/V70F}$-PRG were dosed into HEK-293 cell lysate. As expected, we observed that the HA-WT-Ub-PRG non-selectively labeled multiple DUBs in HEK-293 cells at 30, 60, and 120-minute timepoints as evidenced by the green signal equating the HA-immunoblot (Figure 3.4, left). In contrast, there was very little observed off target labeling for HA-UbV$^{T66K/V70F}$-PRG at the same timepoints, with perhaps a slight band at approximately 50 kDa. Co-staining for UCHL3 in the same blot confirmed the DUB labeled by the UbV was UCHL3 (Figure 3.4, right).

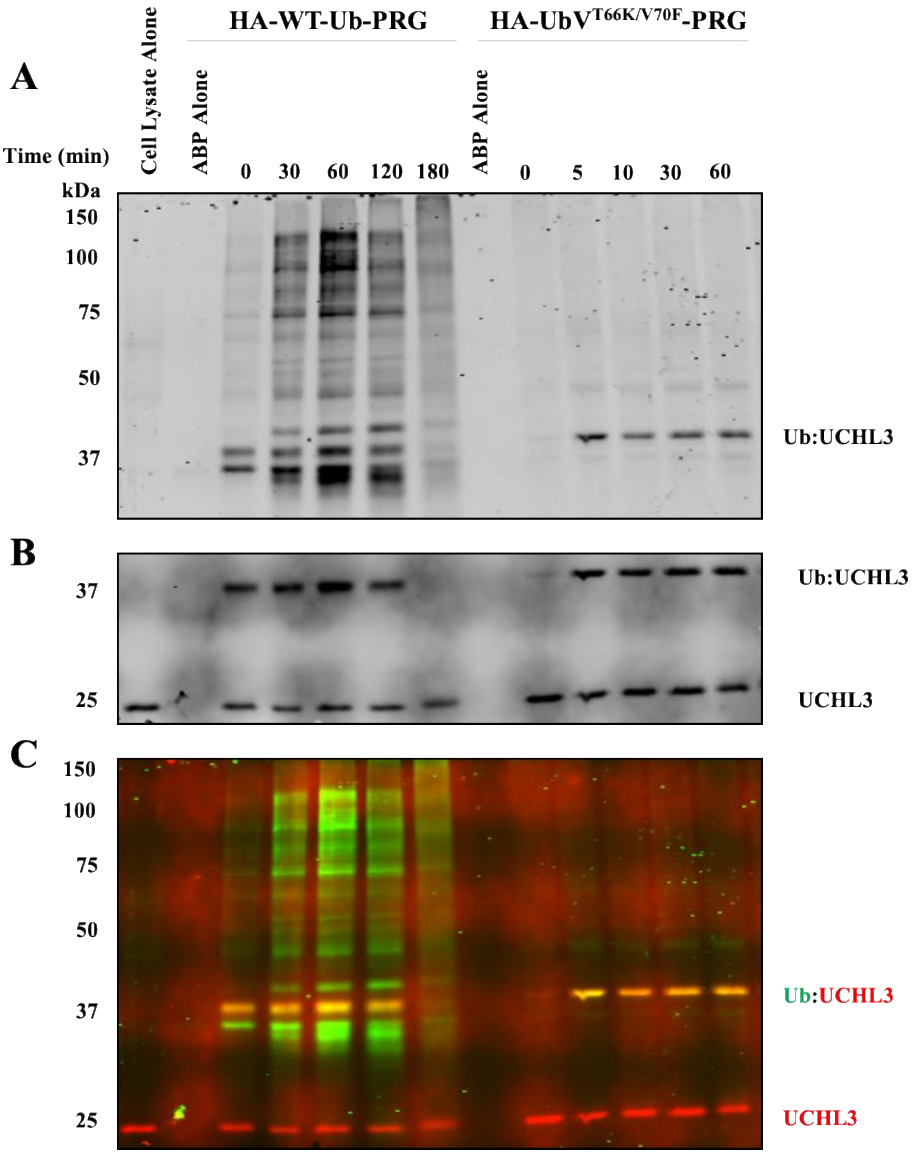

Figure 3.4 Time Dependent Western Blot Displaying UCHL3 Selectivity of HA-UbV$^{T66K/V70F}$-PRG.0.5 µM HA-WT-Ub-PRG or HA-UbV$^{T66K/V70F}$-PRG was incubated with 1 mg/mL HEK293 cell lysate at 37°C for the times indicated above the wells. A) Hemagglutinin (HA) immunoblot displaying Ub-PRG reactivity with DUBs. B) UCHL3 immunoblot displaying Ub-PRG reactivity with UCHL3. C) Co-localization blot displaying colocalization of HA (green) and UCHL3 (red).

3.2.5 Rational Design of $UbV^{Q40F/T66K/V70F}$ and $UbV^{Q40V/T66K/V70F}$

$UbV^{T66K/V70F}$-ABPs displayed a high degree of UCHL3 selectivity. However, we wanted to assess whether further modification of the UbV via rational design could improve activity against UCHL3. To do this we utilized the computational program BioLuminate (Schrödinger, LLC) to obtain Ub residues to aid with our rational design of mutants. In this process, Ub residue Gln40 was found to have productive hydrogen bond contacts with UCHL1 whereas with UCHL3 no such contacts existed. More specifically Gln40 has potential hydrogen bond contacts with three proximal residues on UCHL1; Arg153, Asp155, and Arg213 (Figure 3.5B). The closest UCHL3 residues to Ub Gln40 were distal Thr157 and Gln156 residues (Figure 3.5A). Electrostatic potential maps were investigated to observe the charge state of the area where Ub Gln40 interacts with UCHL3 and UCHL1 structures (Figure 3.5C and Figure 3.5D, respectively). From these maps, it was determined Gln40 interacts with a relatively hydrophobic region within UCHL3 and a largely positively charged pocket within UCHL1. With this information it was postulated mutating Ub residue Gln40 to a hydrophobic residue would potentially increase UbV interactions with UCHL3.

To corroborate our hypothesis, BioLuminate change in affinity and stability data was investigated (Table 3.3). Generally, it was determined from our BioLuminate *in silico* mutational analysis that hydrophobic amino acid residues were predicted to have greater affinity (or more negative values) for UCHL3 than hydrophilic residues. We chose Gln40Phe and Gln40Val to represent the aromatic and hydrophobic amino acid residues because of greater predicted affinities of -2.8 and -0.6 kcal/mol against UCHL3, respectively. Additionally, the Gln40Val mutant was predicted to be considerably more stable in complex with UCHL3 over UCHL1 while the Gln40Phe mutant was predicted to be comparable. Moreover, it was reasoned that a Gln40 mutation to a Phe or Val would perturb the binding of Ub to UCHL1 (Δaffinity values with UCHL1 of 1.2 and 4.1 kcal/mol, respectively). These mutations were input into our $UbV^{T66K/V70F}$-Intein vector to allow production of $UbV^{Q40F/T66K/V70F}$ and $UbV^{Q40V/T66K/V70F}$ -ABPs.

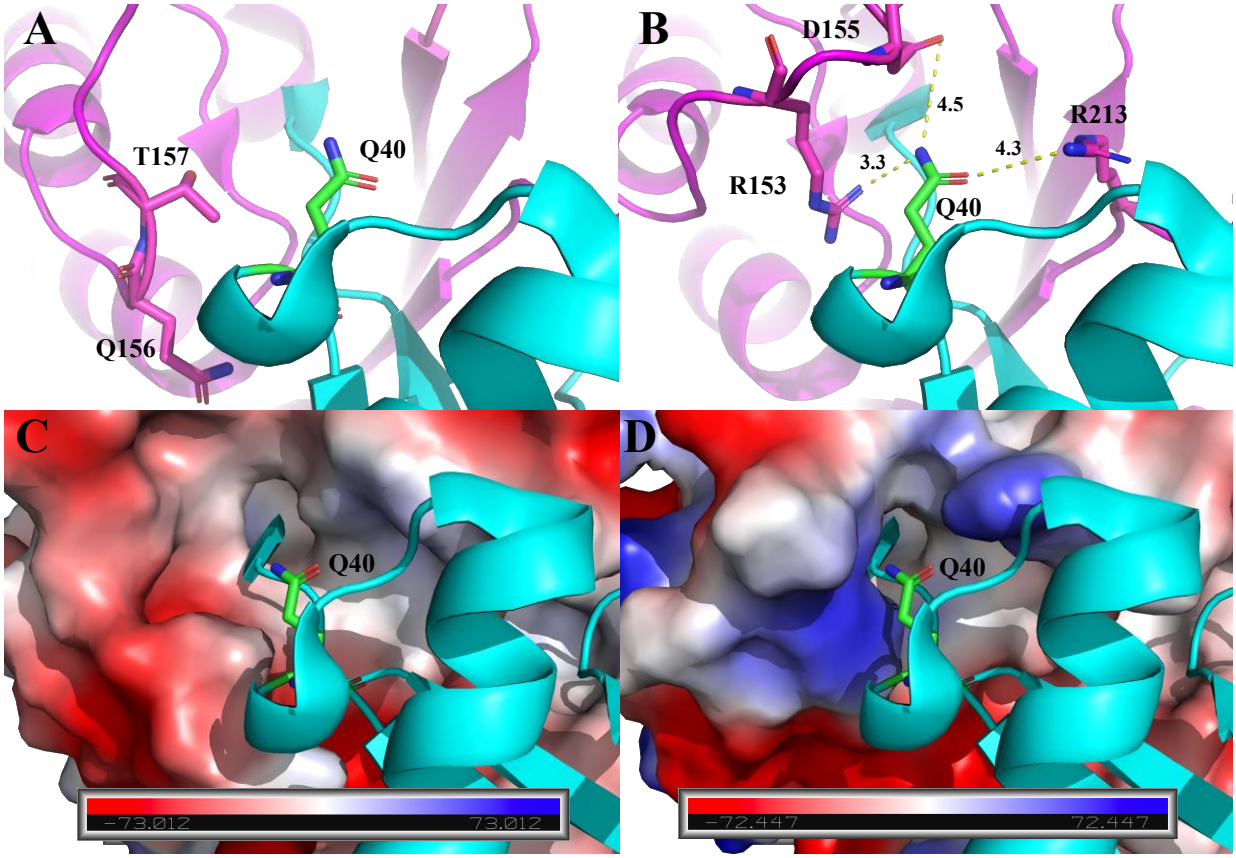

Figure 3.5 Electrostatic Potential Maps and Residue Interactions of Ub Gln40 with UCHL3 and UCHL1.Ub = Cyan, UCHL3/UCHL1 = Magenta A) UCHL3 residues within 6 Å of Ub Gln40 (PDB: 1XD3). B) Potential Gln40 hydrogen bond contacts with residues Arg153, Asp155, and Arg213 on UCHL1 (PDB: 3KW5). Distances are in angstroms. C) Electrostatic potential map of Ub:UCHL3 interaction (PDB: 1XD3). D) Electrostatic potential map of Ub:UCHL1 interaction (PDB: 3KW5).

Table 3.3 BioLuminate ΔAffinity and ΔStability of Ub Mutations to Gln40 Interactions with UCHL3 and UCHL1.A negative Δaffinity value means the Ub mutant binds better than the native Ub protein (calculated using Prime MM-GBSA which uses an implicit solvation model). Negative value of the Δstability means the Ub mutant is more stable than the native Ub protein (calculated using Prime MM-GBSA which uses an implicit solvation model).

Gln40(X); X =	$\Delta Affinity_{UCHL3}$ (kcal/mol)	$\Delta Stability_{UCHL3}$ (kcal/mol)	$\Delta Affinity_{UCHL1}$ (kcal/mol)	$\Delta Stability_{UCHL1}$ (kcal/mol)
Ala	1.0	3.6	6.9	0.2
Arg	-1.2	-2.1	-6.0	3.7
Asn	-0.3	3.1	4.1	3.0
Asp	6.8	7.8	10.2	9.3
Cys	0.0	5.7	4.4	2.4
Glu	4.9	-1.5	5.4	-2.1
Gly	1.7	11.5	7.9	8.0
Hid	-1.1	-1.5	4.6	11.9
Hie	-0.7	3.9	3.4	16.3
Hip	-5.5	0.8	8.1	11.5
Ile	-1.0	-8.7	1.5	-6.6
Leu	-1.1	-2.7	4.7	1.1
Lys	-0.9	13.4	7.6	17.6
Met	-2.0	-11.3	0.2	-11.1
Phe	-2.8	0.8	1.2	-0.1
Pro	-0.2	31.1	3.8	32.2
Ser	0.4	6.8	5.0	3.0
Thr	-0.1	1.4	5.0	-1.6
Trp	-4.2	6.8	75.0	140
Tyr	-2.3	0.8	11.3	65.5
Val	-0.6	-6.0	4.1	-3.6

3.2.6 Binding Characterization of Mono-UbV$^{Q40V/T66K/V70F}$

To assess if the predicted binding affinity and selectivity from Bioluminate would translate to *in vitro* binding the mono-UbV$^{Q40V/T66K/V70F}$ was characterized by performing biolayer interferometry (BLI) and Ub-Rho DUB inhibition assay. Mono-UbV$^{Q40V/T66K/V70F}$ was found to be four times more selective for UCHL3 than UCHL1 based on the BLI steady state K_d determinations (UCHL3 K_d = 49.0 ± 2.9 nM versus UCHL1 K_d = 213.2 ± 9.9 nM, Figure 3.7). Association and dissociation curves and individual BLI experiments are shown in the appendix (Figure A. Corroborating this, the Ub-Rho assay format displays mono-UbV$^{Q40V/T66K/V70F}$ has greater than 100-fold selectivity toward UCHL3 (UCHL3 IC_{50} = 3.5 nM versus UCHL1 IC_{50} = 410 nM).

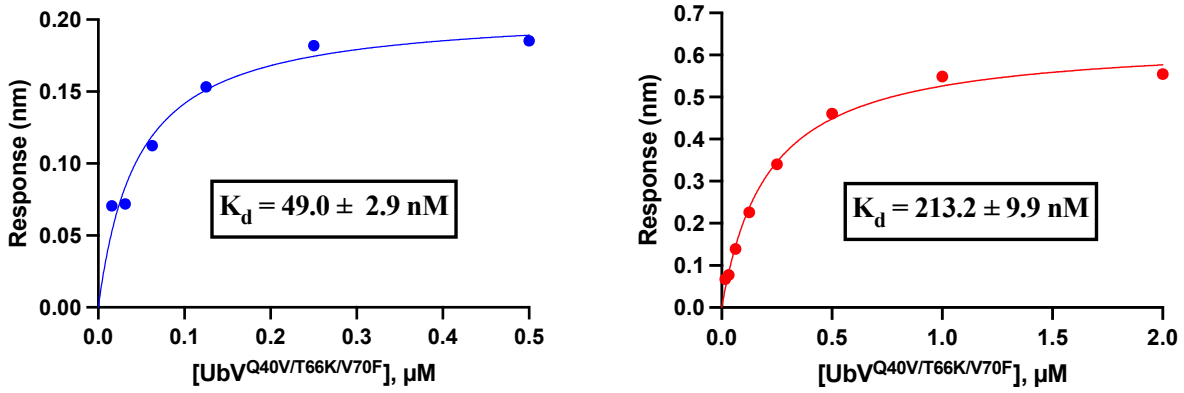

Figure 3.6 Mono-UbV$^{Q40V/T66K/V70F}$ K_d Determinations Utilizing Biolayer Interferometry.(A) Steady-state binding data for His-UCHL3 (B) Steady-state binding data for His-UCHL1

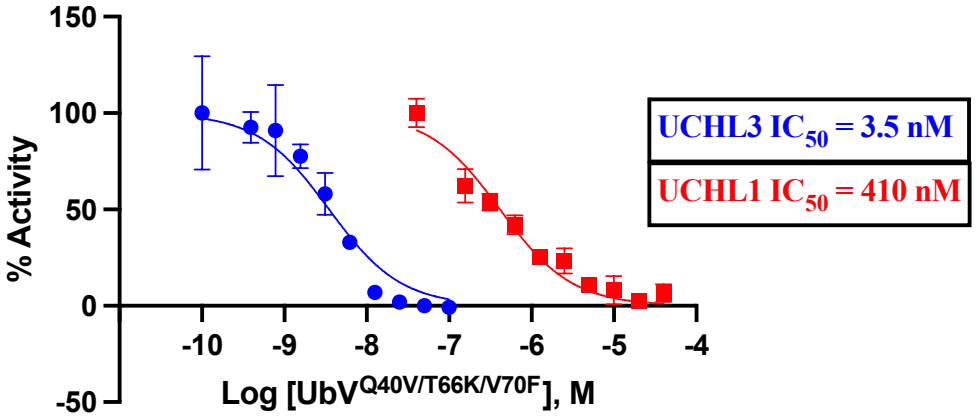

Figure 3.7 UbV$^{Q40V/T66K/V70F}$ Ub-Rho Inhibitory Assay.UbV$^{Q40V/T66K/V70F}$ has >100-fold selectivity for UCHL3 when compared to UCHL1.

3.2.7 Kinetic and Cell Lysate Characterization of $UbV^{Q40F/T66K/V70F}$ and $UbV^{Q40V/T66K/V70F}$ -Activity-Based Probes

The k_{inact}/K_I assays were completed for two UbV triple mutant ABPs (Table 3.4) and compared to WT and $UbV^{T66K/V70F}$-ABPs (progress curves and k_{obs} versus UbV-ABP concentration graphs can be found in Figure A.24-A.25). In comparison to the $UbV^{T66K/V70F}$-ABPs the $UbV^{Q40F/T66K/V70F}$-ABPs had slightly reduced inactivation efficiency against UCHL3 while inactivation efficiency with UCHL1 remained negligible. On the other hand, the valine mutation in $UbV^{Q40V/T66K/V70F}$ -ABPs provided the desired increase for inactivation efficiency against UCHL3 by 4.4-fold over the double-mutant $UbV^{T66K/V70F}$-PRG. The increased inactivation efficiency against UCHL3 also improved the selectivity over UCHL1 to 20,000-fold. Thus, $UbV^{Q40V/T66K/V70F}$-PRG was determined to be the most efficient and selective for UCHL3 and was taken forward into a time-dependent western blot molecular weight gel shift to investigate the UCHL3 selectivity in MDA-MB-231 cell lysate (Figure 3.8). An HA immunoblot displays $UbV^{Q40V/T66K/V70F}$-PRG reacts with a single protein target within 10 minutes and continues to have high selectivity toward this protein for at least 60 minutes (Figure 3.8A). Contrary to the $UbV^{T66K/V70F}$-PRG double mutant presented in figure 3.4, the $UbV^{Q40V/T66K/V70F}$-PRG triple mutant no longer diplays the band at 50 kDa indicating that this UbV is more selective in lysates compared to the double-mutant. A co-localization western blot was performed to confirm this protein was UCHL3 (Figure 3.8B) The unprecedented UCHL3 selectivity in MDA-MB-231 cell lysates by this UbV-ABP provides a useful tool to probe UCHL3.

Table 3.4 k_{inact}/K_I Data for $UbV^{T66K/V70F}$, $UbV^{Q40F/T66K/V70F}$ and for $UbV^{Q40V/T66K/V70F}$-ABPs against UCHL3 and UCHL1.

Enzyme	Electrophilic Warhead	Ubiquitin	k_{inact}/K_I ($M^{-1}s^{-1}$)[a]
UCHL3	VME	WT-Ub	[a]1.6×10^6
		$UbV^{T66K/V70F}$	[b]1.72×10^6
		$UbV^{Q40F/T66K/V70F}$	1.27×10^6
		$UbV^{Q40V/T66K/V70F}$	2.15×10^6
	PRG	WT-Ub	[a]4.79×10^6
		$UbV^{T66K/V70F}$	[b]4.06×10^4
		$UbV^{Q40F/T66K/V70F}$	2.82×10^4
		$UbV^{Q40V/T66K/V70F}$	1.80×10^5
UCHL1	VME	WT-Ub	[a]6.70×10^3
		$UbV^{T66K/V70F}$	[b]1.38×10^2
		$UbV^{Q40F/T66K/V70F}$	1.90×10^2
		$UbV^{Q40V/T66K/V70F}$	5.44×10^2
	PRG	WT-Ub	[a]1.28×10^2
		$UbV^{T66K/V70F}$	[b]3.78×10^0
		$UbV^{Q40F/T66K/V70F}$	9.36×10^0
		$UbV^{Q40V/T66K/V70F}$	9.09×10^0

Reported in Hewitt et al.[31] [b] Presented in Table 3.2 for comparison

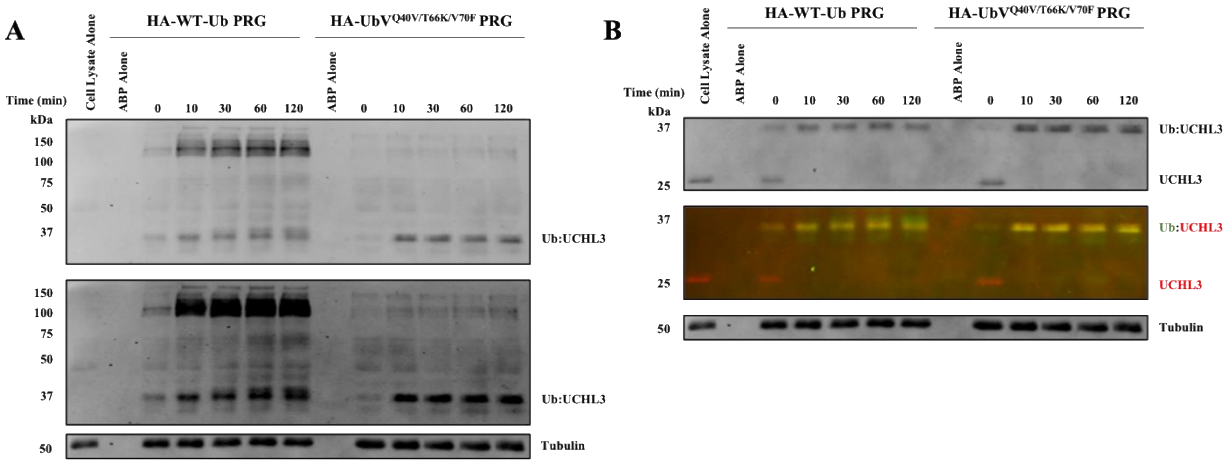

Figure 3.8 Time Course Western Blot Displaying Selectivity of UbV$^{Q40V/T66K/V70F}$-PRG with MDA-231 cell lysates.0.5 µM HA-WT-Ub-PRG or HA-UbV$^{Q40V/T66K/V70F}$-PRG was incubated with 1 mg/mL MDA-MB-231 cell lysate at 37°C for the times indicated above the wells. A) Low and high brightness hemagglutinin (HA) blot, with tubulin loading control immunoblot (Top, middle, and bottom, respectively). B) UCHL3 immunoblot displaying reactivity of Ub-PRG with UCHL3 (top) and colocalization of HA (green) and UCHL3 (red), with tubulin loading control immunoblot (bottom).

3.3 Discussion

The two current inhibitors for UCHL3, TCID and perifosine, have been utilized as UCHL3 probes in several manuscripts without proper characterization of the UCHL3 selective inhibition. In our hands, neither TCID or perifosine are inhibitors for UCHL3, even at concentrations as high as 10 and 50 µM, respectively (Figure 3.3). This provides evidence that TCID and perifosine may not be inhibiting the activity of UCHL3 in the cellular environment. Therefore, there is a dire need for new strategies to probe UCHL3, especially with the recent findings that UCHL3 is involved with DNA repair pathways in cancer. Our previous work describes using the computational program FoldX to rationally design UCHL1 selective UbVs to be used as an alternative to small molecules for inhibition of UCHL1.[31] Additionally, we counter-screened against UCHL3 and chose a UbV that was predicted to be selective toward UCHL3 over UCHL1 for binding and inhibition characterization, UbV^{V70F}. We observed UbV^{V70F} displayed >180-fold selectivity for UCHL3 over UCHL1 in our Ub-Rho inhibition assay format (UCHL3 IC_{50} = 0.54 µM, UCHL1 IC_{50} = >100 µM)

We turned to the crystal structures of Ub:UCHL3 and Ub:UCHL1 to gain an understanding for the selectivity difference of UbV^{V70F} to UCHL3 and UCHL1 (Figure 3.9) and observed key differences are with Ub-bound between the UCHL3 and UCHL1 structures. The Ub:UCHL3 structure (Figure 3.9A) has a Tyr35 residue proximal to the Val70 residue site. Therefore, it is possible that mutating WT-Ub Val70 to a Phe may provide some stability to the Ub:UCHL3 complex by introducing a $\pi - \pi$ interaction. Conversely, at this same location UCHL1 has a Leu residue that may partake in hydrophobic van der Waal's interactions with the Val70 from Ub (Figure 3.9B). Mutation to the aromatic Phe residue may reduce the binding.

The BLI K_d measurements with UbV^{V70F} did not indicate the desired selectivity which was predicted by FoldX (UCHL3 K_d =7,100 nM, UCHL1 K_d = 8,200 nM), however, this selectivity was achieved when measuring IC_{50}s in the Ub-Rho assay format (UCHL3 IC_{50} =540 nM, UCHL1 IC_{50} = >100,000 nM The disparity between the K_d and IC_{50} could be due to the UCH enzyme immobilization because the mutation site is presumably interacting with the internal surface of the UCH proteins. This immobilization could cause changes in the binding and could yield imprecise K_d measurements. An immobilization free method like microscale thermophoresis or isothermal titration calorimetry may resolve this potential issue.

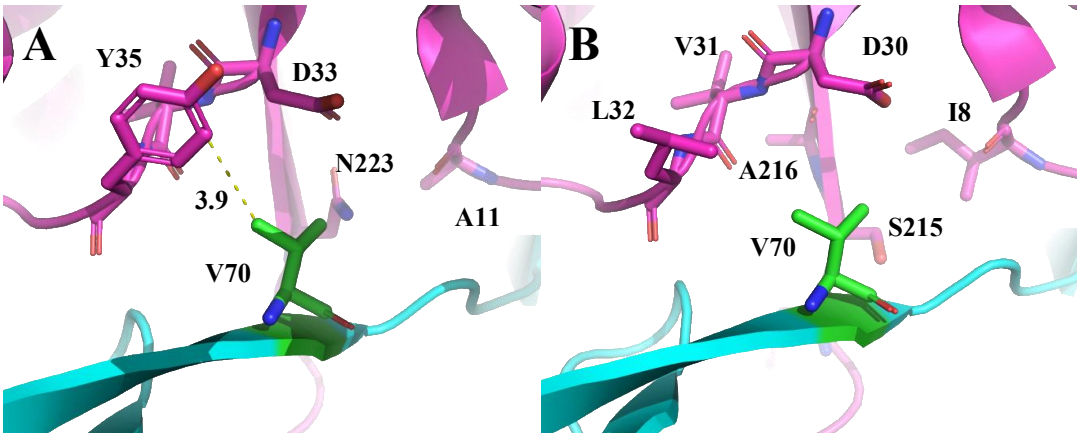

Figure 3.9 Ub Val70 Interactions with UCHL3 and UCHL1.Ub = cyan, Ub Val70 = green, UCHL3 (A) and UCHL1 (B) = Magenta. Distances are in angstroms.

Although the UCHL3/UCHL1 K_d and IC_{50} values were not determined for $UbV^{T66K/V70F}$ or $UbV^{Q40F/T66K/V70F}$, the assays were performed with $UbV^{Q40V/T66K/V70F}$. In Chapter 2 we can demonstrated that the Thr66Lys mutation does not perturb the binding or inhibition potential of UbVs to UCHL3 or UCHL1, thus, we can reasonably deduce the effect of adding a Gln40Val mutation to Ub had on UCHL3 and UCHL1 binding and inhibition by comparing to the UbV^{V70F}.[31] Although the BioLuminate data presented in Table 3.3 suggests $UbV^{Q40V/T66K/V70F}$ would improve binding affinity toward UCHL3 and reduce binding affinity toward UCHL1, our BLI K_d determinations actually showed improved binding affinity values for both proteins (UCHL3 K_d = 49.0 nM, UCHL1 K_d = 213.2 nM) relative to UbV^{V70F} (UCHL3 K_d = 7100 nM, UCHL1 K_d = 8200 nM). As discussed previously, Ub Gln40 interacts with a hydrophobic pocket of UCHL3 and a generally positively charged pocket of UCHL1 (Figure 3.5). Therefore, we predicted substitution of a polar side chain for a hydrophobic side chain with the Gln40Val substitution may increase binding affinity toward UCHL3 through hydrophobic interactions. Unexpectedly, we observed improvement in binding affinity between $UbV^{Q40V/T66K/V70F}$ and both UCHL3 and UCHL1. Thus, even though Gln40 is in proximity with potential hydrogen-bond interacting residues it is possible these interactions are not present in the complex formation and, therefore substitution of the Gln side chain provided the unexpected impact on the *in vitro* binding of $UbV^{Q40V/T66K/V70F}$ to UCHL1.

As was observed with the K_d values the IC_{50} values for $UbV^{Q40V/T66K/V70F}$ (UCHL3 IC_{50} = 3.5 nM, UCHL1 IC_{50} = 410 nM) also both improved in comparison to the corresponding IC_{50}s for UbV^{V70F} (UCHL3 IC_{50} = 540 nM, UCHL1 IC_{50} = >100,000 nM). Thus, even though affinity and inhibition capability for UCHL3 was improved using BioLuminate, the method was not as useful in deriving the desired selectivity over UCHL1. This may be a function of the particular Gln residue in question. Further work needs to be done to identify alternative sites of mutation that may impart the desired binding and selectivity improvements. The combined in vitro binding data is provided in Table 3.5 for comparison.

Table 3.5 Biolayer Interferometry K_ds and Ub-Rhodamine Inhibition Assay IC_{50s} for UbVs with UCHL3 and UCHL1. ND = Not Determined

UbV	UCHL3 K_d (nM)	UCHL1 K_d (nM)	UCHL3 IC_{50} (nM)	UCHL1 IC_{50} (nM)
WT-Ub	430	140	830	410
UbV^{V70F}	7100	8200	540	>100,000
$UbV^{Q40V/T66K/V70F}$	49.0	213.2	3.5	410

While the previous discussion centered on the binding characteristics of the UbV with each DUB the ultimate goal is to develop selective UbV-ABPs that are irreversible covalent inhibitors. Therefore, even though *in vitro* binding metrics do not indicate the desired selectivity the activity of the UbV-ABPs must be characterized by their inactivation efficiencies, or k_{inact}/K_I. In the context of UbV-ABPs the reversible binding of the UbV-ABP to the deubiquitinating enzyme would describe the K_I and the rate of covalent bond formation between the C-terminal VME or PRG groups on the UbV-ABP to the catalytic cysteine would describe the k_{inact} component. Assays were completed to determine the inactivation efficiencies of our UbV-ABPs against UCHL3 and UCHL1 to gain information about the UCHL3 selectivity of our UbV-ABPs. When evaluated in the context of inactivation efficiencies for the $UbV^{T66K/V70F}$-ABPs there was clear selectivity for UCHL3 over UCHL1. $UbV^{T66K/V70F}$-VME exhibited >12,000-fold selectivity for UCHL3 over UCHL1 (UCHL3 $k_{inact}/K_I = 1.72 \times 10^6\ M^{-1}s^{-1}$ compared to UCHL1 $k_{inact}/K_I = 1.38 \times 10^2\ M^{-1}s^{-1}$) while $UbV^{T66K/V70F}$-PRG displayed >10,700-fold selective for UCHL3 over UCHL1 (UCHL3 $k_{inact}/K_I = 4.06 \times 10^4\ M^{-1}s^{-1}$, UCHL1 $k_{inact}/K_I = 3.78 \times 10^0\ M^{-1}s^{-1}$). $UbV^{T66K/V70F}$-VME had similar

inactivation efficiency values compared to WT-Ub-VME whereas $UbV^{T66K/V70F}$-PRG displayed an overall decrease in UCHL3 selectivity relative to the WT-Ub-PRG counterpart.

Upon addition of the third mutation predicted to provide increased binding affinity toward UCHL3, $UbV^{Q40V/T66K/V70F}$-PRG displayed the greatest k_{inact}/K_I selectivity at >19,800-fold UCHL3 selectivity (UCHL3 k_{inact}/K_I = 1.80 x 10^5 $M^{-1}s^{-}1$) over UCHL1 (UCHL1 k_{inact}/K_I = 9.09 x 10^0). This was coupled with unprecedented UCHL3 selectivity in the time-dependent co-localization cellular engagement western blots with MDA-MB-231 cell lysates. The $UbV^{Q40V/T66K/V70F}$-PRG starts solely interacting with UCHL3 in the MDA-MB-231 in 10 minutes and this UCHL3 selectivity remains until at least 60 minutes providing evidence of long lasting UCHL3 selectivity.

3.4 Conclusion

Overall, characterization of the k_{inact}/K_I for $UbV^{T66K/V70F}$-ABPs, $UbV^{Q40F/T66K/V70F}$-ABPs, $UbV^{Q40V/T66K/V70F}$-ABPs with UCHL3 and UCHL1 show these UbV based ABPs are selective for UCHL3 over the closest structural homolog, UCHL1. $UbV^{Q40V/T66K/V70F}$-PRG displayed the most promising UCHL3 selectivity based on k_{inact}/K_I and exhibited a high degree UCHL3 selectivity over broader DUBs based on the MDA-231 cell lysate western blot gel shift assay. These results indicate that a computational approach may be employed to rationally design UbV's with improved binding affinity toward DUBs of interest. However, one must carefully select the residues for mutation based on Ub-binding interactions with proposed off-target DUBs. Clearly we showed the Thr66Lys mutation is capable of abrogating binding to USP family DUBs. However, obtaining selectivity within the same UCH DUB family, at least in terms of binding affinity and inhibition, was more difficult to predict. Alternative sites of mutation need to be assessed to demonstrate the utility of the BioLuminate approach to gaining selectivity within the UCH family in terms of binding affinity. When viewing selectivity through the lens of covalent ABPs, however, the intrinsic reactivity of the DUB active-site cysteine may be advantageous. It has been well established that UCHL3 is more catalytically active than UCHL1, reacting faster with covalent warheads. When electrophilic groups were appended onto the UbV's to provide ABPs, this desired selectivity was observed. Thus, UCHL3 UbV-ABPs represent the most potent and selective strategy to probe the role UCHL3 plays in cancer.

3.5 Experimental

3.5.1 Initial FoldX Design of a UCHL3 Selective mono-Ub Mutant

The UCHL1 and UCHL3 ubiquitin bound crystal structures (PDB ID: 3KW5 and 1XD3) were loaded into YASARA[131] (version 17.8.15) containing the FoldX plugin[112–114] (http://foldxsuite.crg.eu) and energy minimized using the repair object function under the analyze tab to optimize amino acid side chains by improving torsion angles, removing van der Waal's clashes, and minimizing the energy of the structures as suggested by the FoldX protocol. Next an alanine scan was performed across Ub and the predicted change in binding affinity (ΔΔG) for the alanine mutants versus UCHL1 were calculated. Residue positions on Ub that tolerated mutation to Ala while binding to UCHL1 and were at or near the Ub-UCHL1 interface, were prioritized for subsequent position scanning. A position scan of natural amino acids was completed for each prioritized residue position and the predicted ΔΔG of binding for each UCHL1 and UCHL3 were tabulated ($\Delta\Delta G_{UCHL1}$ and $\Delta\Delta G_{UCHL3}$). The change in free energy for each mutant was subtracted to predict the mutations that would impart the largest degree of binding selectivity for UCHL1 over UCHL3 ($\Delta\Delta\Delta G_{selectivity} = \Delta\Delta G_{UCHL1} - \Delta\Delta G_{UCHL3}$). These ΔΔΔG values were utilized to prioritize recombinant ubiquitin mutants to express in *E. coli*.

3.5.2 Generation of Recombinant Proteins

Plasmids and Cloning

All plasmids were ordered from GenScript (Piscataway, NJ) unless otherwise noted. The site-directed mutagenesis and validation of the pRSET-A monoubiquitin plasmid was outsourced to GenScript. Plasmids were transformed into competent BL21(DE3) *Escherichia coli* cells (New England Biolabs, Cat# C2527I) and plated on ampicillin agar plates. Single colonies were picked from the agar plates and grown overnight at 37 °C with shaking at 250 RPM. Glycerol stocks were made from these cultures by mixing 20% glycerol and 80% bacterial culture and stored at -80 °C for future protein expressions.

Recombinant Expression of UCHL1 and UCHL3 Proteins

A pET-15b plasmid construct was used for the expression of both 6x-histidine (His)-tagged UCHL1 and His-UCHL3 in bacterial culture. These plasmids were transformed into competent BL21(DE3) E. coli cells using the procedure previously described. Starter cultures were grown at 37 °C with shaking at 250 RPM overnight. 10 mL of starter culture was inoculated into each liter of autoclaved LB media containing 100 µg/mL ampicillin and grown at 37 °C with shaking at 250 RPM to an OD of 0.4-0.8 before being induced with 300 µL of 1.0 M IPTG. These induced cultures were grown for 18 hours at 18 °C with shaking at 250 RPM. Bacterial cell pellets were spun down at 4000 x g for 20 minutes and resuspended in lysis buffer (1x PBS containing 400 mM KCl). These resuspended bacterial cells were stored in a -80 °C freezer for lysis on a later date or taken directly to lysis by sonication. Lysed bacterial cells were pelleted by centrifugation at 14,000 x g and the supernatant was loaded onto a Nickel-NTA column equilibrated with 1x PBS. After flow through was collected, the column was subject to a 0-500 mM imidazole step gradient and fractions were collected. Both His-UCHL1 and His-UCHL3 eluted from the column at ~150 mM imidazole as evidenced by SDS-PAGE of fractions collected. Fractions that contained the desired protein were pooled together and dialyzed against 1x PBS containing 400 mM KCl with 1.0 mM DTT. This dialyzed protein sample was concentrated down using Amicon Ultra Centrifugal Filters and purified by size-exclusion chromatography (SEC) on an S200 column using running buffer (50mM Tris, 50 mM NaCl, 1mM DTT, pH 7.6). Fractions that contained the protein of interest were concentrated and placed in -80 °C for future experimental use.

Recombinant Expression of UbV Proteins

Mono-ubiquitin variants were purified from a pRSET-A vector. The untagged WT-Ub pRSET-A vector construct was obtained from Dr. Chittaranjan Das (Purdue University). This WT-Ub plasmid was sent to GenScript where site-directed mutagenesis was performed and validated. All UbVs were purified as described above with the following changes. The lysis buffer added to the bacterial cell pellets was 50 mM sodium acetate pH = 4.5. After lysis by sonication, the sample was boiled at 80 °C for 5 minutes to precipitate out the undesired proteins. After centrifugation at 14,000 x g, the pH of the supernatant was measured to be ~5 so it was adjusted to 4.5 with glacial acetic acid to further precipitate out undesired proteins. The precipitated proteins were centrifuged

down at 4000 x g for 8 minutes. Supernatant was loaded onto a countertop SP SepharoseTM Fast Flow (Mono S) column (GE Healthcare, product number 17-0729-10), flow through was collected and the column was subject to a 0-1.0 M NaCl step gradient to elute out the UbVs. The fractions that contained UbVs (determined through SDS-PAGE analysis) were concentrated and further purified by SEC on an S200 column as described above.

Ubiquitin Intein Chitin Binding Domain Expressions

Variations of ubiquitin-intein-chitin binding domain (Ub-intein-CBD) proteins were expressed in a pTXB1 vector (containing an Mxe intein/chitin binding domain sequence). The process was performed for both WT-Ub and UbV. The WT-Ub-intein-CBD was provided by Dr. Chittaranjan Das (Purdue University, West Lafayette) and additions/mutations were made to this construct and validated by GenScript. Lysis buffer for these expressions was a 300 mM sodium acetate buffer containing 50 mM mercaptoethanesulfonic acid (MES) at pH 6.0 (herein referred to as equilibration buffer). After lysis by sonication, cell debris was pelleted as described above and the supernatant was run in a column containing chitin resin (New England Biolabs, Catalog number: S6651S). Equilibration of the chitin column consisted of running 3 column volume (CV) of equilibration buffer through the column prior to column loading. Another 4 CV of equilibration buffer was washed through the column after which equilibration buffer containing 50 mM MES sodium salt (MESNa) was added. This was incubated in the column for 18 hours at 37 °C after which the desired protein was eluted out using the same buffer. The eluted Ub-MESNa sample was concentrated down to ~1.5 mL and stored at -80 °C until further use.

Ub activity-based probes (Ub-ABPs) were constructed by reacting excess glycine-vinylmethyester (VME) or propargylamine (PRG) with Ub-MESNa overnight in 1.0 M sodium bicarbonate containing 150 mg *N*-hydroxysuccinimide (NHS) in a total volume of 10 mL at pH 8.0 (to mitigate MESNa hydrolysis). This was dialyzed into 50 mM sodium acetate buffer pH 4.5 and run on a Mono S column to separate out the reacted species. The fractions that contained ubiquitin species of interest were determined by reaction with UCHL1 for 30 minutes at 37 °C and a subsequent SDS PAGE analysis.

3.5.3 Binding Characterization

Binding Affinity Measurements using Biolayer Interferometry

Ub and UbV binding affinity was measured according to a previously reported protocol[108] with minor changes, mainly our method utilized Ni-NTA coated biosensors (Molecular Devices, Part Number 18-5101) rather than streptavidin coated sensors. Initial concentrations of the UCH proteins were determined by A280 on NanoDrop™ (ThermoScientific) after which His-UCHL1 and His-UCHL3 were diluted into BLI buffer (1x PBS containing 0.05% v/v tween 20 and 0.1% w/v bovine serum albumin (BSA)) to concentrations of 25 µg/mL and 100 µg/mL, respectively, to achieve the similar loading in BLI assay. UbVs were buffer exchanged into 1x PBS using 0.5 mL Zeba™ spin desalting columns (ThermoScientific, catalog number 89882). The concentration of the UbVs was determined by BCA assay and diluted to top concentrations into BLI buffer and 1:1 serial dilutions were completed. Top concentrations differed in assay set-ups based on expected K_d from of UbV to UCH protein. 40 µL of each solution was added to a 384 tilted-bottom well plate (Molecular Devices, Part Number 18-5080). One Ni-NTA biosensor was used for each K_d measurement, dipping first into BLI buffer (initial baseline, 60 seconds), then the His-UCH protein wells (loading step, 300 seconds), then into BLI buffer alone (baseline step, 60 seconds) followed by dipping into lowest concentration of UbV (association step, 120 seconds) then into buffer alone (dissociation step, 100 seconds). A reference sensor of loaded with protein was dipped into buffer only containing wells to adjust for protein-buffer signals. The association-dissociation was repeated with increasing concentration of UbV. All measurements were taken at 30 °C.

Biacore Data Analysis Software (version 8.2) was used to collect and analyze the raw data for the association and dissociation curves. After subtraction of a reference sensor (loaded sensors dipped into buffer only containing wells), averages of the association responses (in nm response signal from 110 seconds – 115 seconds) was calculated and plotted as a function of UbV concentration in Prism 8. These data were fit to a non-linear regression one site – specific binding model to determine a K_d. Non-specific binding of the sensor to Ub (unloaded sensor tip dipped into Ub containing wells) was checked with WT-Ub. Negligible non-specific signal was observed at a concentration of 2 µM WT-Ub (not shown).

UCH Inhibition Assays

UbVs were buffer exchanged into 50 mM Tris-HCl containing 0.5 mM EDTA pH 7.6 using 0.5 mL Zeba spin desalting columns (ThermoScientific, catalog number 89882). The concentrations of each UbV were determined by BCA assay and were diluted to the 5x top assay concentrations in activity assay buffer (50 mM Tris, 0.5 mM EDTA, 0.1% bovine serum albumin, 5 mM DTT at pH 7.6). 5x top assay concentrations differed for each UbV based on expected IC_{50}. 1:1 serial dilutions of 5x top assay concentrations for each UbVs were completed in activity assay buffer. His-UCHL1 and His-UCHL3 proteins were diluted into activity assay buffer and 20 µL of 2.5 nM His-UCHL1 and 0.25 nM His-UCHL3 were added to wells of a black 384-well plate (Fisher Scientific, product number 12566624) and incubated with 10 µL of a 5x concentrations of UbV for 30 minutes. The difference in enzyme concentration was due to activity differences in the enzymes and necessary to obtain a readout in the linear range for analysis. 450 nM stock of ubiquitin rhodamine110 (Ub-Rho) was made and 20 µL of this stock was added to the assay wells directly before fluorescent measurements were recorded using a Synergy Neo2 Multi-Mode Reader (Biotek) at excitation and emission wavelengths = 485 nm and 535 nm, respectively. Initial slopes were identified and plotted using Prism 8. The control (wells containing only activity assay buffer/no ubiquitin inhibitor) was normalized to 100% enzyme activity and the sample wells were calculated at percent activity compared to the control.

3.5.4 DUB Cell Engagement Assays

DUB engagement assays were performed according to previously published protocols with minor changes.[125] Cell pellets were lysed in 50 mM Tris-HCl buffer (pH 7.4) containing 150 mM NaCl, 5 mM $MgCl_2$, 5 mM DTT, 2 mM ATP, 0.5% NP-40, and 10% glycerol (herein referred to as cell lysis buffer) for 30 minutes on ice. Every 10 minutes the incubating cells were vortexed for 10 seconds to ensure homogeneous lysis. Cell lysates were clarified by centrifugation at 13,000 x g for 10 minutes and the supernatant was collected. Protein concentrations of clarified cell lysates were determined using Bradford assay and each sample was brought to a concentration of 0.5 mg/mL in cell lysis buffer. Initial hemagglutinin (HA) tagged Ub-Activity-Based Probe (ABP = vinyl methylester or propargylamine) concentrations were determined by A280 on a NanoDrop™ (ThermoScientific) system and diluted to 10 µM in cell lysis buffer. Concentration determinations

by A280 measurements were performed with all HA containing Ub and UbVs because of the higher extinction coefficient provided by the HA sequence (leading to more accurate protein concentrations), relative to the mono-ubiquitins. 1 part of 10 µM HA-Ub-ABP was added to 19 parts of 0.5 mg/mL cell lysate and incubated in a heat block at 37 ºC for the times stated. 4x Laemmli buffer was added to the samples to terminate the reaction at each timepoint. For the dose dependency blots, 1 part of 20x concentration of HA-Ub-ABP was added to 19 parts of 0.5 mg/mL cell lysate and incubated in a heat block at 37 ºC for the times stated. 10 µL of each sample was loaded onto a 12% SDS-PAGE gel and run at constant 190V for ~ 75 minutes. Gels were transferred to a nitrocellulose membrane and subjected to western blot procedures. Primary antibodies used were HA-Tag - 6e2 (Cell Signaling Technologies), C29F4 (Cell Signaling Technologies), Ab18181 (Abcam); UCHL3 – D25E6 (Cell Signaling Technologies), Ab126621 (Abcam); Alpha Tubulin – Ab7291 (Abcam) or Ab176560 (Abcam). Fluorescent secondary antibodies (Licor IRDye 680RD Goat anti-Rabbit and Licor IRDye 800CW Goat anti-Mouse) were used. Images were collected on a Licor Odyssey system.

3.5.5 Ubiquitin Activity Based Probe k_{inact}/K_I Assays

The k_{inact}/K_I is a metric that is relevant for irreversible inhibitors as the efficacy of the covalent bond formation is dependent on the rate of the bond forming reaction as well as the ligand binding to the target. The k_{inact}/K_I describes the potency of the first reversible binding event in the inhibition constant (K_I) and the maximum rate of inactivation (k_{inact}). To obtain this data His-UCHL1 and His-UCHL3 enzymes were diluted to 2.5 nM and 0.25 nM stock solutions, respectively, in 50 mM Tris-HCl (pH = 7.6) buffer containing 0.5 mM EDTA, 5 mM DTT, and 0.1% w/v BSA. HA-WT-Ub-ABPs and HA-UbV-ABPs underwent 1:1 serial dilutions from a top concentration in the same buffer. The UCH enzyme concentrations were optimized to obtain a dynamic range for progress curves for k_{obs} determinations. Ub-Rho (Boston Biochem, catalog number U-555) was diluted to 450 nM in the same buffer to make the Ub-Rho stock. 20 µL of Ub-Rho stock solution was first added to each well in a 384-well plate followed by 10 µL of HA-WT Ub ABP or HA-UbV ABP. To initiate the reaction, 20 µL of each respective enzyme stock solution was added and fluorescence measurements were immediately recorded on a Synergy Neo 2 Multi-Mode Reader (BioTek) at excitation and emission wavelengths of 485 nm and 535 nm, respectively. Progress curve raw data was input into Prism 8 and a baseline correction analysis was completed to obtain

all the time = 0 points at the origin for fitting purposes. Each progress curve underwent fitting to $Y = V_0*(1-e^{(-kobs*t)})/k_{obs}$.[132] The k_{obs} values for each progress curve was graphed against the concentration of HA-WT Ub-ABP or HA-UbV-ABP. The slope of the linear fit was determined to be the k_{inact}/K_I (the rate constant describing the UbVs inactivation efficiency (covalent bond formation on the catalytic cysteine) on the UCH enzymes resulting from the potency (K_I) of binding and the maximum potential rate of inactivation (k_{inact}).

CHAPTER 4. INVESTIGATIONS INTO UB BINDING TO UCHL1

The following chapter was adapted with permission from the following manuscripts.

Sheedlo M.J., Kenny S., Podkorytov I.S., Brown K., Ma J., Iyer S., Hewitt C.S., Arbough T., Mikhailovskii O., Flaherty D.P., Wilson M.A., Skrynnikov N.R. Das C., Biochemistry 2021, 60, 8, 584-596, © 2021 American Chemical Society. DOI: https://doi.org/10.1021/acs.biochem.0c00760

Krabill A.D., Chen, H., Hussain S., Hewitt C. S., Imhoff R.D., Muli C.S., Das C., Galardy P.J., Wendt M.K., Flaherty D.P., Molecules 2021, 26(5), 1227, © 2021 MDPI. DOI: https://doi.org/10.3390/molecules26051227

4.1 Introduction

Our expertise in experimentally determining the binding of Ub to UCHL1 was utilized in two collaborative efforts involved with 1) further exploring the mechanism of Ub:DUB binding/substrate release and 2) supporting the characterization of VAEFMK, a peptide based UCHL1 inhibitor, to validate its potential to be used as a probe for UCHL1. For the first collaborative project, biolayer interferometry was completed to investigate the binding of Ub to WT-UCHL1 and UCHL1^{C90A} to determine if the post cleavage product negatively charged C-terminus of Ub caused electrostatic repulsion and aided in Ub substrate release. The hypothesis for this experiment was that Ub UCHL1^{C90A} would have increased affinity toward UCHL1^{C90A} compared to WT-UCHL1. For the second collaborative effort, biolayer interferometry was also utilized to elucidate if VAEFMK binding could perturb Ub binding to UCHL1. Below are descriptions and discussions of the data generated.

4.2 Ubiquitin Substrate Release Introduction

In substrate recognition, DUBs differ significantly from digestive proteases, such as trypsin and chymotrypsin, and many other proteases that engage their substrates only at local regions adjacent to their preferred cleavage sites. For general proteases, substrate recognition hinges largely on one specific side chain or a few specific side chains in the context of a disordered polypeptide segment. In contrast, DUBs engage a sizable portion of their ubiquitinated protein

substrate through extensive protein–protein interactions with the Ub portion of the substrate-Ub complex, which enables precise placement of the scissile isopeptide bond beneath the catalytic group. As a result, although they invariably cleave after the LRGG motif in the flexible C-terminal tail of Ub, this motif must be presented in the context of an intact Ub. The products of the hydrolysis reaction are a readily dissociating protein leaving group that departs as the amino fragment and the acyl-enzyme thioester intermediate, involving Ub and DUB. This intermediate is subsequently hydrolyzed, releasing the Ub carboxylic fragment and the restored enzyme.[138]

Interactions of DUB with the Ub portion of the substrate are fairly substantial, burying in some cases up to 1900 $Å^2$ of accessible surface area yet upon product formation, the Ub fragment is released and the free enzyme is regenerated for an additional catalytic cycle. It is conceivable that the resulting negatively charged carboxylate group on $Gly76^{Ub}$ from the hydrolysis reaction might be drive dissociation of Ub from the DUB by other negatively charged active-site residue(s) through electrostatic repulsion. The proximity of the newly formed carboxylate with these residues could weaken Ub binding and thereby facilitating product release. A likely candidate for such a repulsive residue would be the catalytic Cys itself owing to its proximity to the newly generated Ub carboxylate group and its expected ionization state as a catalytic thiolate ion (Figure 4.1).

4.3 Ubiquitin Substrate Release Results

The mechanism by which Cys-protease DUBs cleave Ub from a target protein is akin to the catalytic mechanism of papain-like Cys proteases proceeding through nucleophilic addition and elimination steps.[139] The nucleophilic thiol group of the DUB's catalytic cysteine attacks the carbonyl group of the isopeptide (or peptide) bond at the C-terminal $Gly76^{Ub}$, leading to an acyl-enzyme thioester intermediate (Ub-enzyme thioester intermediate), with concomitant departure of the target protein as the amine fragment (Figure 5.1). This step is followed by addition of the catalytic water to break the thioester bond, resulting in regeneration of the catalytic thiolate and a noncovalent complex of enzyme bound to the Ub-carboxylate (Ub-COOH) product. The Ub product fragment must be released from the enzyme for subsequent rounds of catalysis (Figure 5.1).

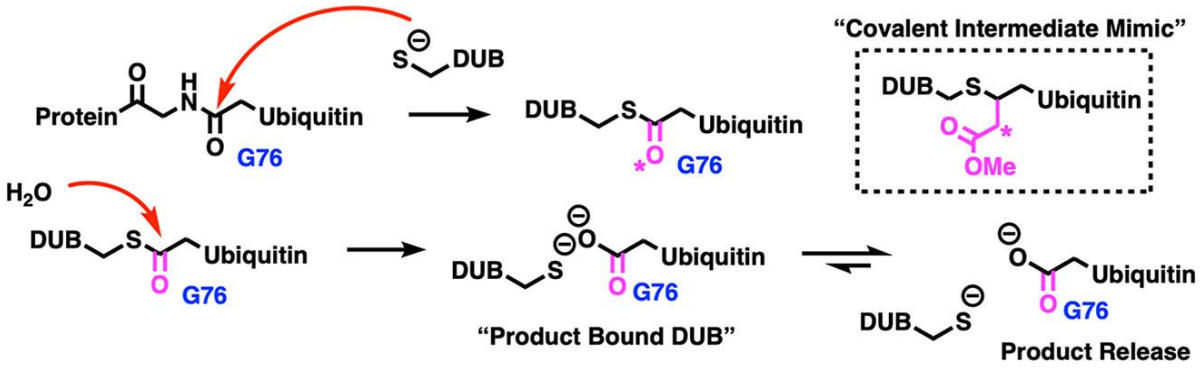

Figure 4.1 Deubiquitination mechanism of DUBs.The catalytic cysteine of the DUB acts as a nucleophile to form a thioester intermediate with the carboxy terminus of Ub. This thioester intermediate can be mimicked by a Ub-VME-linked DUB as shown in the inset above. Hydrolysis of the thioester results in the formation of the Ub product fragment remaining noncovalently associated with the DUB. In this product complex, the charged forms of the catalytic cysteine and the carboxy terminus of Ub may give rise to repulsion facilitating product release. The asterisk indicates the correspondence between the physiologically relevant acyl-thioester intermediate and the VME-based model thereof.

To test if electrostatic repulsion between the catalytic cysteine of DUB and the C-terminal carboxylate of Ub is a general mechanism of product release we turned to BLI to measure binding of this DUB and its mutant to Ub. Although the difference in binding affinity was marginal in the case of UCHL1, 193 nM for the WT enzyme versus 156 nM for the C90A mutant, the trend was consistent with the presumed role of electrostatic repulsion (Figure 4.2 and Table 4.1). The binding of WT-UCHL1 to Ub is already strong and represents one of the highest-affinity interactions known between a DUB and Ub. Alanine substitution here produces only a modest further enhancement compared to the existing tight binding between the WT enzyme and Ub.

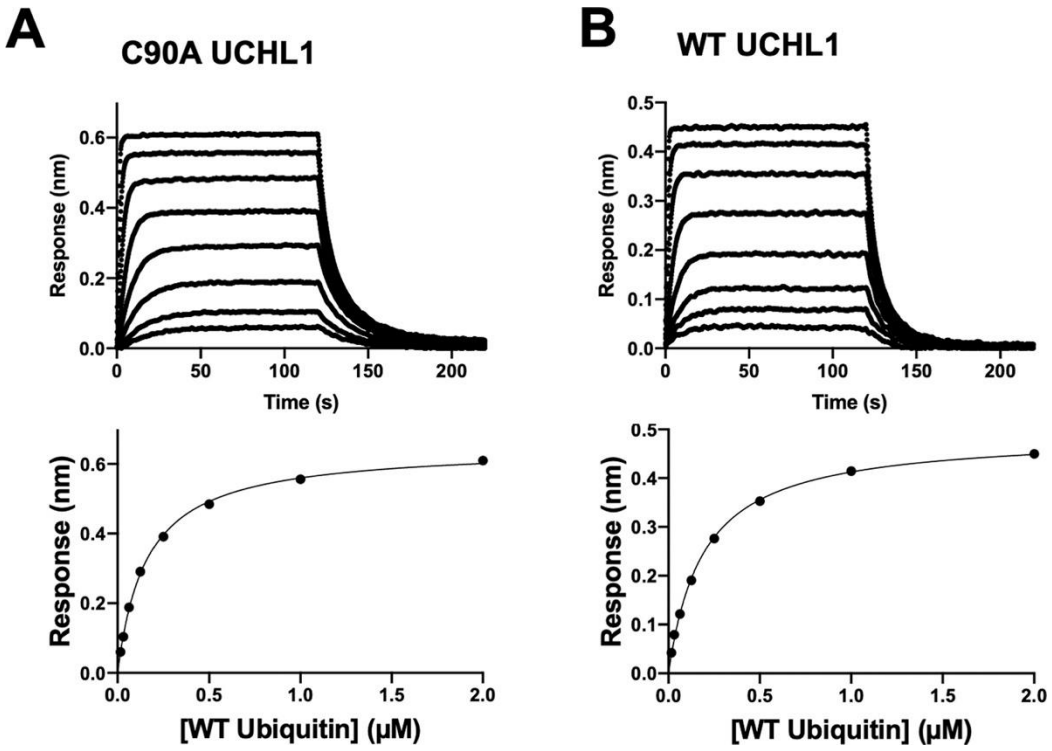

Figure 4.2 Biolayer interferometry measurements of UCHL1 binding to Ub.(A) Association–dissociation curves for binding of UCHL1(C90A) to Ub. Steady-state kinetics (bottom) was used to determine the binding constant. (B) Association–dissociation curves for binding of WT UCHL1 to Ub. Steady-state kinetics (bottom) was used to determine the binding constant. The measurements conducted in triplicate produce average binding constants of 193 ± 4 nM for WT UCHL1 vs 156 ± 1 nM for the C90A mutant.

Table 4.1 Kinetic binding parameters were obtained from BLI data for UCHL1-Ub binding

UCHL1	k_{on} ($\mu M^{-1}s^{-1}$)	k_{off} (s^{-1})	K_D (nM)
WT UCHL1	0.539	0.104	193
UCHL1 C90A	0.455	0.071	156

4.4 Ubiquitin Substrate Release Discussion

While our work was in progress, Morrow et al. reported a study of a catalytic Cys-to-Ala mutants of the SAGA DUB module Ubp8, OTUD1, and USP14 (along with others).[140] These studies highlighted the effects of the Cys-to-Ala mutation in the context of the cellular environment.

In all of these cases, a higher affinity for Ub was observed when the catalytic Cys was mutated to Ala, while the increase in the affinity was more pronounced in some DUBs compared to others. Our results are in agreement with that report. We observed a marginal but apparent increase in binding affinity due to the Ala substitution at the catalytic Cys90 of UCHL1. This increased binding affinity was more apparent with another deubiquitinating enzyme, $SdeA_{DUB}$, in which ITC was utilized to see a difference in binding affinities. It is possible that the range of affinity gained upon Cys-to-Ala mutation reflects a difference in the extent to which the repulsion might be tolerated, which in turn will depend on the details of the active-site microenvironment. Morrow and co-workers attributed the affinity enhancement observed in the Ala mutants to an absence of a steric clash between the side chain of the catalytic Cys and the terminal carboxylate group of the Ub product.[140] In the absence of the steric conflict, the carboxylate group would establish favorable interactions within the active-site pocket, giving rise to a higher affinity of the mutant with Ub. While alanine substitution decreases the size of the side chain, the Ala mutant would also be devoid of any charge that may otherwise be expected of the thiol group in the catalytic Cys. Thus, the electrostatic effects should be considered as a contributing factor underlying the higher affinity of the Ala mutant.

4.5 UCHL1 Peptide Based Inhibitor (VAEFMK) Introduction

The previous gold standard UCHL1 probe was the reversible inhibitor LDN-57444 (Figure 4.1); however, the utility of this molecule as a UCHL1 inhibitor has been questioned recently as on-target engagement of UCHL1 in cellular environments has not been observed.[56,61] An alternative strategy for targeting UCHL1 is via electrophilic conjugation of the catalytic cysteine, Cys90. A recent set of reversible cyanamide-based covalent inhibitors have been described represented by MT-19 and IMP-1710 (Figure 4.1). MT-19 displayed a UCHL1 IC_{50} value of 670 nM after 30-min pre-incubation while IMP-1710 displayed a value of 38 nM.[60,61] However, these inhibitors may suffer from apparent non-selective toxicity, particularly in non-UCHL1 expressing cells. Krabill et al. showed MT-19 displayed anti-proliferative properties in KMS-12 cell lines that do not express UCHL1, and IMP-1710 began to display cytotoxicity at 10 μM in patient derived human bronchial fibroblasts.[60,61]

The tripeptide benzyloxycarbonyl-Val-Ala-Glu(γ-methoxy)-fluoromethylketone (VAEFMK, 1) (Figure 4.3) represents an alternative class of covalent UCHL1 inhibitor that has

remained unexplored. VAEFMK was originally discovered serendipitously as a hit in a screen of halo-methylketone tripeptides against the herpes simplex virus cysteine protease UL36.[141] However, during counter-screening against a panel of human DUBs, VAEFMK was shown to inhibit UCHL1. The molecule was co-crystallized with UCHL1 by Davies et al., and remains the only ligand-bound UCHL1 complex reported to date.[59] However, there is little biochemical and cellular information reported for this scaffold. Covalent peptides have long been utilized as inhibitors for cysteine proteases including the known caspase inhibitor VADFMK.[142] The fluoromethylketone moiety is less reactive than chloromethylketone and cyanamide counterparts and is an irreversible inhibitor, as opposed to the reversibility of the cyanamides. Thus, we hypothesized VAEFMK would exhibit little off-target non-specific reactivity in cells, making it a suitable starting point for structure-activity relationship (SAR) studies. To this end, our group set out to fully characterize VAEFMK and analogs as a UCHL1 inhibitor. Successfully characterizing this inhibitor would serve to validate this molecular scaffold as a novel probe for UCHL1.

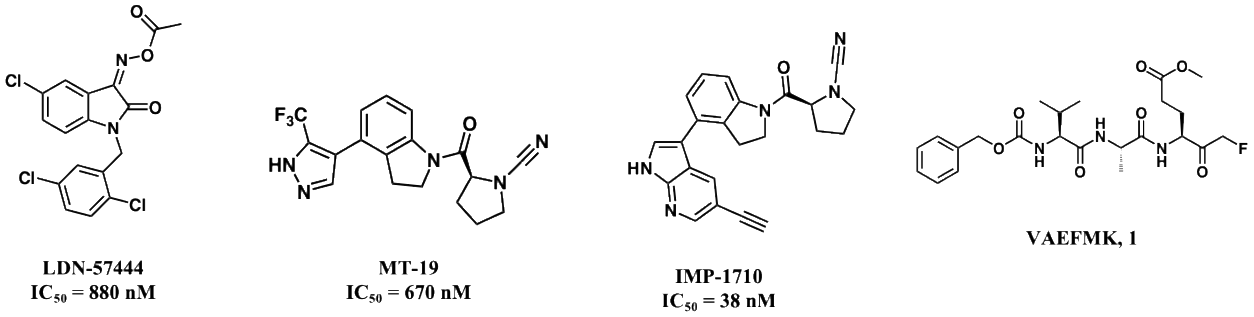

Figure 4.3 UCHL1 Previously reported UCHL1 inhibitors with biochemical IC50 values versus UCHL1.

4.6 VAEFMK Results

4.6.1 VAEFMK Analogs Perturb Ub Binding to UCHL1

In addition to its role as a deubiquitinating enzyme other putative physiological functions for UCHL1 under normal condition are hypothesized to be to (1) maintain a mono-Ub pool within cells and (2) mask sites of activation on Ub through maintaining the Ub-UCHL1 protein-protein interaction (PPI).[28,143–145] Given this, and the relatively strong binding affinity of Ub to UCHL1, it is believed that within cells UCHL1 is mostly bound to free mono-Ub.[146] The crystal structure

of VAEFMK bound to UCHL1 confirms that the inhibitor does not bind to the Ub-binding site of UCHL1, but actually approaches and binds to the face opposite of the Ub-site and interacts with the catalytic cysteine (Figure 4.4A, PDB: 4DM9 and PDB: 3KW5).[30,59] This would potentially still allow the Ub-binding interface to be available to interact with mono-Ub. To determine if VAEFMK is able to abrogate the UCHL1:Ub interaction, Ub-binding studies were carried out using biolayer interferometry (BLI). His-UCHL1 was preincubated with an excess of VAEFMK (2 mM) or DMSO overnight at room temperature to ensure full covalent modification of the Cys90 was achieved. The dissociation constant (K_d) of Ub towards the UCHL1 DMSO treated control was determined to be similar to previously published affinities (Figure 4.4B).[31] However, when UCHL1 was pre-treated with VAEFMK and the Cys90 covalently modified this abolished the ability of UCHL1 to interact with Ub (Figure 4.4C). Taken together, these data suggest that even though VAEFMK binds on the opposite face of UCHL1 compared to the Ub-binding domain it still completely precludes Ub binding. This may be a factor of VAEFMK stabilizing the crossover loop and, in turn, precluding Ub binding; however, further investigation is needed to test this hypothesis. Nonetheless, it appears the inhibition of UCHL1 by the fluoromethylketone analogs would reduce the binding of mono-Ub within the cell to UCHL1.

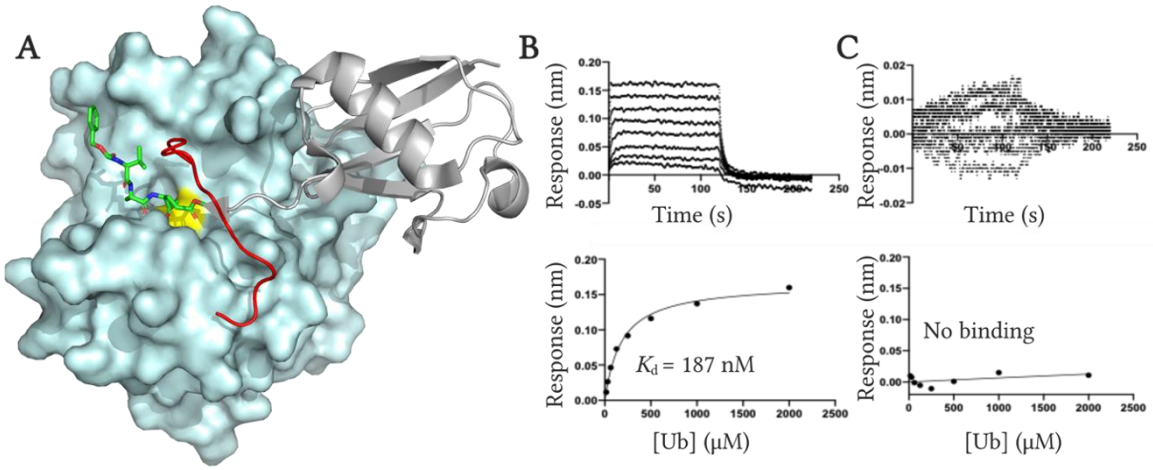

Figure 4.4 Competition of binding for VAEFMK versus Ub.**(**A**)** Overlaid crystal structure of VAEFMK (green sticks) bound to UCHL1 (cyan surface) (PDB: 4DM9) and Ub (gray ribbon) bound to UCHL1 (PDB: 3KW5). Crossover loop of UCHL1 shown in red ribbon for clarity**. (**B**)** Association/dissociation and steady-state binding data for UCHL1 and 1:1 serial dilutions Ub in BLI assay buffer. (C) Association/dissociation and steady-state binding data for UCHL1 after preincubation with VAE-FMK.

4.6.2 VAEFMK Analogs are Specific for the Active Site Cysteine in UCHL1

In addition to the catalytic Cys90 residue, UCHL1 possesses five other cysteines. Among the five alternative cysteine residues Cys152 and Cys220 have known post translational modification and biological activities. (Figure 4.5). Cys152, which resides on the cross-over loop of UCHL1, has previously been reported to exhibit nucleophilic activity toward endogenous electrophiles as well as be involved in trans-nitrosylation events.[147] Additionally, Cys220 has been reported to play a role in farnesylation and AKT signaling.[148–151] A common shortcoming to covalent inhibitors is that the reactive electrophilic groups may partake in non-specific labeling of off-target cysteines. Moreover, if the fluoromethylketone analogs form an adduct with Cys152 this could alter the loop dynamics and provide a possible explanation for why Ub does not bind to the UCHL1-VAEFMK adduct. To investigate if alternative cysteines are affected on UCHL1 we used analog **34** (Figure 4.6) to confirm that the fluoromethylketone derivatives only conjugate Cys90. Analog **34** was determined to be the most potent inhibitor of UCHL1 in a SAR series reported by Krabill et al., having an IC_{50} of 7.7 µM with UCHL1 after 3 hours of pre-incubation.[57] Molecule **34** was incubated with both recombinant wild-type UCHL1 containing Cys90 and a catalytically inactive UCHL1 C90A mutant. This was followed by a click reaction to append a fluorophore then analyzed by in-gel fluorescence imaging. It was observed that analog **34** only formed a covalent adduct with the Cys90 of the WT-UCHL1 while no fluorescent bands were observed for the $UCHL1^{C90A}$ treated protein (Figure 4.7A). Additionally, samples were analyzed by mass spectrometry to increase sensitivity for detection of any non-Cys90 adducts. The mass spectrometry data unequivocally suggests that **34** reacts only with Cys90 of UCHL1 as a single adduct + 486.00 Da was observed that would correspond to the molecular weight of **34** without the fluorine atom (Figure 4.7C, tabular data provided in Table 4.2). There were no adducts observed in the UCHL1 C90A samples incubated with **34** (Figure 4.7D). Table 2 summarizes the mass spectrometry data from the samples tested and confirms that the fluoromethylketone electrophile is selective only for the catalytic Cys90 on UCHL1.

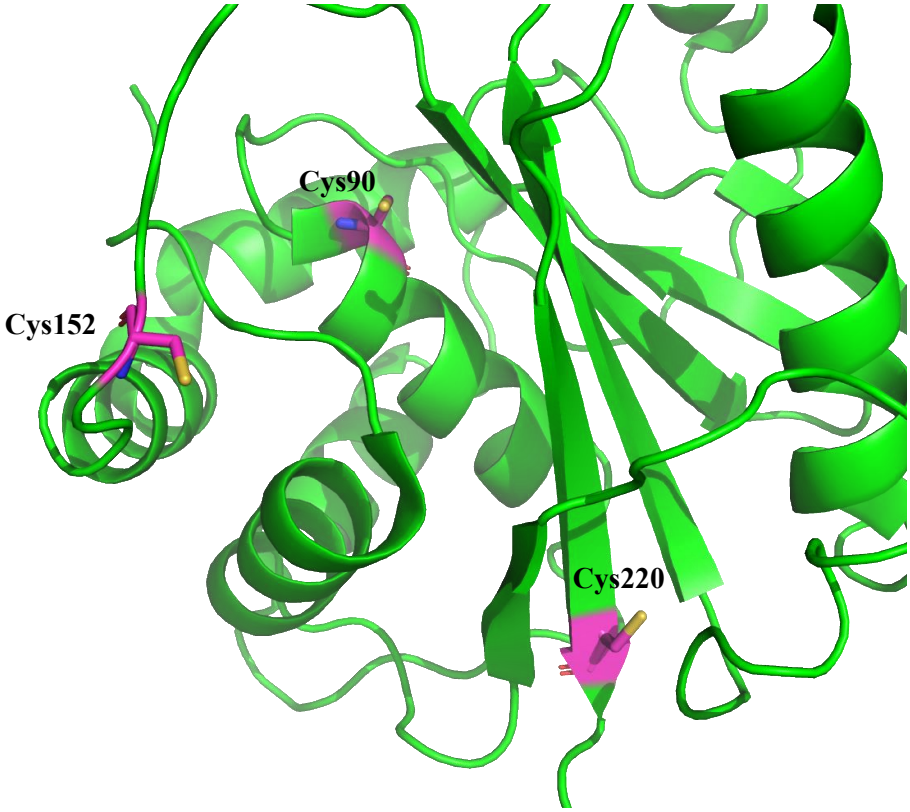

Figure 4.5 Cys90, Cys 152, and Cys220 Residue Locations on UCHL1. Cys residues are colored magenta and UCHL1 (PDB:2ETL) is green.

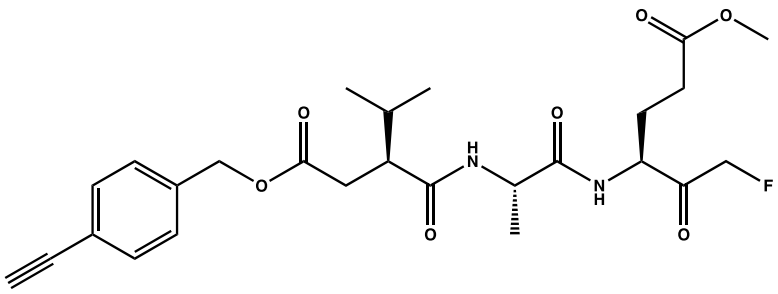

Figure 4.6 Structure of Fluoromethylketone Analog **34**

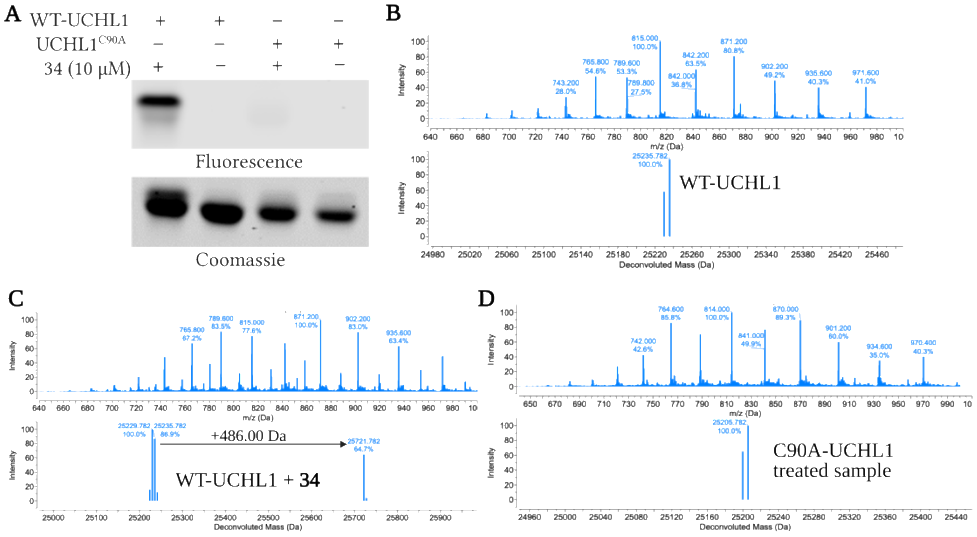

Figure 4.7 Fluoromethylketone **34** selectively conjugates to the Cys90 on UCHL1.(A) Recombinant WT-UCHL1 and catalytically inactive C90A mutant followed click reaction with Cy5-Azide and analyzed by in-gel fluorescence shows the alkyne-tagged analog **34** forms a covalent adduct with WT-UCHL1 but does not form an adduct with the catalytically inactive C90A mutant. Coomassie stain provided as loading control. (B) Deconvoluted mass spectrum for WT-UCHL1 at 10 μM. (C) Deconvoluted mass spectrum for WT-UCHL1 (10 μM) treated with **34** (20 μM). (D) Deconvoluted mass spectrum for C90A-UCHL1 (10 μM) treated with **34** (20 μM).

Table 4.2 Observed Deconvoluted Masses for Recombinant WT- and C90A-UCHL1 treated with Analog **34**

Protein and treatment	Calculated Deconvoluted Masses Observed (Da)[a]	Adduct(s) Observed (Da)
UCHL1	25235.782	none
WT-UCHL1 + **34** (1:1)	25235.782 and 25721.782	+486.00
WT-UCHL1 + **34** (1:2)	25235.782 and 25721.782	+486.00
UCHL1 C90A	25205.782	none
UCHL1 C90A + **34** (1:1)	25205.782	none
UCHL1 C90A + **34** (1:2)	25205.782	none

[a]Average of duplicate samples

4.7 Discussion

` The structural data of UCHL1 conjugated to VAEFMK (PDB: 4DM9) shows the VAEFMK inhibitor bound in the catalytic triad site but distal from the where C-terminus of Ub enters in the Ub bound UCHL1.[59] Due to the structural data on VAEFMK and our knowledge of Ub binding to UCHL1, there is a possibility that even though UCHL1 is inhibited by the covalent inhibitor VAEFMK, it still may be able to carry out its cellular function by binding to mono-Ub. The biolayer interferometry experiments that were performed would suggest that when UCHL1 is inhibited with VAEFMK UCHL1 is unable to bind to Ub. This may be due to stabilization of the crossover loop, however more investigation is needed to mechanistically explain why this abrogation of Ub binding is occurring when UCHL1 is inhibited with VAEFMK.

4.8 Experimental

4.8.1 Ub, UCHL1, and UCHL1^{C90A} Expression and BLI Methods

Expressions of WT Ubiquitin

Mono-ubiquitin variants were purified from a pRSET-A vector. The untagged WT-Ub pRSET-A vector construct was obtained from Dr. Chittaranjan Das (Purdue University). This WT-Ub plasmid was sent to GenScript where site-directed mutagenesis was performed and validated. All UbVs were purified as described above with the following changes. The lysis buffer added to

the bacterial cell pellets was 50 mM sodium acetate pH = 4.5. After lysis by sonication, the sample was boiled at 80 °C for 5 minutes to precipitate out the undesired proteins. After centrifugation at 14,000 x g, the pH of the supernatant was measured to be ~5 so it was adjusted to 4.5 with glacial acetic acid to further precipitate out undesired proteins. The precipitated proteins were centrifuged down at 4000 x g for 8 minutes. Supernatant was loaded onto a countertop SP SepharoseTM Fast Flow (Mono S) column (GE Healthcare, product number 17-0729-10), flow through was collected and the column was subject to a 0-1.0 M NaCl step gradient to elute out the UbVs. The fractions that contained UbVs (determined through SDS-PAGE analysis) were concentrated and further purified by SEC on an S200 column.

Expressions of His-tagged UCHL1 or UCHL1^{C90A}

Recombinant double His-tagged UCHL1 subcloned in vector pET-15b was expressed in the BL21 (DE3) strain of *E. coli* using the same protocol as described above for Ub. The resuspended cells were incubated with lysozyme for 30 min on ice and further lysed using a French press. The cellular debris were pelleted by ultracentrifugation (100000*g*) for 1 h at 4 °C. The protein in the clarified supernatant was purified by Ni^{2+} affinity chromatography using Ni-NTA resin (GE Healthcare), followed by size-exclusion chromatography (Superdex 75). The hexa-histidine tags at the N- and C-termini of UCHL1 were left uncleaved for the purpose of biolayer interferometry (BLI) experiments.

Biolayer Interferometry with UCHL1 and UCHL1^{C90A}

The concentration of the doubly His-tagged UCHL1 proteins (WT and C90A mutant) was determined by the nanodrop absorbance at 280 nm ($\varepsilon = 8970\ cm^{-1}\ M^{-1}$) before diluting the proteins into BLI buffer [1× PBS containing 0.05% (v/v) Tween 20 and 0.1% (w/v) BSA] to a concentration of 0.9 μM. Wild-type ubiquitin was buffer exchanged into 1× PBS using PD10 columns (GE Healthcare). Due to the low extinction coefficient ($\varepsilon = 1280\ cm^{-1}\ M^{-1}$), the concentration of WT Ub was determined by a BCA (bicinchoninic acid) assay; the protein was then diluted into BLI buffer to a concentration of 2 μM. A 1:1 serial dilution of ubiquitin was performed to make the different concentrations of analyte used in the BLI experiment; 40 μL of each Ub solution was transferred to a 384-well tilted-bottom plate. One Ni-NTA sensor was used for

each K_D measurement. His-tagged UCHL1 protein was allowed to load onto the sensor for 300 s. The UCHL1-loaded tip was dipped into wells that contained the lowest concentration of Ub first. Ubiquitin association was monitored for 120 s before the sensor was transferred to the blank buffer and Ub dissociation was monitored for 100 s. The experiments were carried out in technical triplicate at 25 °C, using an Octet RED384 instrument (ForteBio). A reference sensor was also included in each experiment to use as a baseline and thus correct for nonspecific binding. This reference sensor was coated with UCHL1 and dipped into an empty buffer solution. ForteBio Data Acquisition 9.0 software was used to collect raw data for the association and dissociation curves. The data were fitted using nonlinear regression assuming a one-site binding model to determine the K_d value.

4.8.2 VAEFMK Methods

Time Dependent Inhibition Assays

This assay was performed the same as described above with the exception that instead of 3-hour pre-incubation followed by Ub-Rho addition the Ub-Rho substrate was added at 20-minute increments following addition of inhibitor to wells beginning at 0 min and ending at 120 min. Plates were read continuously for 20 min following addition of Ub-Rho. The % activity of each inhibitor concentration was the plotted vs. time of pre-incubation and the slope of this plot is the pseudo first-order rate constant (k_{obs}) for inhibition at each concentration. The k_{obs} was plotted as a function of inhibitor concentration and then fit to the equation $Y = k_{inact}X/(K_I+X)$ to calculate k_{inact}, K_I and k_{inact}/K_I as described by Resnick et al.[132]

Recombinant Protein Expressions

UCHL1, UCHL1^{C90A}, and UCHL3 (Expressed in pET15b by GenScript) for biochemical assays were grown in LB growth medium at 37 °C to an optical density of 0.6–0.8. After 0.1 mm IPTG induction at 17 °C for 18 hours the bacteria were lysed and pelleted at 15,000g, and clarified lysate was purified on HisPur Ni-NTA resin (Thermo Scientific) according to manufacturer's instructions

Biolayer Interferometry with VAEFMK

This assay was carried out according to our previously published protocol using an Octet RED384 biolayer interferometer (ForteBio, Fremont, CA, USA).[31] A solution containing 5 µM His-UCHL1 was incubated with 2 mM VAE-FMK or DMSO overnight in reaction buffer (50 mM Tris pH 7.6, 0.5 mM EDTA, 5 mM DTT) at room temperature before buffer exchanging into water using Zeba spin desalting columns (Thermo Scientific, catalog no. 89882). The concentration of His-UCHL1 was determined by A_{280} on a NanoDrop system (Thermo Scientific), after which His-UCHL1 was diluted into BLI buffer [1× PBS containing 0.05% (*v*/*v*) Tween 20 and 0.1% (*w*/*v*) bovine serum albumin (BSA)]. The concentration of Ub was determined by the BCA assay and diluted to top concentrations into BLI buffer, and 1:1 serial dilutions were completed. The top concentration of Ub was 2 µM. 40 µL of each solution was added to a 384-well tilted-bottom plate (part no. 185080, Molecular Devices, San Jose, CA, USA). The Ni-NTA biosensor was dipped first into BLI buffer (initial baseline, 60 s), then into the His-UCH protein wells (loading step, 300 s), then into BLI buffer alone (baseline step, 60 s), then into the lowest concentration of Ub (association step, 120 s), and then into buffer alone (dissociation step, 100 s). A reference sensor loaded with protein was dipped into wells containing only buffer to adjust for protein-buffer signals. The association-dissociation was repeated with increasing concentrations of Ub.

Octet RED384 Data Analysis Software (ForteBio, version 9.0.0.15) was used to collect and analyze the raw data for the association and dissociation curves. After subtraction of a reference sensor (loaded sensors dipped into wells containing only buffer), averages of the association responses (in nanometer response signal from 110 to 115 s) were calculated and plotted as a function of Ub concentration in Prism 8. These data were fit to a nonlinear regression one-site specific binding model to determine a K_d.

Mass Spectrometry Analysis of Analog 34 Adducts on UCHL1

Solutions containing 10 µM recombinant $UCHL1^{WT}$ or $UCHL1^{C90A}$ (from pET15b) (49 µL) was incubated with either 10 µM or 20 µM inhibitor for 3 hours at room temperature in PBS starting block buffer (Thermo Scientific # 37538). To quench reaction, chilled acetone was added to the sample to achieve an overall 80% acetone solution. After overnight storage at -20 °C, suspension was centrifuged at 14,000 xg at 4 °C for 15 minutes. Supernatant was discarded, and

pellet was dried by vacuum centrifugation for 1 hour. Pellet was reconstituted in 50/50 water/acetonitrile with 0.1% formic acid. 25 pmol per sample was analyzed by LC/MS (Agilent 1260 Infinity II with a ZORBAX Rapid Resolution High Definition 300Å Stable Bond C3, 2.1 x 100 mm, 1.8 µm column) attached to an Agilent 6129 quadrupole mass spectrometer in positive ion mode.

The column was held at 45 °C. Mobile solution A was 0.1% formic acid in water, and mobile phase B was 0.1% formic acid in acetonitrile. The gradient used was hold at 5% B for 5 min, increase linearly to 100% B for 10, and then hold at 95% B for 5 min. The mass data were collected at a range of 500 - 1000 m/z.

Raw data were processed using MestReNova. For all samples, the deconvoluted mass was calculated with a charged state range from 27 to 36, *m/z* range of 670 – 900 Da, and deconvoluted mass range from 25000 – 26000 Da. Representative data had an abundance threshold of 10-20% for charged state deconvolution calculation. For C90A mutant, this abundance threshold was lowered to 5% to detect the presence of any reacted protein. 34 adduct is expected to be +486.00 Da after displacement of fluorine.

CHAPTER 5. CONCLUSION AND FUTURE DIRECTIONS

5.1 Introduction

Since the seminal paper on modulation of deubiquitinating enzyme (DUB) activity by ubiquitin variants (UbVs) was published by Sachdev Sidhu's lab in 2013, additional research groups have pushed to develop deubiquitinating enzyme selective UbVs.[77] Thus far, selective UbVs have been developed for USP8, USP21, USP2a, OTUB1, BRISC, USP7, USP2, USP10, and USP15.[77,79,81,106,107] This dissertation describes the development of selective mono-UbVs toward both UCHL1 and UCHL3 and also a UCHL1/UCHL3 selective UbV activity based probe (ABP) and a highly selective UCHL3 UbV-ABP. Since there are now numerous DUB selective UbVs, there has been an increase in research to produce UbV-based chemical tools to study DUB biology in cells.

5.2 Contribution to Deubiquitinating Enzyme Field

Prior to this work, ubiquitin variants were mainly designed using phage-display technology and focused on the importance of specific Ub residues to DUB binding. The research described in this dissertation utilized rational design aided by structural data computational approaches to generating UbVs that are selective for specific enzymes, UCHL1 and UCHL3, in the UCH subfamily of DUBs. Our work was the first to investigate modifications of residues to specifically improve selectivity to UCH proteins over other homologous enzymes. This work provides a proof of concept that this rational design of UbVs is feasible using both free (FoldX) and proprietary (BioLuminate) computational approaches.

5.3 Future Directions

5.3.1 Development of Cell Permeable UbVs

The greatest hurdle to broad utility of UbV-based chemical tools to study DUB biology in cells is cell permeability of UbVs. Since Ub is an 8.6 kDa protein, it will not cross the cell membrane in its native state. The TAT peptide, R_{10}, and cyclic cell-penetrating peptides (cCPPs) developed by Dehua Pei's lab have all been utilized to get large protein cargos into cells via the

endocytosis.[152–154] Zhihao Zhuang's lab conjugated R_{10} to a modified UbV to develop a photocaged cell permeable Ub probe for temporal profiling of DUBs.[155] This UbV-based tool was utilized for proteome wide profiling of DUBs at various stages in the cell cycle. To our knowledge, conjugation of the R_{10} sequence has not been used to develop a cell permeable DUB selective UbV. A future direction of the project to provide greater utility of these UbVs will be to pursue conjugation of a cCPP to one of our UCHL3 selective UbVs.

Alternatively, it has been observed that masking of surface exposed carboxylic acid residues via diazo compound esterification of proteins can be used to make proteins cell permeable.[156,157] The esterified surface carboxylates are then de-esterified by esterases in the cellular environment to yield the native protein.[156] Our lab has completed proof of concept studies to provide evidence that esterification via this methodology can produce cell permeable HA-WT-Ub-ABPs. The diazo compound (Figure 6.1) was incubated with HEK-293 cells for approximately 4 hours. After treatment, the cells were washed, pelleted, lysed, and a western blot was performed blotting for HA (attached to Ub-VME). Thus, any samples that contained HA bands contained intercellular HA-WT-Ub-VME (Figure 6.1). Cells that were incubated with at least 1 µM diazo conjugated HA-Ub-VME contained HA bands in the cell lysates samples. Although the carboxylic acid residues that are modified by the diazo compound have not fully been characterized, this proof-of-concept study provides evidence of another methodology to produce cell permeable UbVs for development of DUB selective UbV assays.

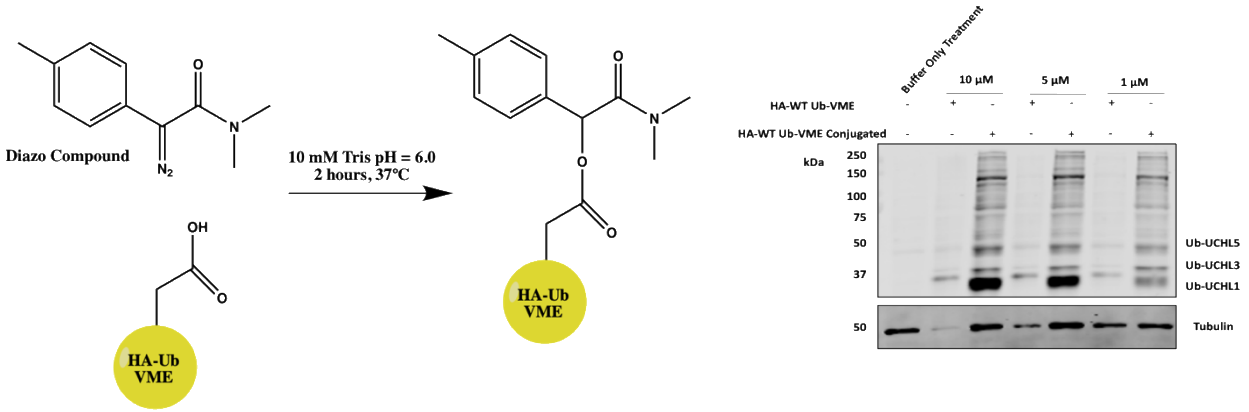

Figure 5.1 Evidence of Diazo Conjugated HA-Ub-VME is Cell Permeable.Left, reaction of diazo compound with HA-Ub-VME, right, western blot (Immunoblotting for HA tag) displays diazo conjugated HA-WT-Ub-VME is cell permeable in HEK-293 cells.

5.3.2 Caged-Luciferin Ubiquitin Variant for Tracking UCH Activity in Cells

Tracking the activity of specific DUBs in cells remains difficult despite the progress made to develop selective Ub-ABPs for specific DUB enzymes. It is our hypothesis that combining our UCH-selective Ub-ABPs with both the aforementioned cell-permeating strategies and a split-luciferin chemiluminescence will provide a UCH selective Ub-ABP that may be used in cells and *in vivo*.[158] D-cysteine (*D*-Cys), and not the natural *L*-Cys, has been shown to spontaneously react with the molecule 6-amino 2-cyanobezothiazole (NH_2-CBT) to produce 6-amino-*D*-luciferin.[159] Our hypothesis is that by appending *D*-Cys to a UCHL3 selective UbV, it will be cleaved off solely by UCHL3 and no other DUB. After cleavage, NH_2-CBT can then be added to luciferase expressing cells to form luciferin and emit bioluminescence. We performed an *in vitro* proof of concept study that involved appending a *D*-Cys onto the C-terminus of one of our UCHL3 selective UbVs to produce HA-UbV$^{Q40V/T66K/V70F}$-(*D*-Cys). The UbV was incubated with varying concentrations of UCHL3 followed by addition of luciferase luminescence was recorded. This assay was performed with different concentrations of both recombinantly expressed UCHL3 and UCHL1 to detect the difference in *D*-Cys cleavage from both enzymes (Figure 6.2). Figure 6.2 displays negligible luminescence from UCHL1 up to concentrations of 10 nM UCHL1, meaning there was neglibile *D*-Cys cleavage from HA-UbV$^{Q40V/T66K/V70F}$-(d-cys). In contrast, UCHL3 exhibited dose dependent cleavage of HA-UbV$^{Q40V/T66K/V70F}$-(d-cys), providing evidence that this assay format can be used with recombinantly expressed proteins and is likely selective for UCHL3.

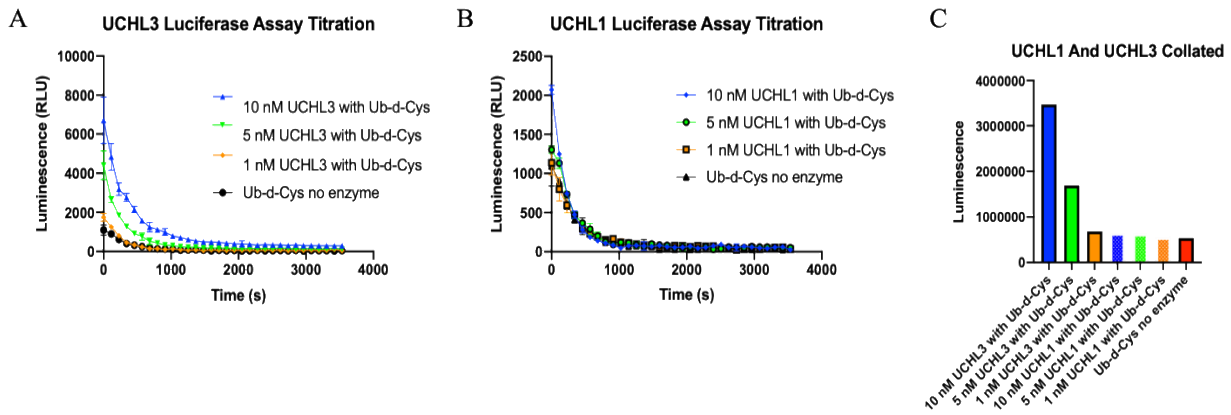

Figure 5.2 Split Luciferase Assay with Recombinantly Expressed UCHL3 and UCHL1 with HA-UbV$^{Q40V/T66K/V70F}$-(d-cys).A) UCHL3 luminescence readings at 10 nM, 5nM, and 1 nM UCHL3 concentrations. B) UCHL1 luminescence readings at 10 nM, 5nM, and 1 nM UCHL1. C) Integration of curves in A and B.

Additionally, for a cellular context, preliminary assays were carried out in MDA-MB-231 cell lysates with varying concentrations of *D*-Cys to investigate if luminescence can be detected to gain an understanding of the concentration of UbV-(d-cys) to produce a detectible luminescence signal. For this assay, 0.5 mg/mL MDA-MB-231 cell lysate was incubated with 100 µM, 50 µM, and 10µM d-cys (adding 4X NH_2-CBT to each reaction) with and without luciferase. Figure 6.3 displays concentrations of at least 50 µM *D*-Cys yield a detectable luminescence signal. Assays using HA-UbV$^{Q40V/T66K/V70F}$-(d-cys) with MDA-MB-231 cell lysates and eventually a cell permeable version of HA-UbV$^{Q40V/T66K/V70F}$ -(d-cys) still need to be completed to verify the applicability of the assay for probing UCHL3 activity in a cellular context. Nonetheless, these preliminary assays provide a proof of concept for the development of an intracellular selective UCHL3 assay.

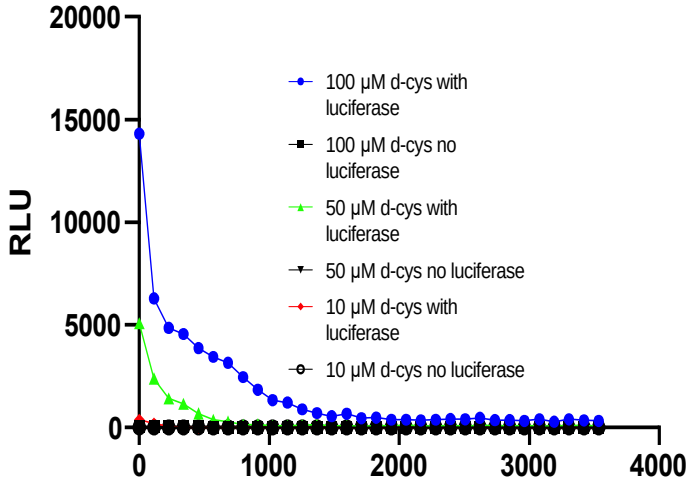

Figure 5.3 Luminescence with 0.5 mg/mL MDA Cell Lysates incubated with 100 µM, 50µM, and 10 µM with or without luciferase.

APPENDIX A. SUPPLEMENTAL FIGURES

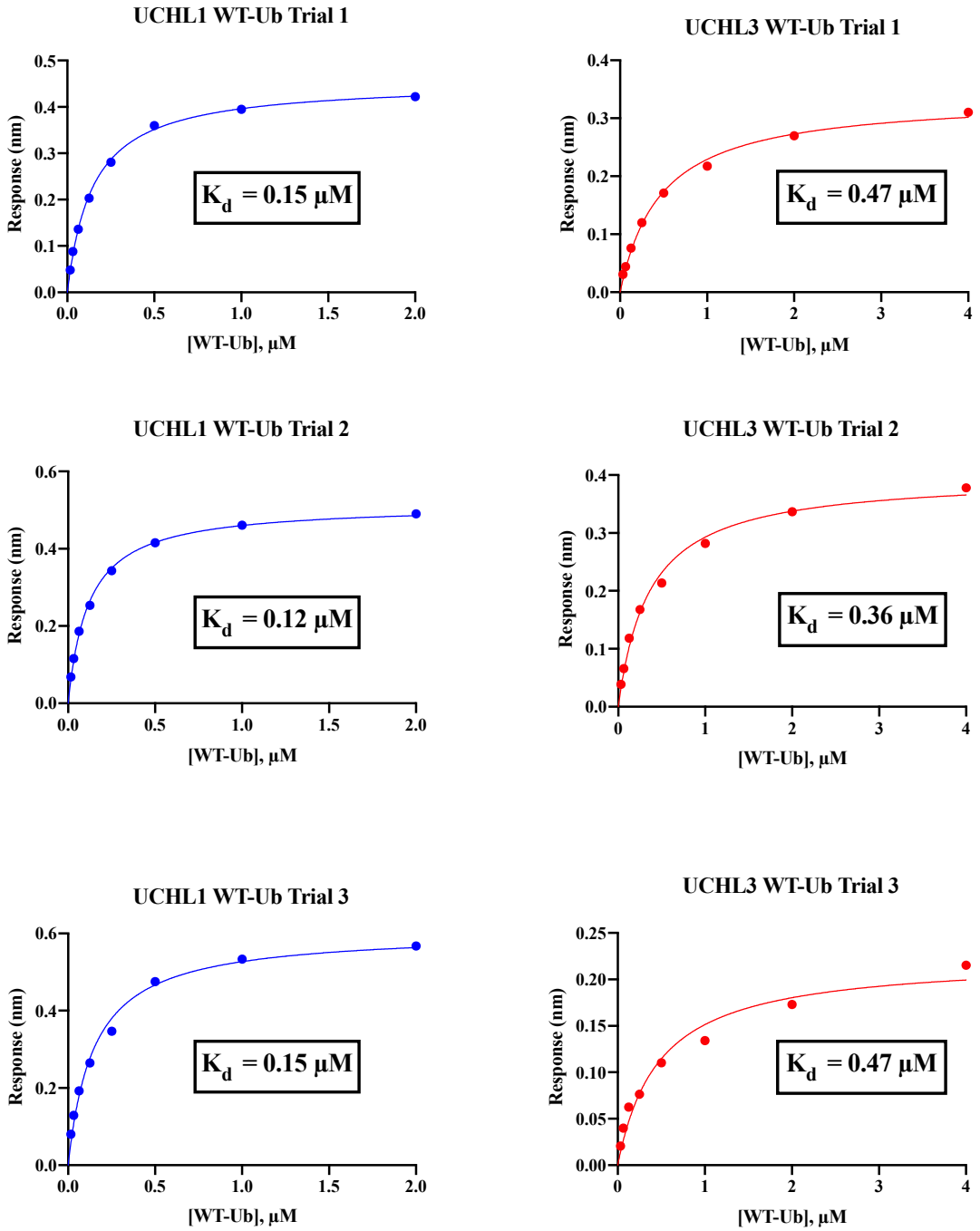

Figure A.1 Biolayer Interferometry Steady State Binding Curves for WT-Ub Binding to His-UCHL1 and His-UCHL3. Individual points were averaged values from 110s-115s of the association step for each trial. K_ds determined by fitting to a 1:1 binding model in Prism 8

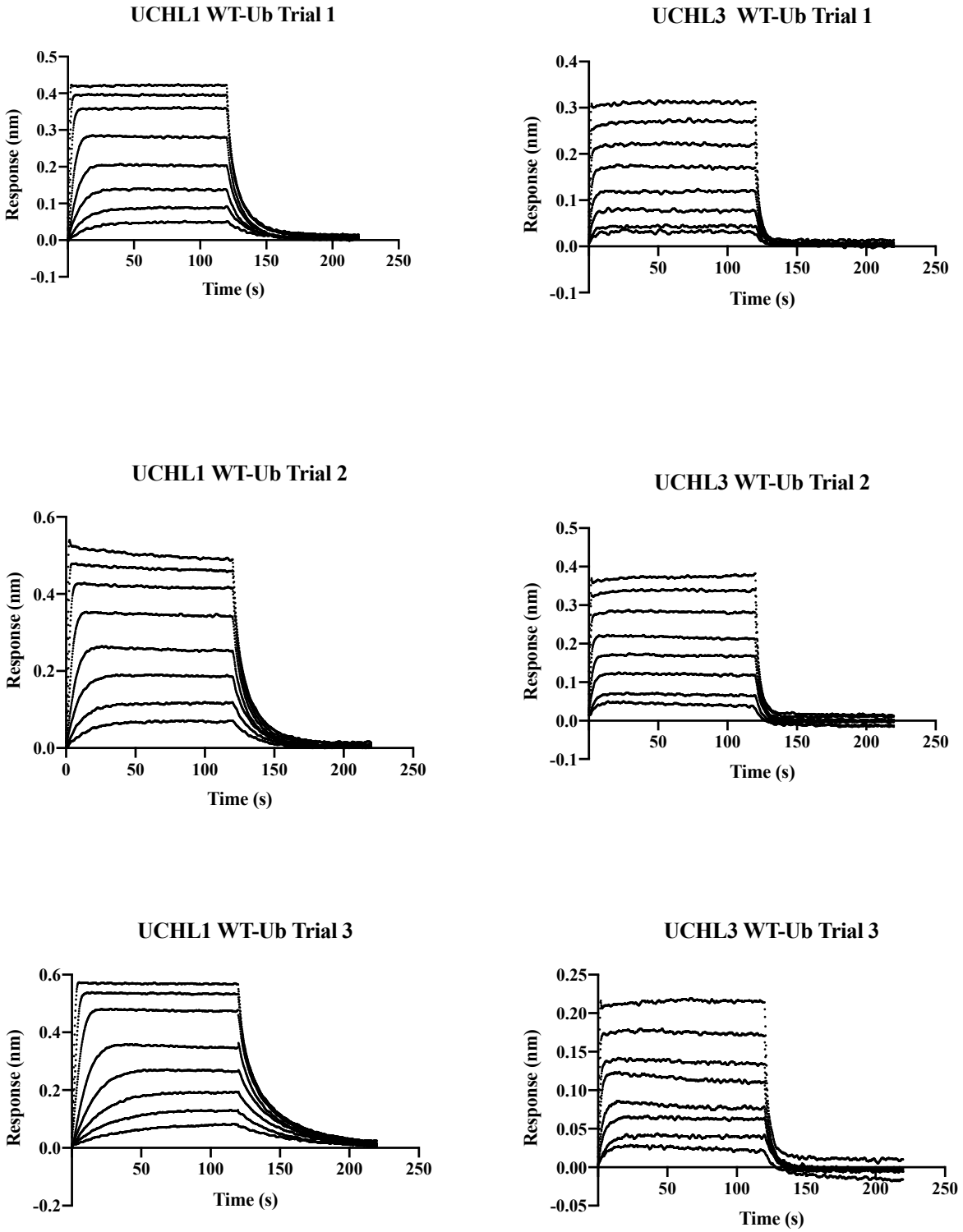

Figure A.2 Raw Biolayer Interferometry Association and Dissociation Curves for WT-Ub Binding to His-UCHL1 and His-UCHL3. WT Ubiquitin association lasted for 120 seconds and subsequently dissociated for 100 seconds. Data subtracted from baseline sensogram containing 1x PBS 0.05% v/v Tween 20 with 0.1% w/v BSA (buffer only) wells in loading, association, dissociation, and buffer containing wells.

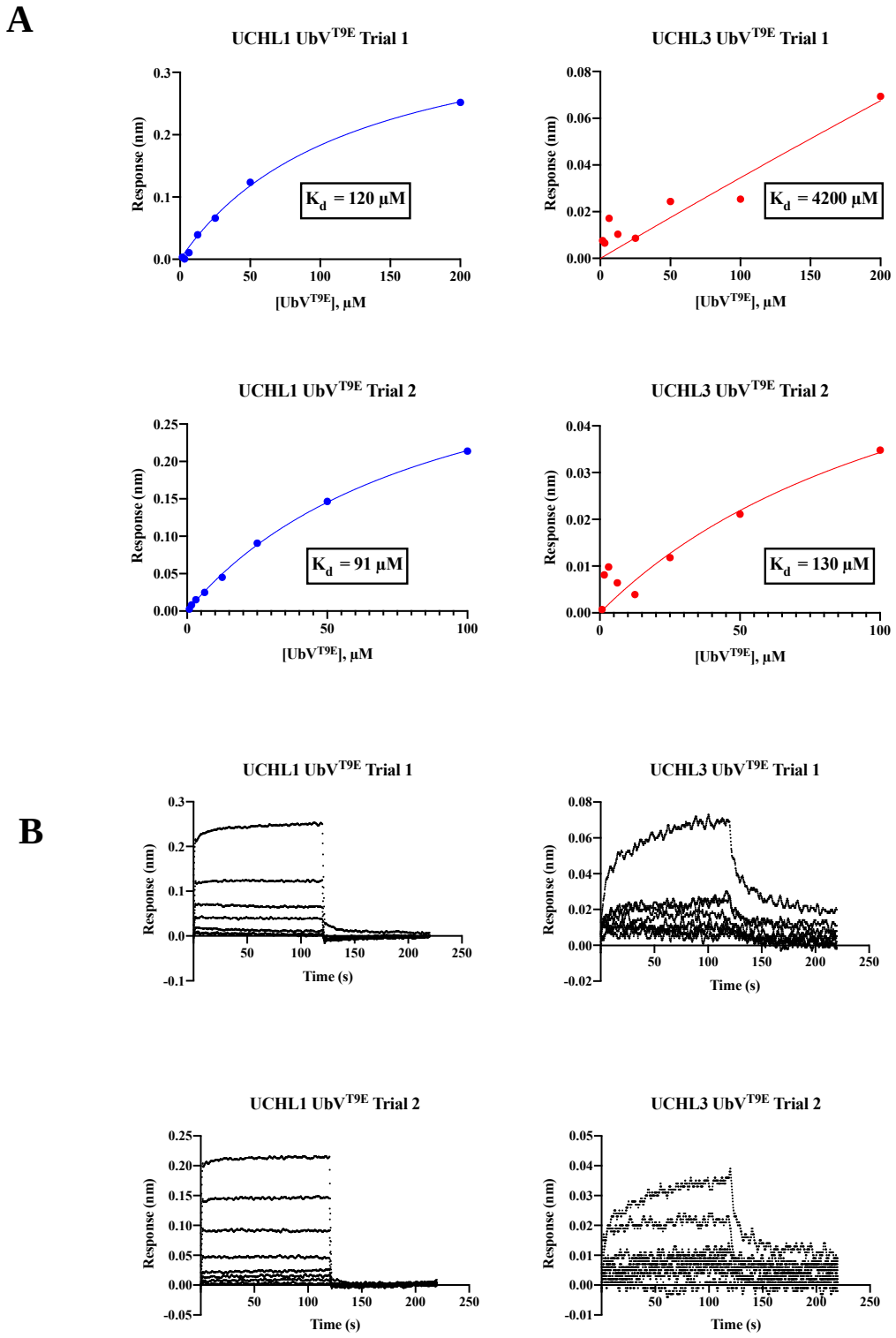

Figure A.3 A) Biolayer Interferometry Steady State Binding Curves for UbV^{T9E} Binding to His-UCHL1 and His-UCHL3. Individual points were averaged values from 110s-115s of the association step for each trial. K_ds determined by fitting to a 1:1 binding model in Prism 8 B) Raw biolayer interferometry association and dissociation curves for UbV^{T9E} binding to His-UCHL1 and His-UCHL3. UbV^{T9E} association lasted for 120 seconds and subsequently dissociated for 100 seconds. Data subtracted from baseline sensogram containing 1x PBS 0.05% v/v Tween 20 with 0.1% w/v BSA (buffer only) wells in loading, association, dissociation, and buffer containing wells.

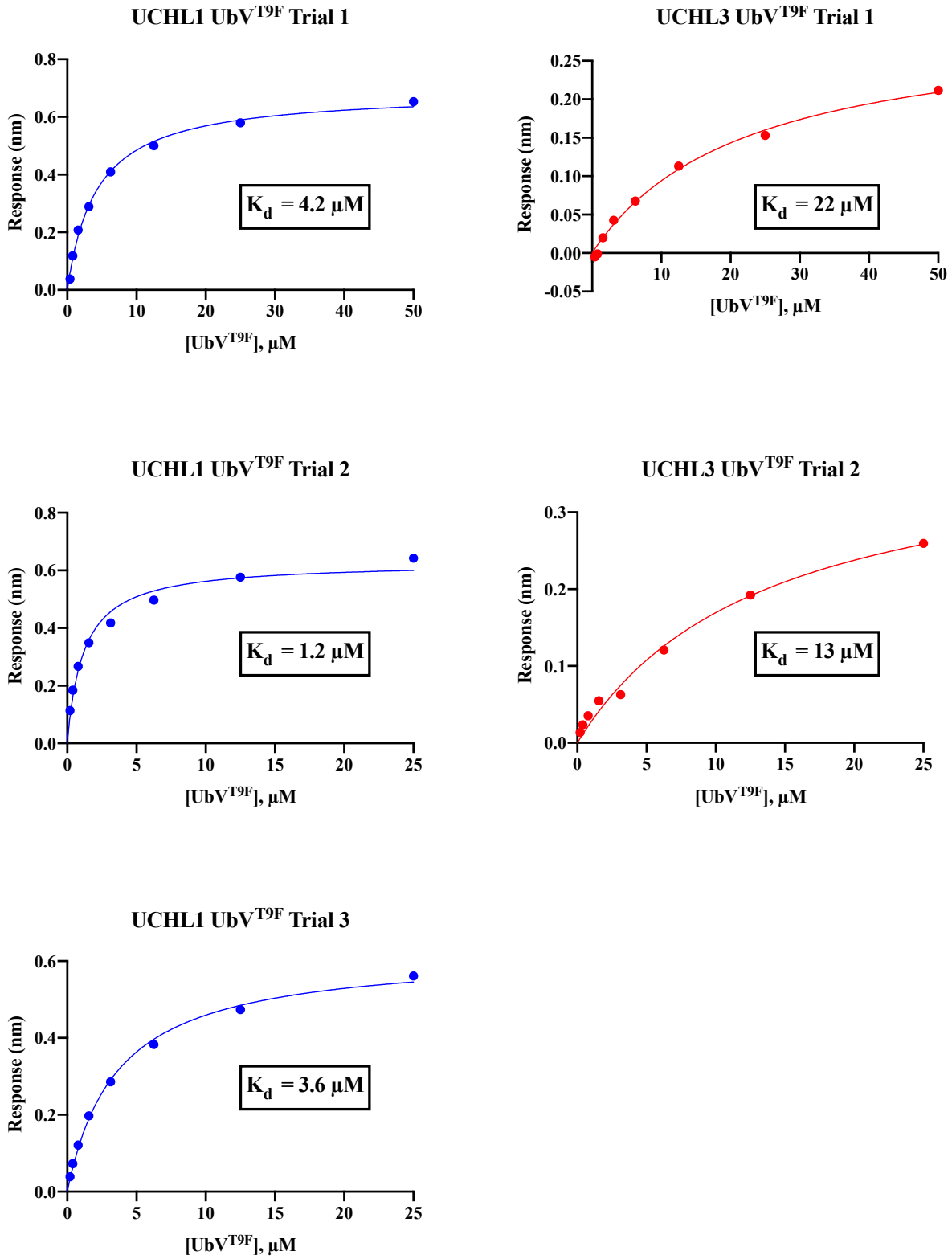

Figure A.4 Biolayer Interferometry Steady State Binding Curves for UbV^{T9F} Binding to His-UCHL1 and His-UCHL3. Individual points were averaged values from 110s-115s of the association step for each trial. K_ds determined by fitting to a 1:1 binding model in Prism 8.

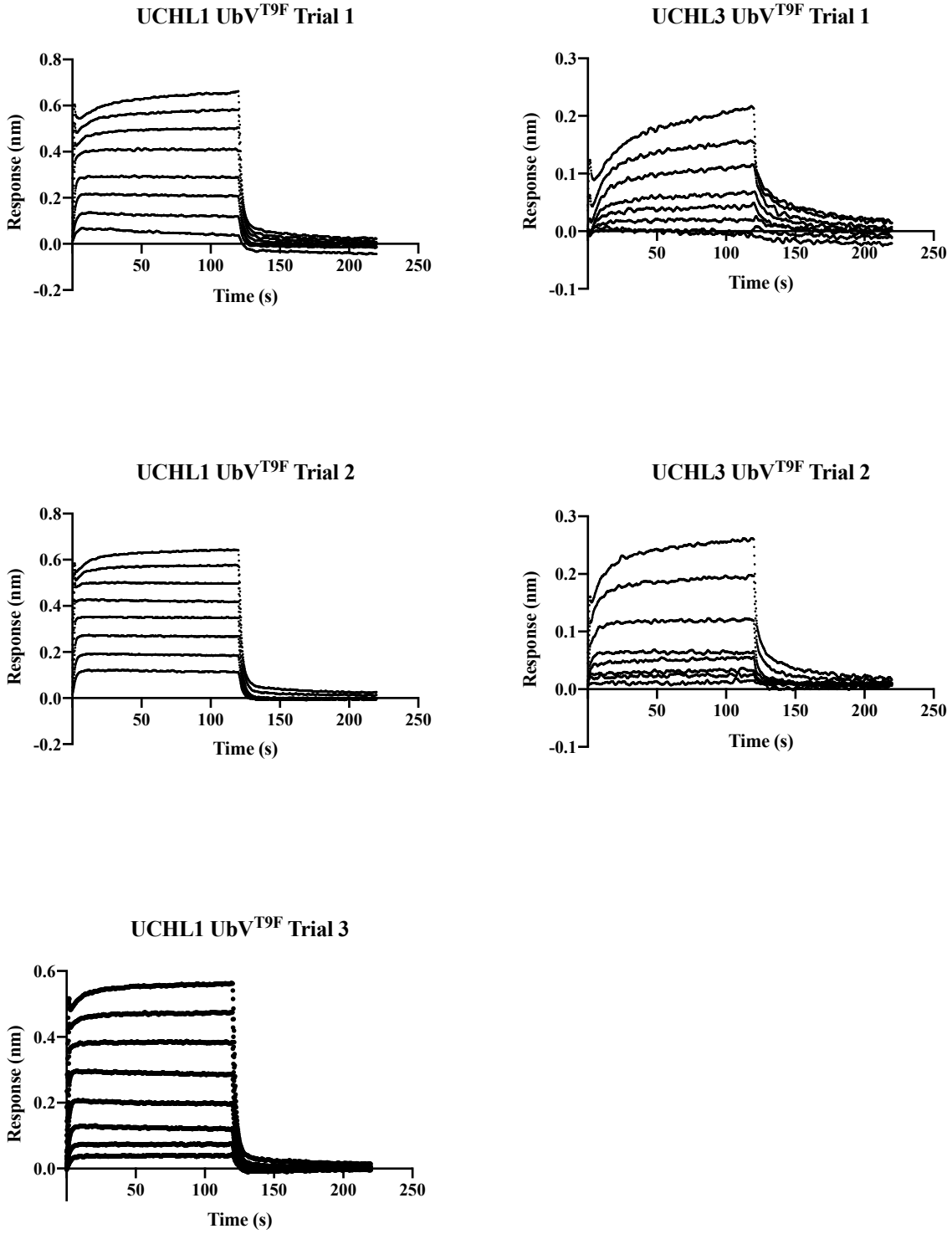

Figure A.5 Raw Biolayer Interferometry Association and Dissociation Curves for UbV^{T9F} Binding to His-UCHL1 and His-UCHL3. UbV^{T9F} association lasted for 120 seconds and subsequently dissociated for 100 seconds. Data subtracted from baseline sensorgram containing 1x PBS 0.05% v/v Tween 20 with 0.1% w/v BSA (buffer only) wells in loading, association, dissociation, and buffer containing wells.

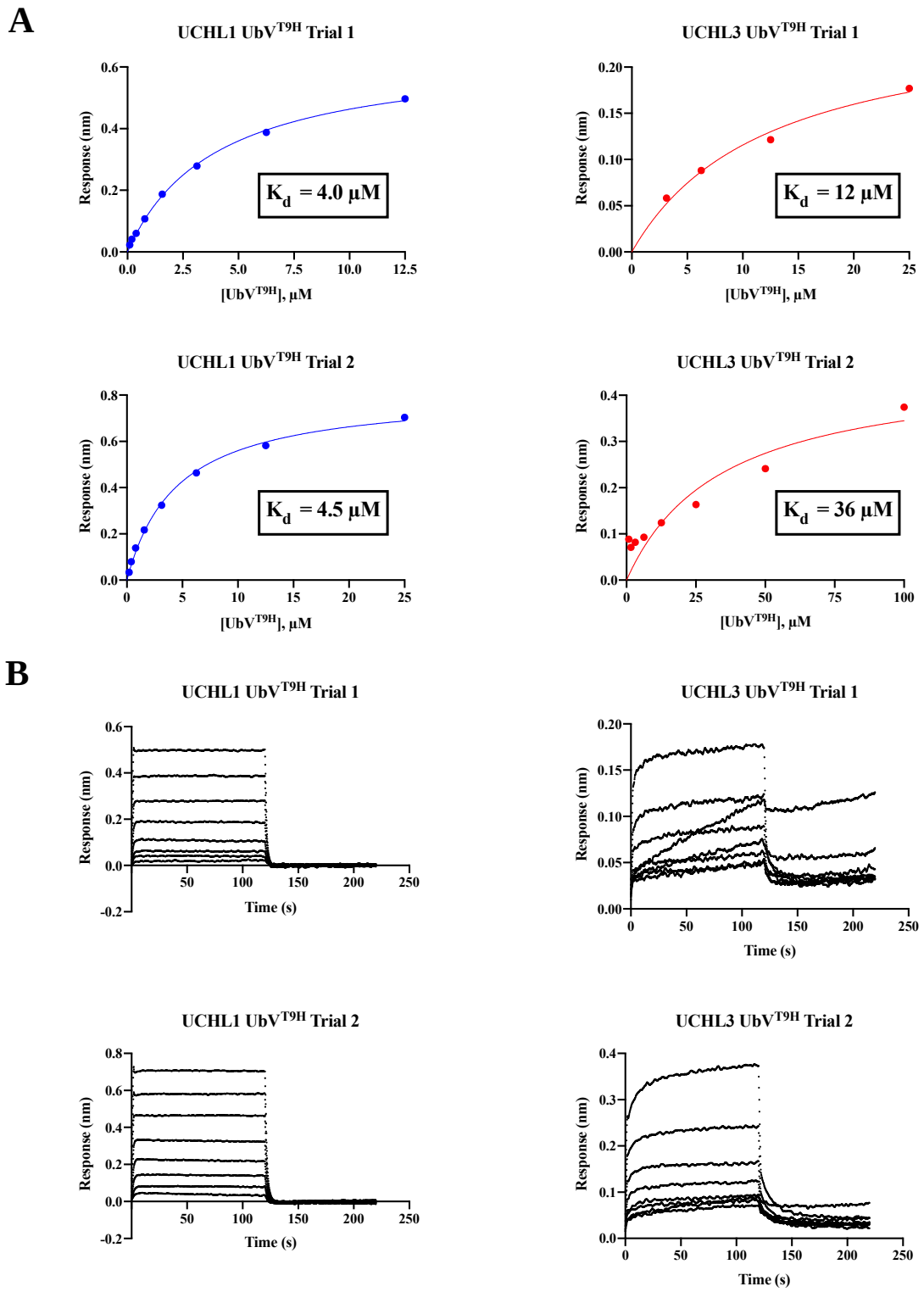

Figure A.6 A) Biolayer Interferometry Steady State Binding Curves for UbV^{T9H} Binding to His-UCHL1 and His-UCHL3. Individual points were averaged values from 110s-115s of the association step for each trial. K_ds determined by fitting to a 1:1 binding model in Prism 8 B) Raw biolayer interferometry association and dissociation curves for UbV^{T9H} binding to His-UCHL1 and His-UCHL3. UbV^{T9H} association lasted for 120 seconds and subsequently dissociated for 100 seconds. Data subtracted from baseline sensorgram containing 1x PBS 0.05% v/v Tween 20 with 0.1% w/v BSA (buffer only) wells in loading, association, dissociation, and buffer containing wells.

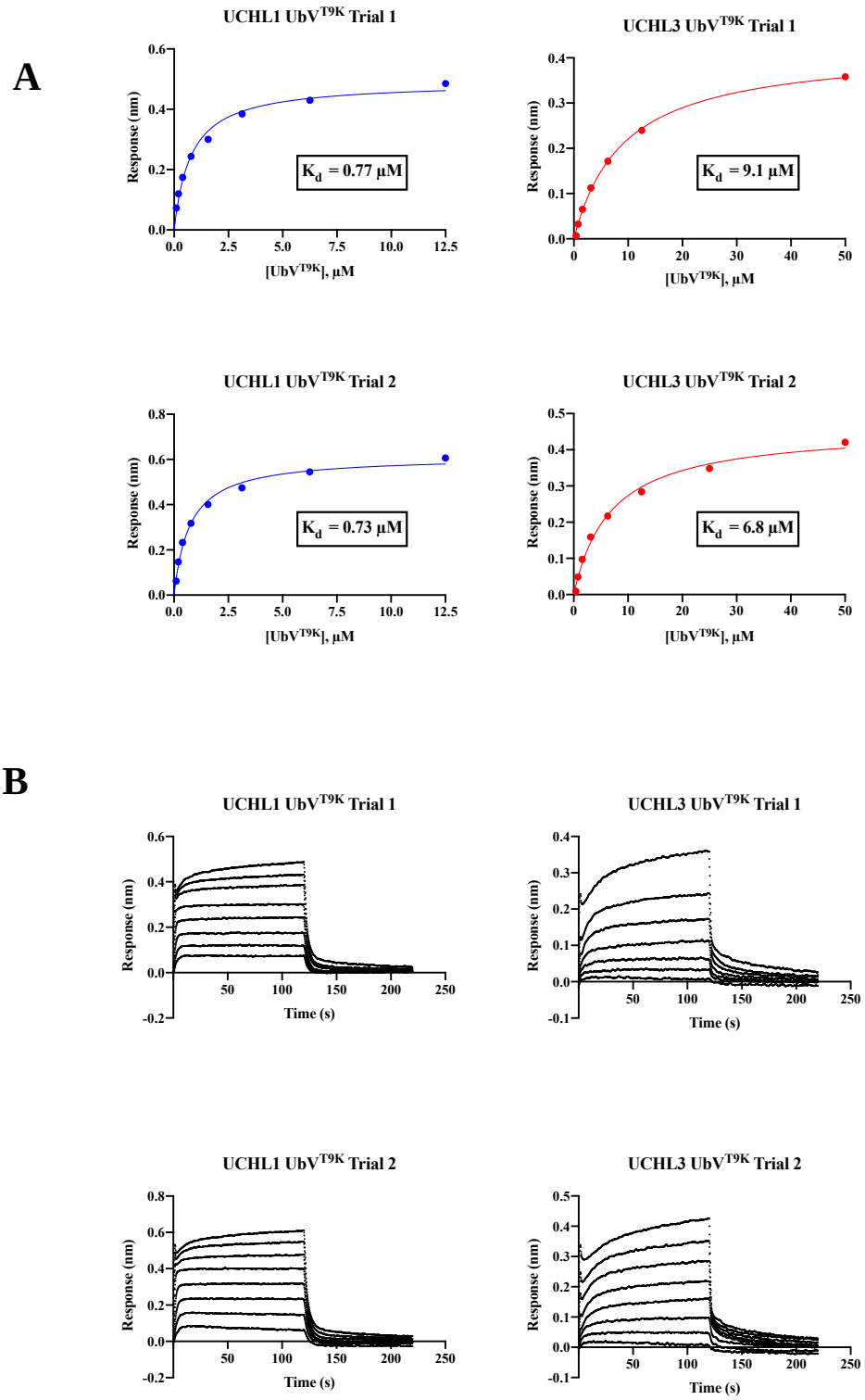

Figure A.7 A) Biolayer Interferometry Steady State Binding Curves for UbV^{T9K} Binding to His-UCHL1 and His-UCHL3. Individual points were averaged values from 110s-115s of the association step for each trial. K_ds determined by fitting to a 1:1 binding model in Prism 8 B) Raw biolayer interferometry association and dissociation curves for UbV^{T9K} binding to His-UCHL1 and His-UCHL3. UbV^{T9K} association lasted for 120 seconds and subsequently dissociated for 100 seconds. Data subtracted from baseline sensorgram containing 1x PBS 0.05% v/v Tween 20 with 0.1% w/v BSA (buffer only) wells in loading, association, dissociation, and buffer containing wells.

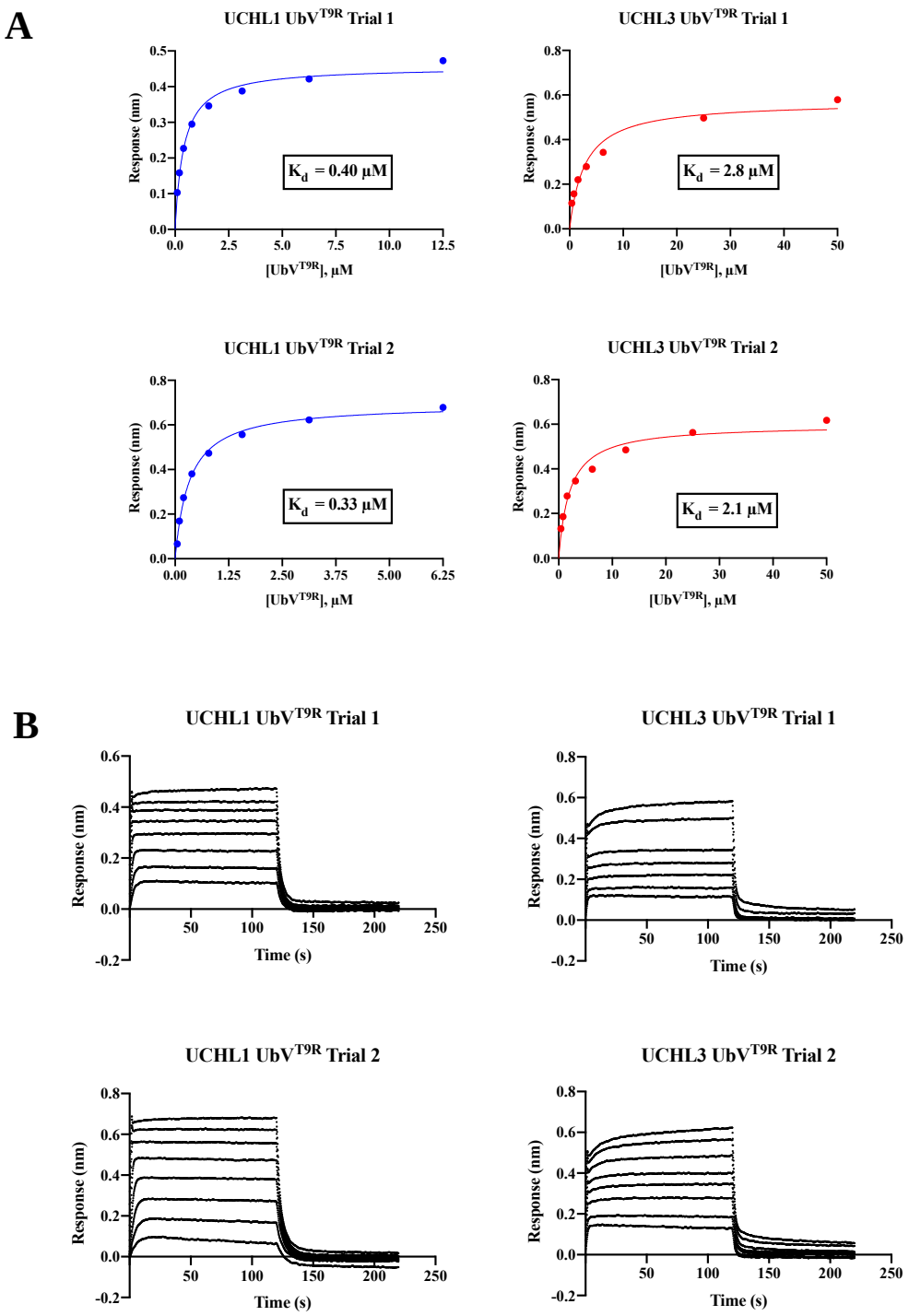

Figure A.8 A) Biolayer Interferometry Steady State Binding Curves for UbV^{T9R} Binding to His-UCHL1 and His-UCHL3. Individual points were averaged values from 110s-115s of the association step for each trial. K_ds determined by fitting to a 1:1 binding model in Prism 8 B) Raw biolayer interferometry association and dissociation curves for UbV^{T9R} binding to His-UCHL1 and His-UCHL3. UbV^{T9R} association lasted for 120 seconds and subsequently dissociated for 100 seconds. Data subtracted from baseline sensorgram containing 1x PBS 0.05% v/v Tween 20 with 0.1% w/v BSA (buffer only) wells in loading, association, dissociation, and buffer containing wells.

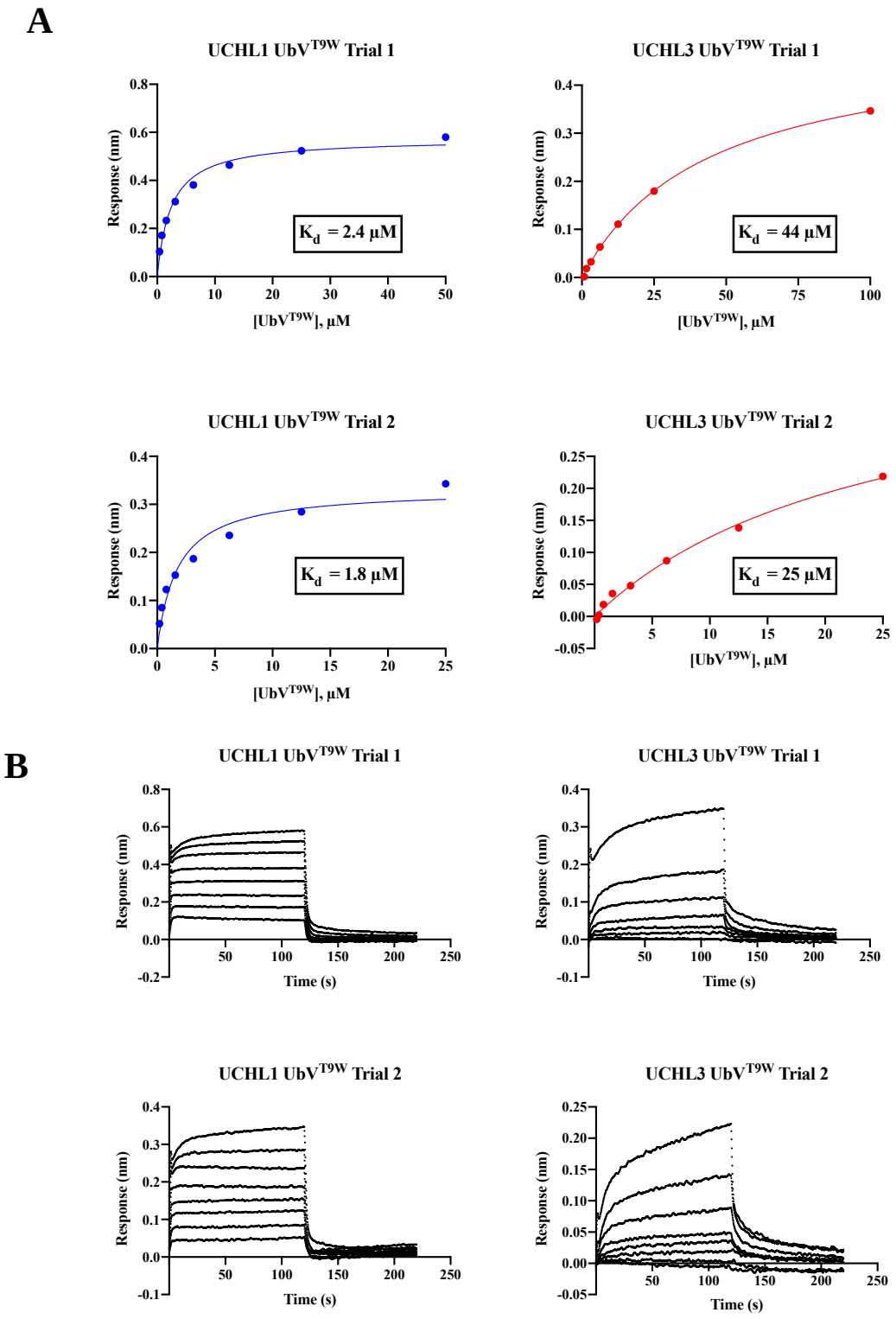

Figure A.9 A) Biolayer Interferometry Steady State Binding Curves for UbV^{T9W} Binding to His-UCHL1 and His-UCHL3. Individual points were averaged values from 110s-115s of the association step for each trial. K_ds determined by fitting to a 1:1 binding model in Prism 8 B) Raw biolayer interferometry association and dissociation curves for UbV^{T9W} binding to His-UCHL1 and His-UCHL3. UbV^{T9W} association lasted for 120 seconds and subsequently dissociated for 100 seconds. Data subtracted from baseline sensorgram containing 1x PBS 0.05% v/v Tween 20 with 0.1% w/v BSA (buffer only) wells in loading, association, dissociation, and buffer containing wells.

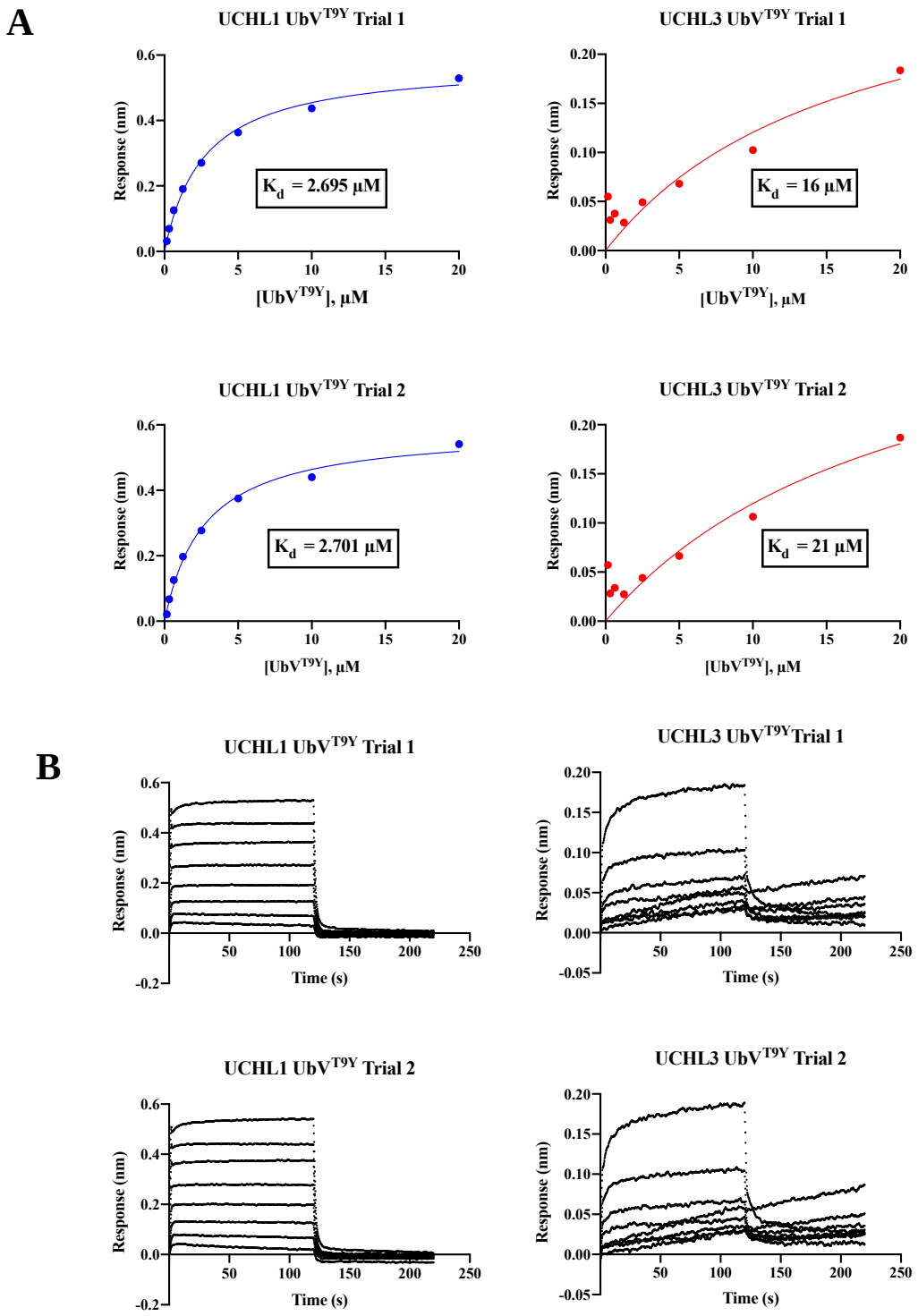

Figure A.10 A) Biolayer Interferometry Steady State Binding Curves for UbV^{T9Y} Binding to His-UCHL1 and His-UCHL3. Individual points were averaged values from 110s-115s of the association step for each trial. K_ds determined by fitting to a 1:1 binding model in Prism 8 B) Raw biolayer interferometry association and dissociation curves for UbV^{T9Y} binding to His-UCHL1 and His-UCHL3. UbV^{T9Y} association lasted for 120 seconds and subsequently dissociated for 100 seconds. Data subtracted from baseline sensorgram containing 1x PBS 0.05% v/v Tween 20 with 0.1% w/v BSA (buffer only) wells in loading, association, dissociation, and buffer containing wells.

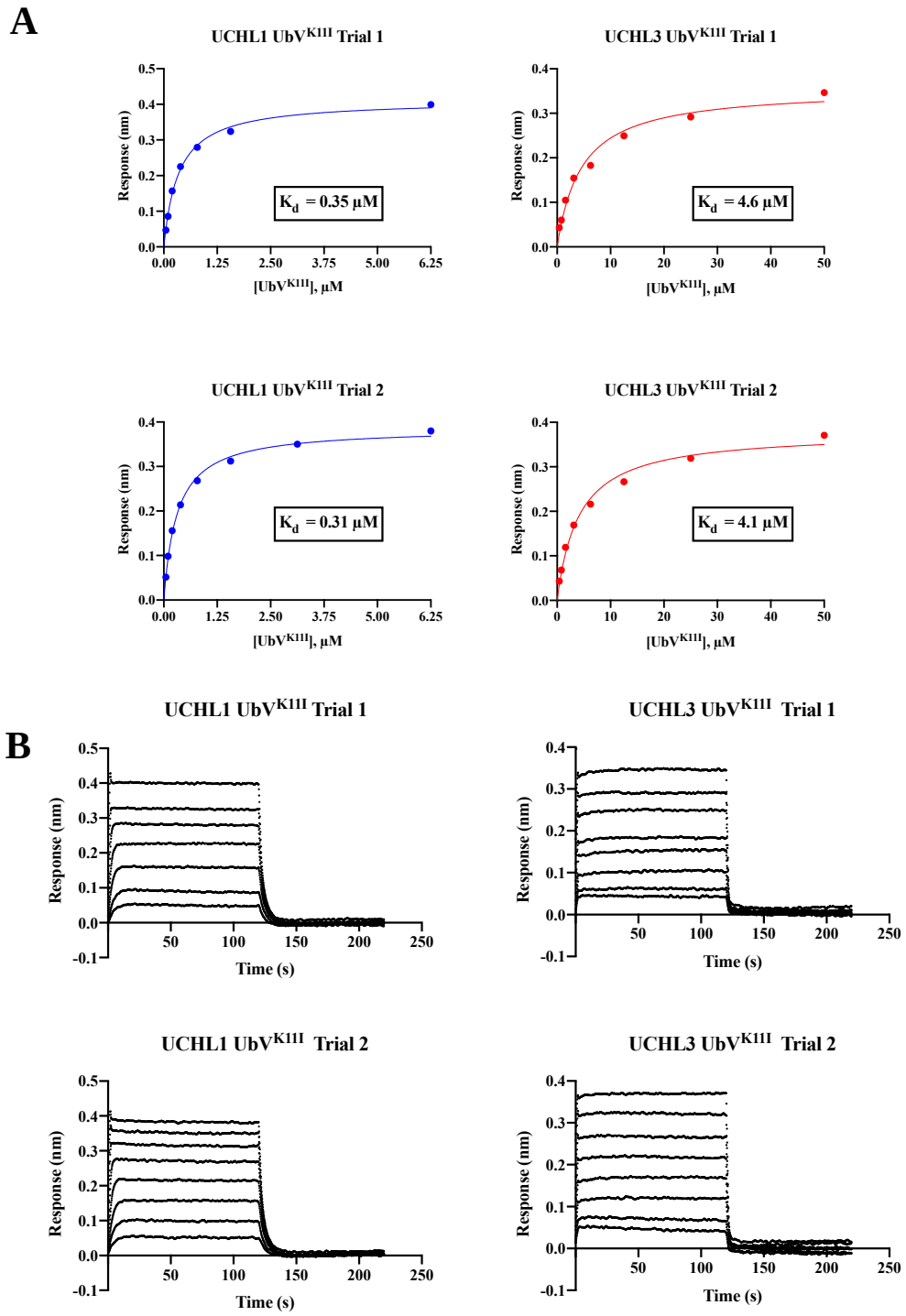

Figure A.11 A) Biolayer Interferometry Steady State Binding Curves for UbV^{K11I} Binding to His-UCHL1 and His-UCHL3. Individual points were averaged values from 110s-115s of the association step for each trial. K_ds determined by fitting to a 1:1 binding model in Prism 8 B) Raw biolayer interferometry association and dissociation curves for UbV^{K11I} binding to His-UCHL1 and His-UCHL3. UbV^{K11I} association lasted for 120 seconds and subsequently dissociated for 100 seconds. Data subtracted from baseline sensorgram containing 1x PBS 0.05% v/v Tween 20 with 0.1% w/v BSA (buffer only) wells in loading, association, dissociation, and buffer containing wells.

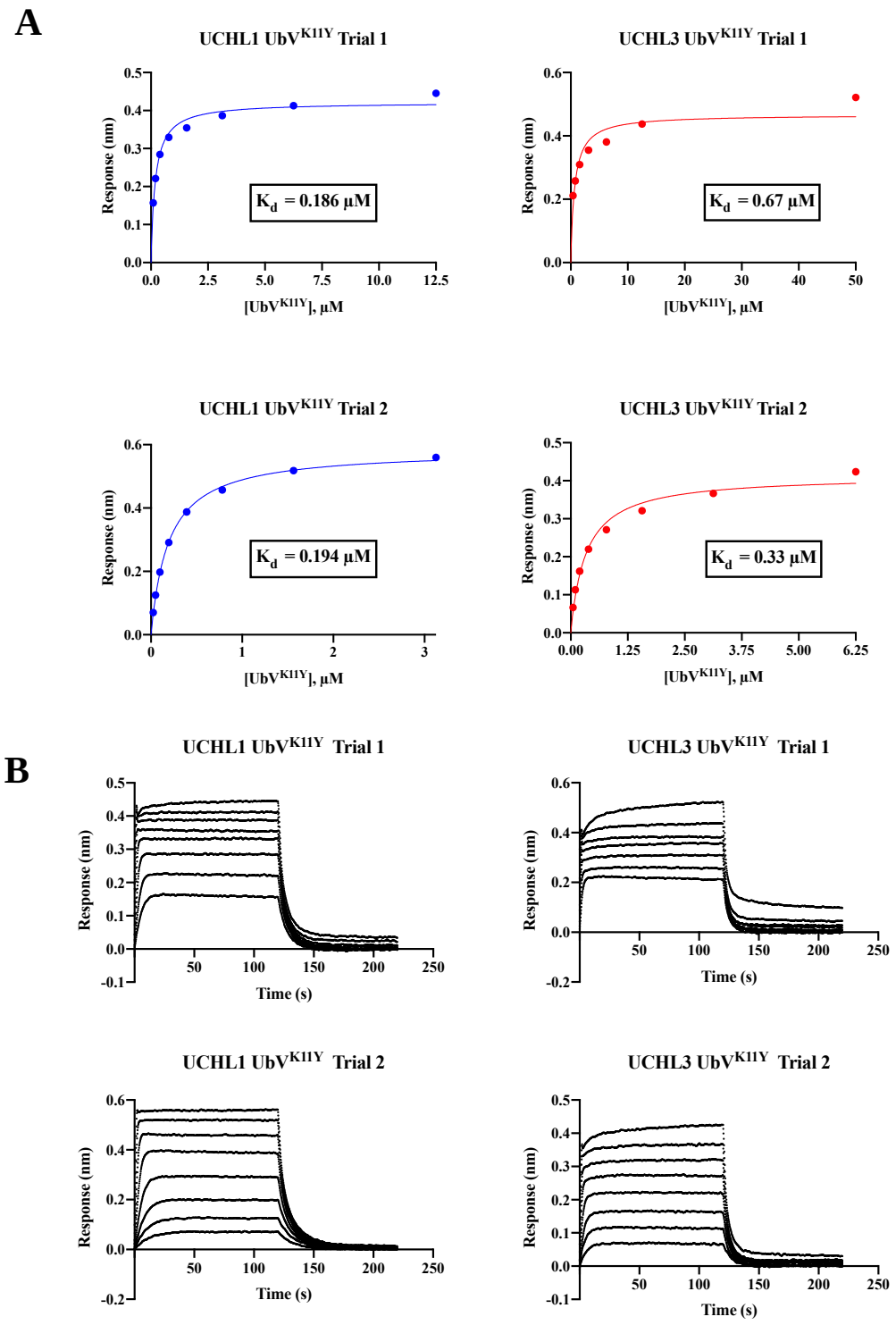

Figure A.12 A) Biolayer Interferometry Steady State Binding Curves for UbV^{K11Y} Binding to His-UCHL1 and His-UCHL3. Individual points were averaged values from 110s-115s of the association step for each trial. K_ds determined by fitting to a 1:1 binding model in Prism 8 B) Raw biolayer interferometry association and dissociation curves for UbV^{K11Y} binding to His-UCHL1 and His-UCHL3. UbV^{K11Y} association lasted for 120 seconds and subsequently dissociated for 100 seconds. Data subtracted from baseline sensorgram containing 1x PBS 0.05% v/v Tween 20 with 0.1% w/v BSA (buffer only) wells in loading, association, dissociation, and buffer containing wells.

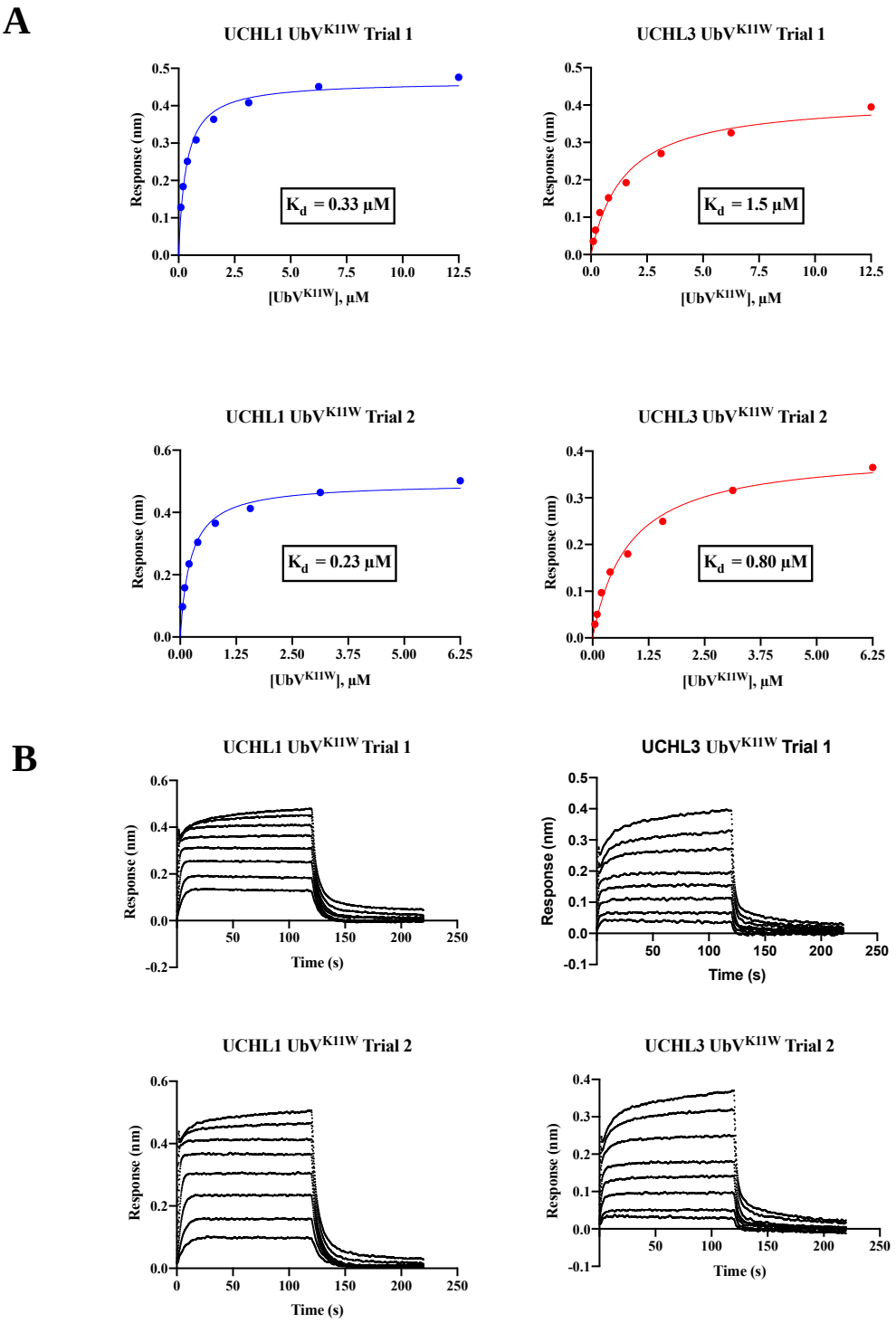

Figure A.13 A) Biolayer Interferometry Steady State Binding Curves for UbV^{K11W} Binding to His-UCHL1 and His-UCHL3. Individual points were averaged values from 110s-115s of the association step for each trial. K_ds determined by fitting to a 1:1 binding model in Prism 8 B) Raw biolayer interferometry association and dissociation curves for UbV^{K11W} binding to His-UCHL1 and His-UCHL3. UbV^{K11W} association lasted for 120 seconds and subsequently dissociated for 100 seconds. Data subtracted from baseline sensorgram containing 1x PBS 0.05% v/v Tween 20 with 0.1% w/v BSA (buffer only) wells in loading, association, dissociation, and buffer containing wells.

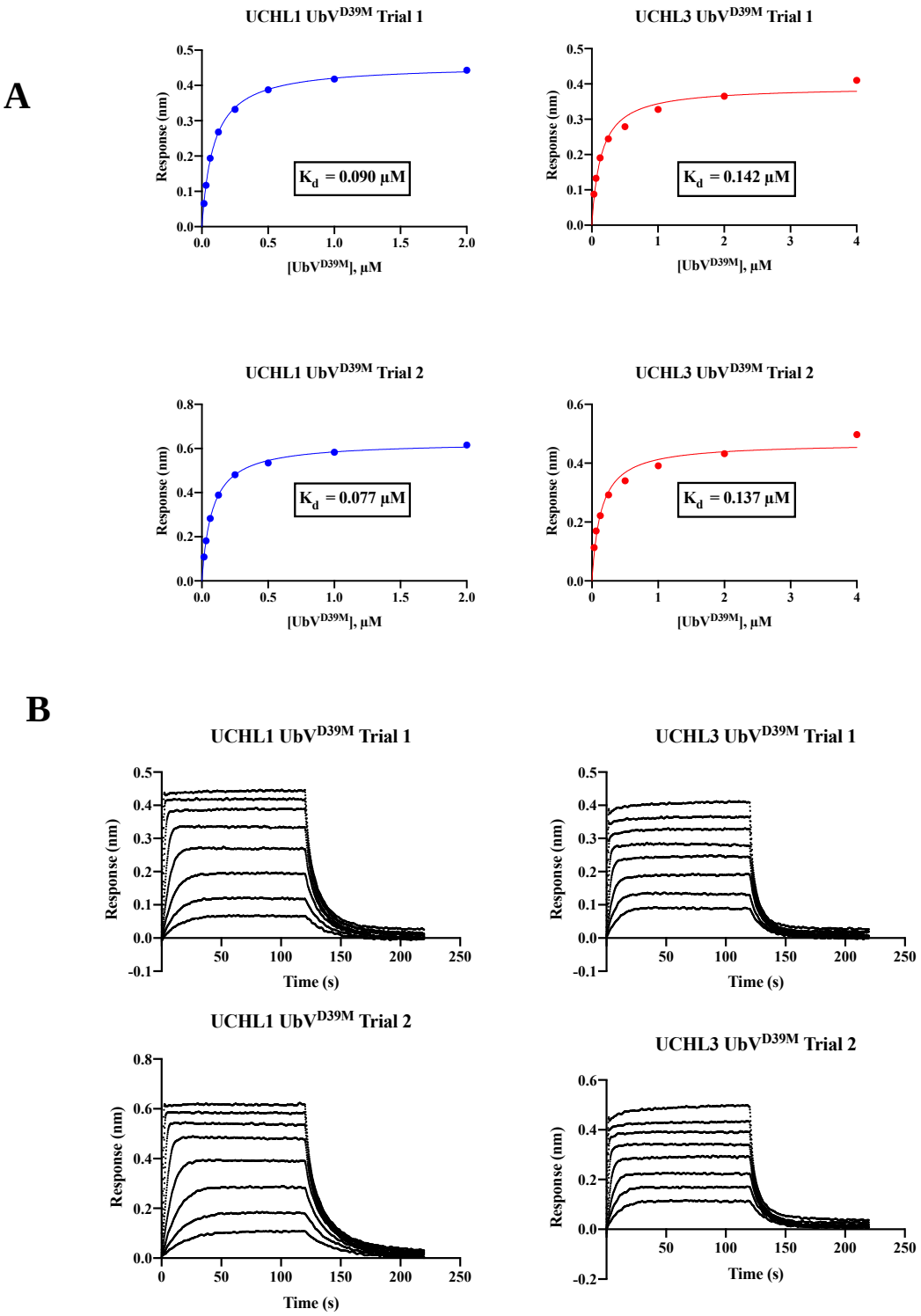

Figure A.14 A) Biolayer Interferometry Steady State Binding Curves for UbV^{D39M} Binding to His-UCHL1 and His-UCHL3. Individual points were averaged values from 110s-115s of the association step for each trial. K_ds determined by fitting to a 1:1 binding model in Prism 8 B) Raw biolayer interferometry association and dissociation curves for UbV^{D39M} binding to His-UCHL1 and His-UCHL3. UbV^{D39M} association lasted for 120 seconds and subsequently dissociated for 100 seconds. Data subtracted from baseline sensorgram containing 1x PBS 0.05% v/v Tween 20 with 0.1% w/v BSA (buffer only) wells in loading, association, dissociation, and buffer containing wells.

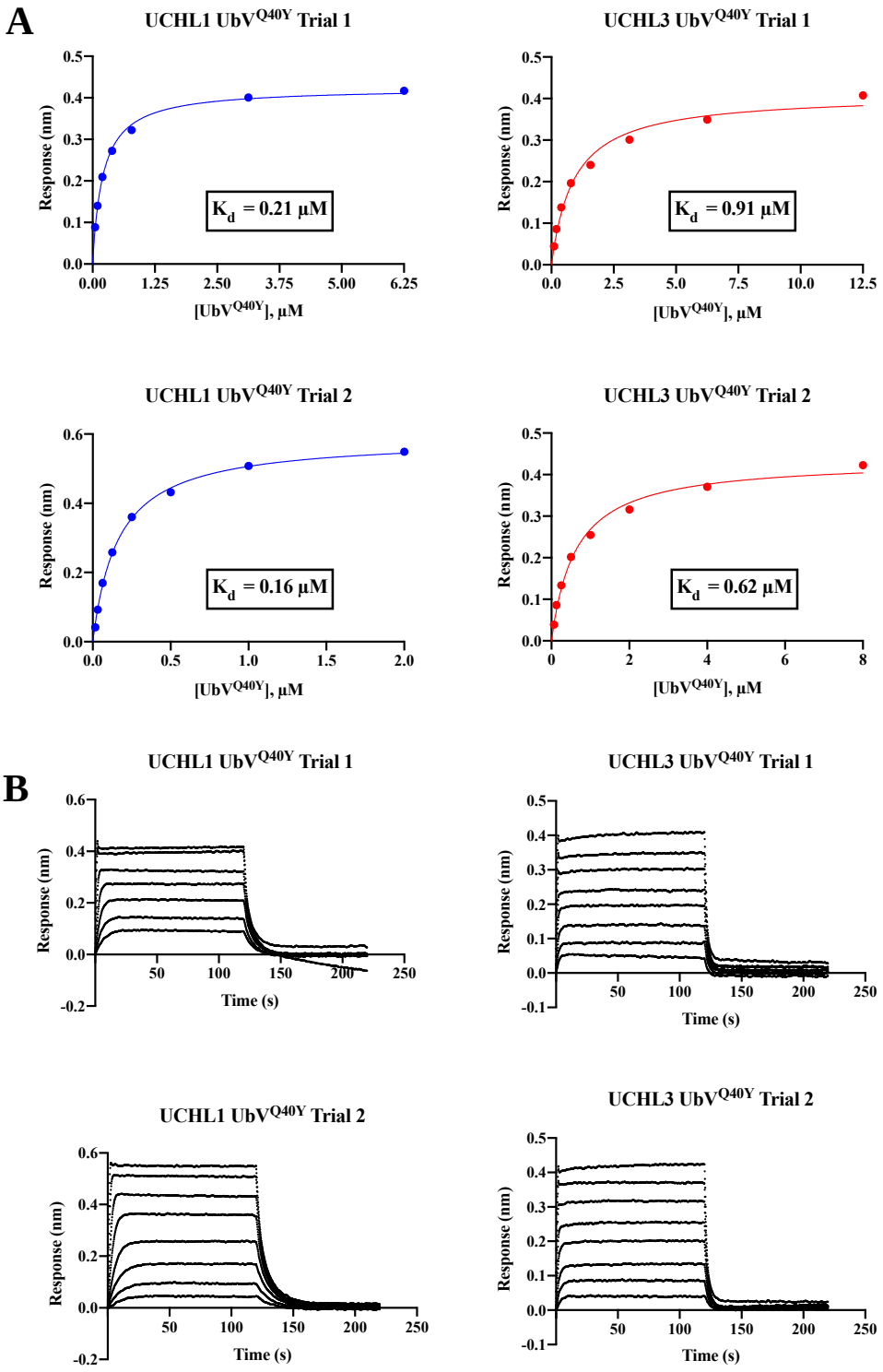

Figure A.15 A) Biolayer Interferometry Steady State Binding Curves for UbV^{Q40Y} Binding to His-UCHL1 and His-UCHL3. Individual points were averaged values from 110s-115s of the association step for each trial. K_ds determined by fitting to a 1:1 binding model in Prism 8 B) Raw biolayer interferometry association and dissociation curves for UbV^{Q40Y} binding to His-UCHL1 and His-UCHL3. UbV^{Q40Y} association lasted for 120 seconds and subsequently dissociated for 100 seconds. Data subtracted from baseline sensorgram containing 1x PBS 0.05% v/v Tween 20 with 0.1% w/v BSA (buffer only) wells in loading, association, dissociation, and buffer containing wells.

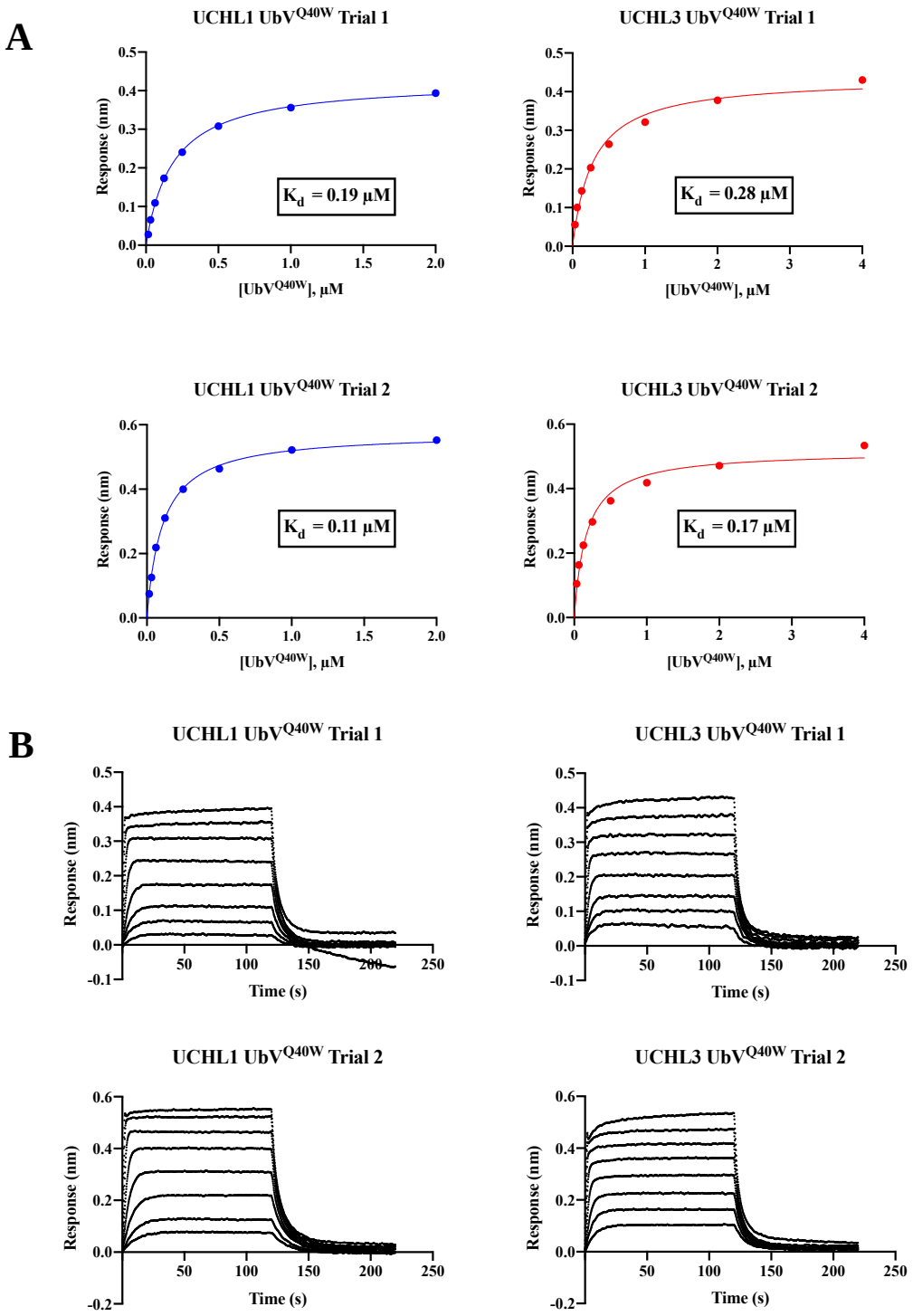

Figure A.16 A) Biolayer Interferometry Steady State Binding Curves for UbV^{Q40W} Binding to His-UCHL1 and His-UCHL3. Individual points were averaged values from 110s-115s of the association step for each trial. K_ds determined by fitting to a 1:1 binding model in Prism 8 B) Raw biolayer interferometry association and dissociation curves for UbV^{Q40W} binding to His-UCHL1 and His-UCHL3. UbV^{Q40W} association lasted for 120 seconds and subsequently dissociated for 100 seconds. Data subtracted from baseline sensorgram containing 1x PBS 0.05% v/v Tween 20 with 0.1% w/v BSA (buffer only) wells in loading, association, dissociation, and buffer containing wells.

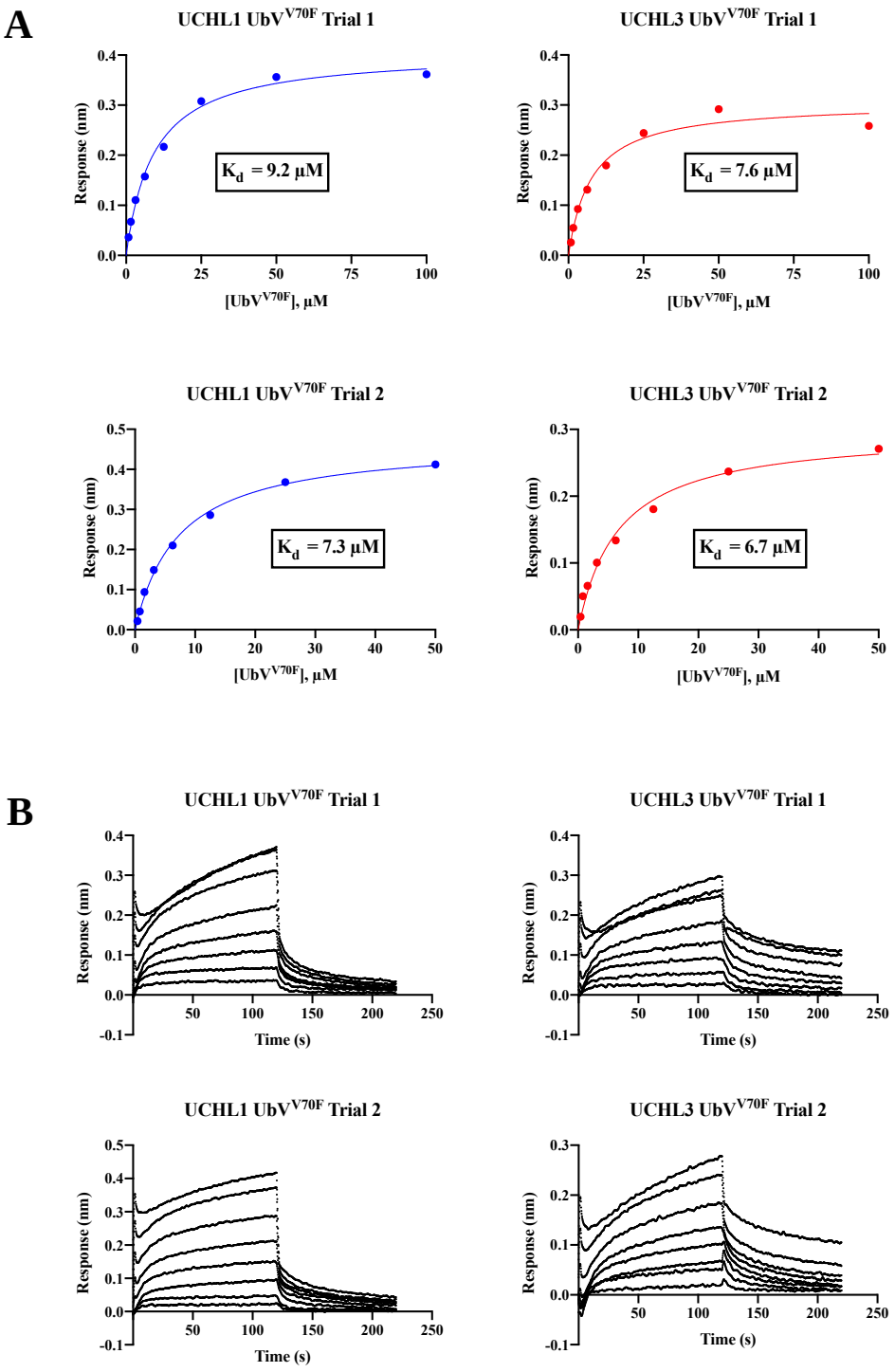

Figure A.17 A) Biolayer Interferometry Steady State Binding Curves for UbV^{V70F} Binding to His-UCHL1 and His-UCHL3. Individual points were averaged values from 110s-115s of the association step for each trial. K_ds determined by fitting to a 1:1 binding model in Prism 8 B) Raw biolayer interferometry association and dissociation curves for UbV^{V70F} binding to His-UCHL1 and His-UCHL3. UbV^{V70F} association lasted for 120 seconds and subsequently dissociated for 100 seconds. Data subtracted from baseline sensorgram containing 1x PBS 0.05% v/v Tween 20 with 0.1% w/v BSA (buffer only) wells in loading, association, dissociation, and buffer containing wells.

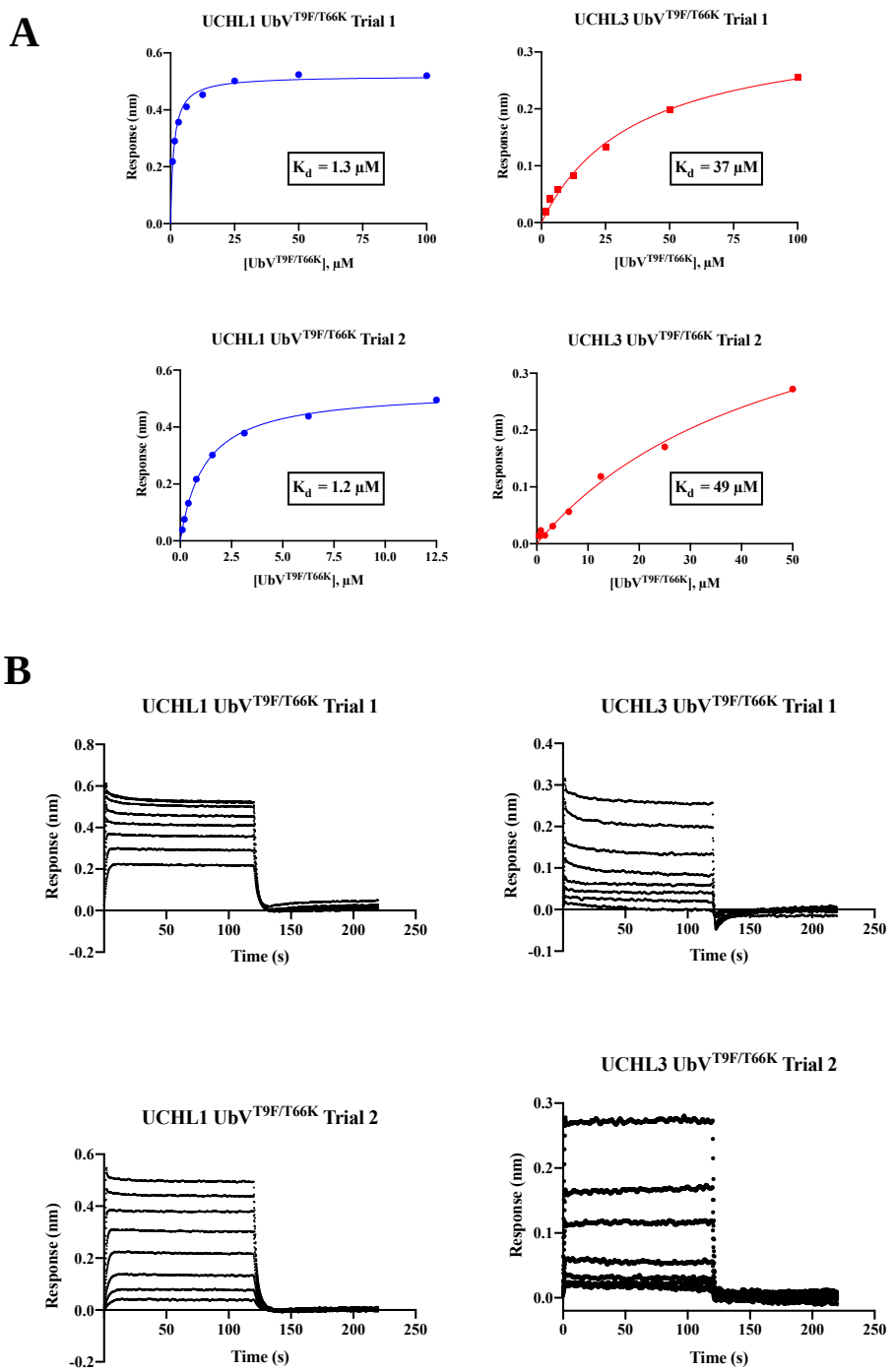

Figure A.18 A) Biolayer Interferometry Steady State Binding Curves for $UbV^{T9F/T66K}$ Binding to His-UCHL1 and His-UCHL3. Individual points were averaged values from 110s-115s of the association step for each trial. K_ds determined by fitting to a 1:1 binding model in Prism 8 B) Raw biolayer interferometry association and dissociation curves for $UbV^{T9F/T66K}$ binding to His-UCHL1 and His-UCHL3. $UbV^{T9F/T66K}$ association lasted for 120 seconds and subsequently dissociated for 100 seconds. Data subtracted from baseline sensorgram containing 1x PBS 0.05% v/v Tween 20 with 0.1% w/v BSA (buffer only) wells in loading, association, dissociation, and buffer containing wells.

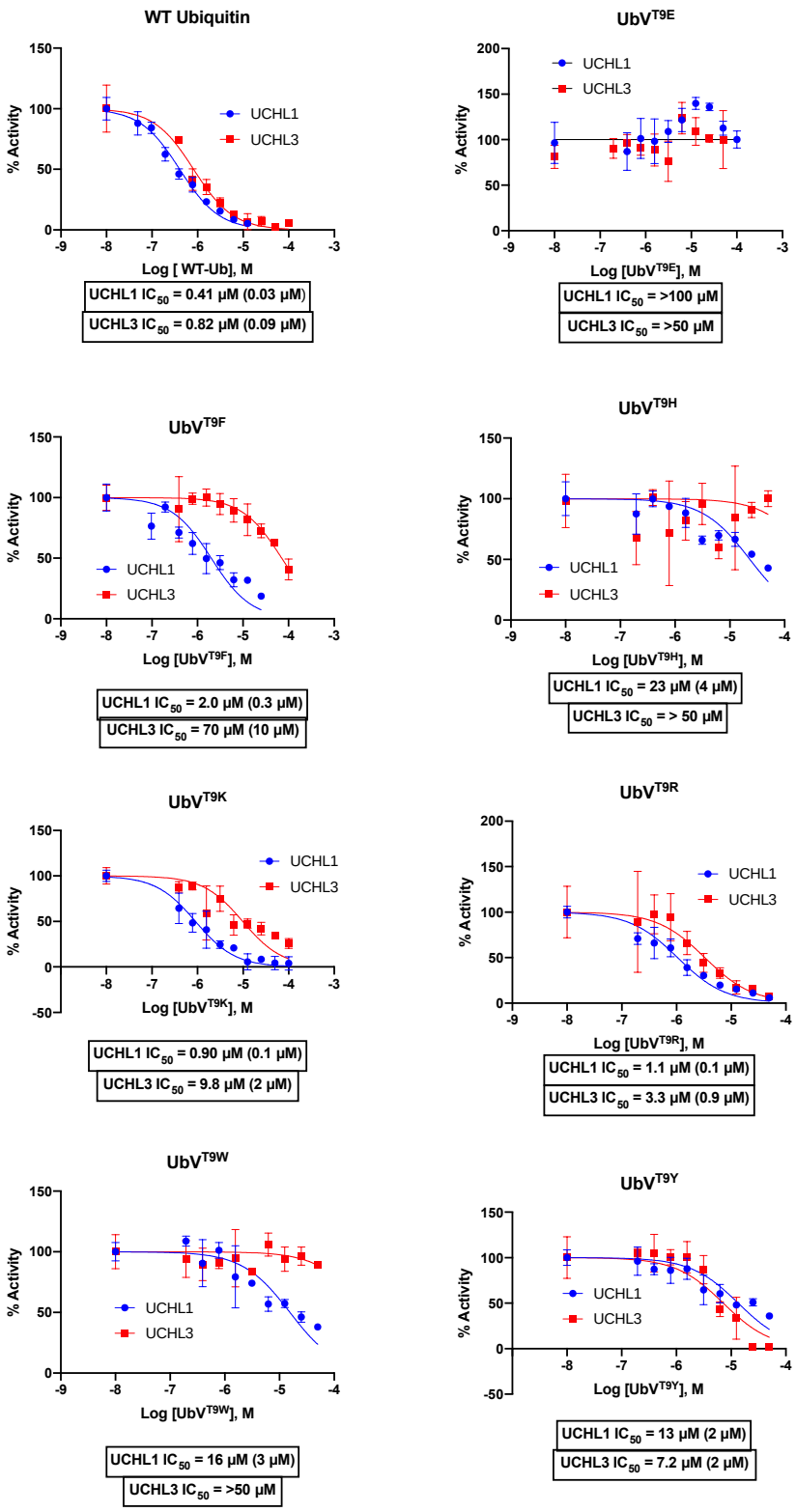

Figure A.19 IC_{50} for WT-Ub, UbV^{T9E}, UbV^{T9F}, UbV^{T9H}, UbV^{T9K}, UbV^{T9R}, UbV^{T9W}, and UbV^{T9Y} with His-UCHL1 (Blue) and His-UCHL3 (Red). 100% activity is average activity of UCH enzymes in Ub Rho assay buffer only (no UbV).

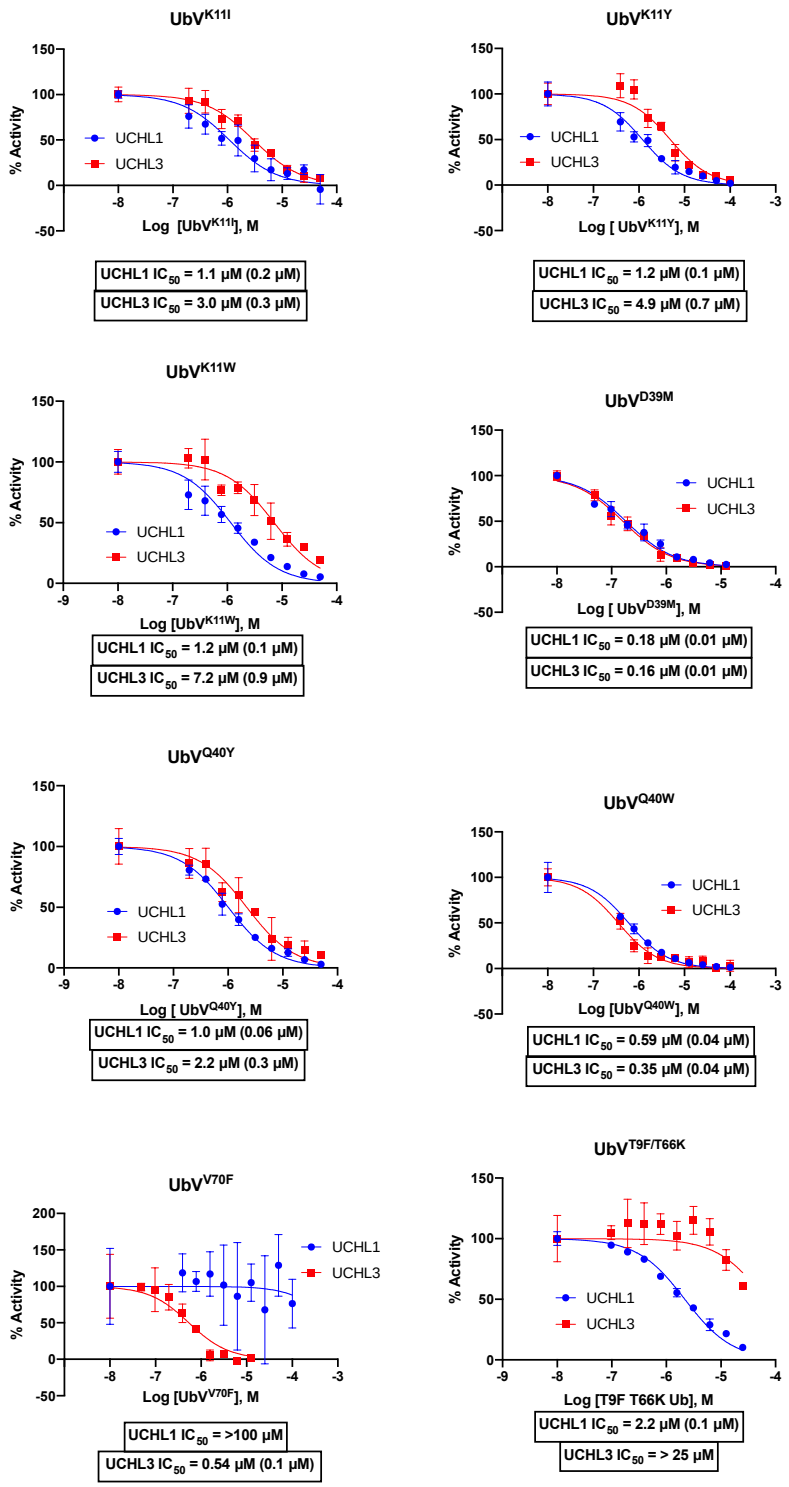

Figure A.20 IC_{50} for UbV^{K11I}, UbV^{K11Y}, UbV^{K11W}, UbV^{D39M}, UbV^{Q40Y}, UbV^{Q40W}, UbV^{V70F}, and $UbV^{T9F/T66K}$ with His-UCHL1 (Blue) and His-UCHL3 (Red). 100% activity is average activity of UCH enzymes in Ub Rho assay buffer only (no UbV).

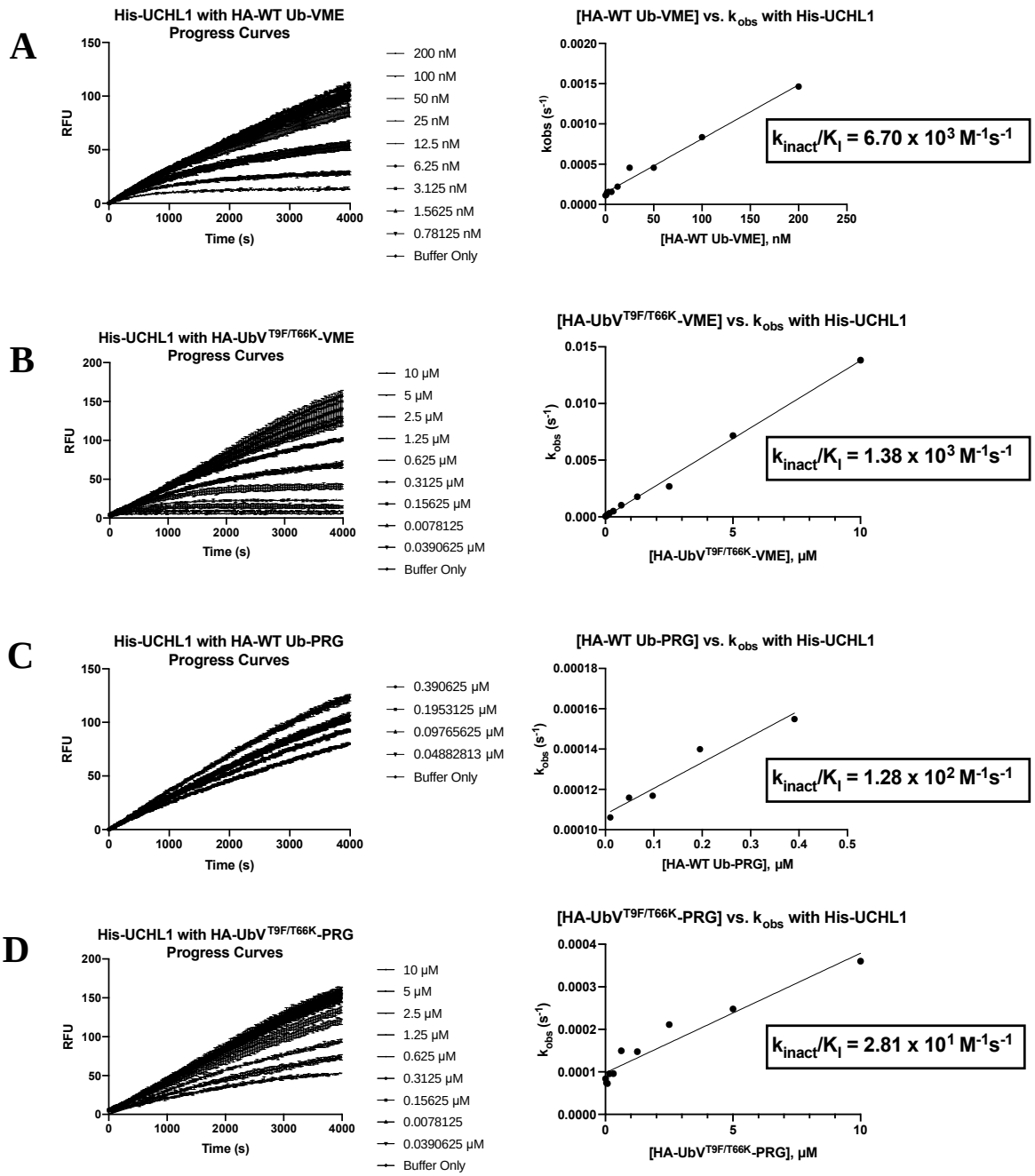

Figure A.21 Progress Curves and k_{inact}/K_I Data for His-UCHL1 with A) HA-WT Ub-VME, B) HA-UbV$^{T9F/T66K}$-VME, C) HA-WT Ub-PRG, and D) HA-UbV$^{T9F/T66K}$-PRG

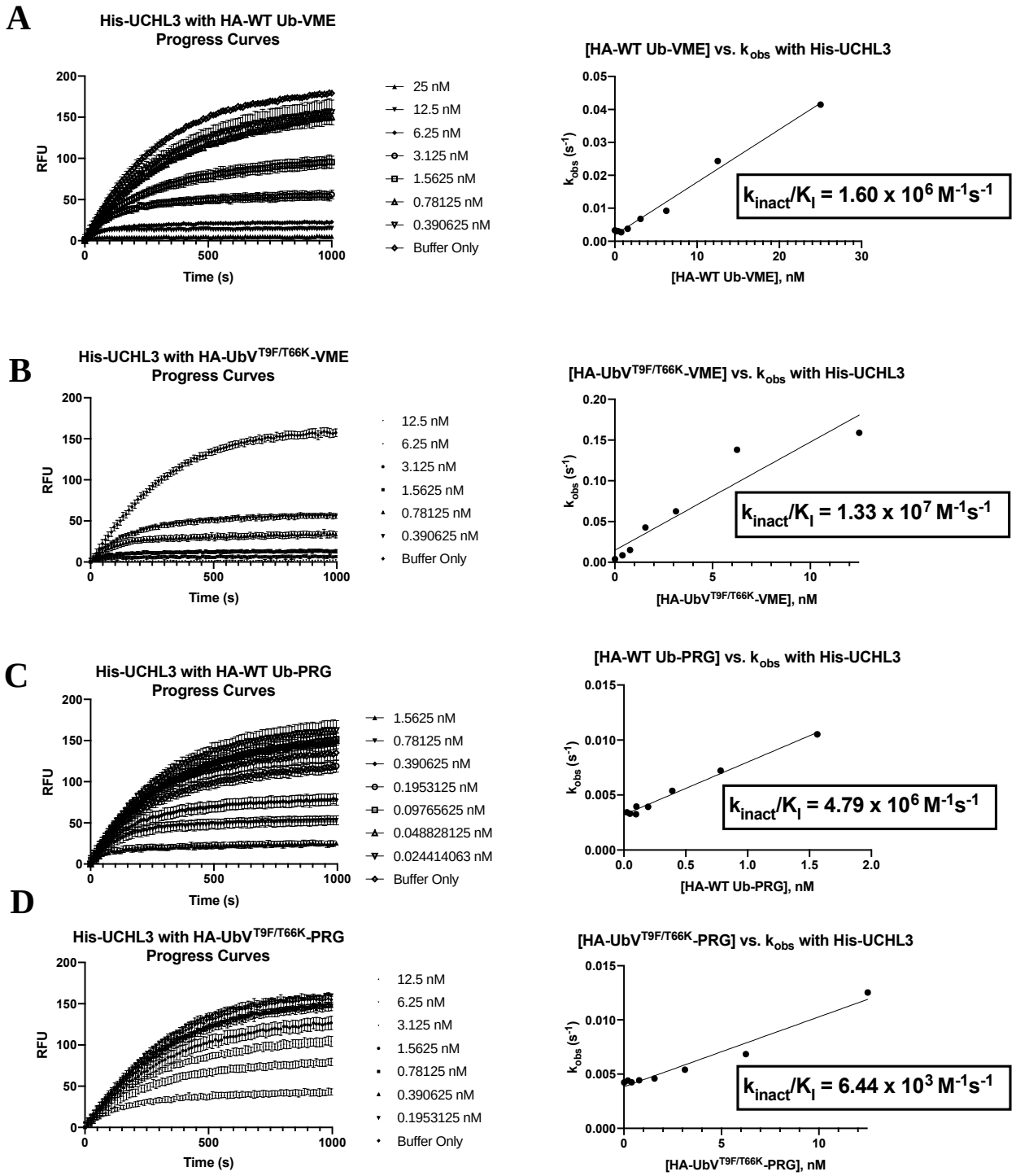

Figure A.22 Progress Curves and k_{inact}/K_I Data for His-UCHL3 with A) HA-WT Ub-VME, B) HA-UbV$^{T9F/T66K}$-VME, C) HA-WT Ub-PRG, and D) HA-UbV$^{T9F/T66K}$-PRG

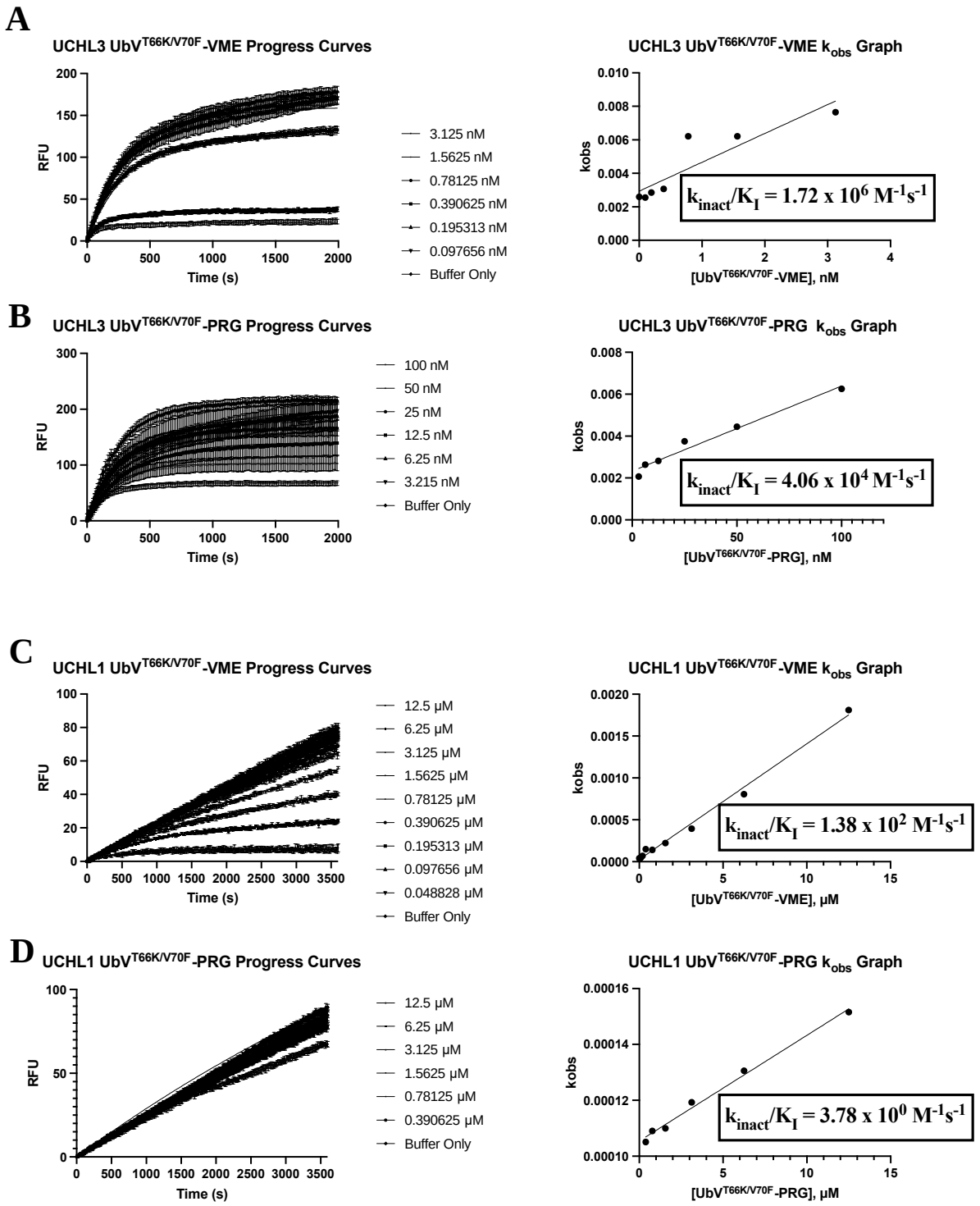

Figure A.23 Progress Curves for UbV$^{T66K/V70F}$-ABPs for His-UCHL3 and His-UCHL1 with A) UCHL3 with HA-UbV$^{T66K/V70F}$-VME, B) UCHL3 with HA-UbV$^{T66K/V70F}$-PRG C) UCHL1 with HA-UbV$^{T66K/V70F}$-VME, D) UCHL1 with HA-UbV$^{T66K/V70F}$-PRG

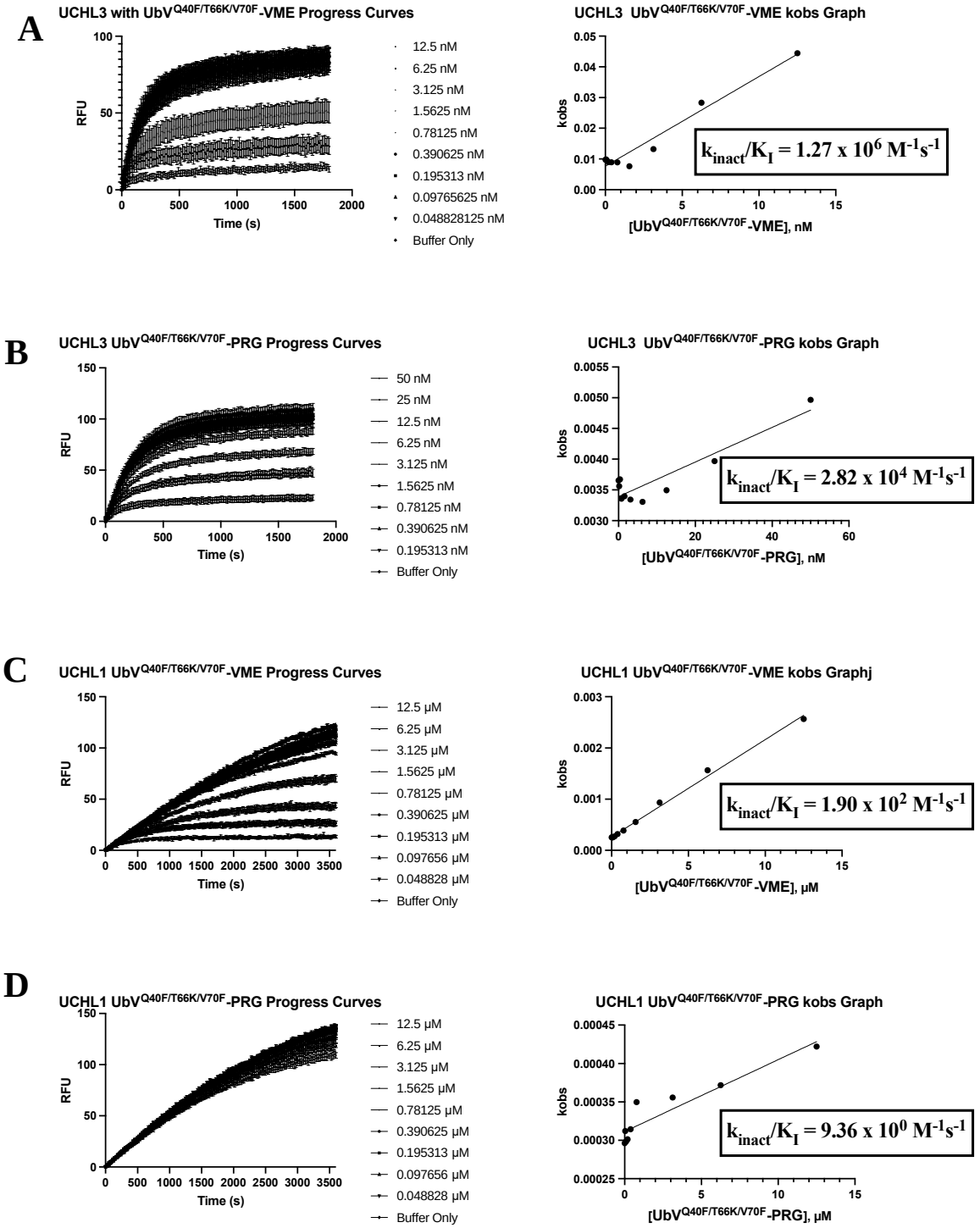

Figure A.24 Progress Curves for UbV$^{Q40F/T66K/V70F}$-ABPs for His-UCHL3 and His-UCHL1 with A) UCHL3 with HA-UbV$^{Q40F/T66K/V70F}$-VME, B) UCHL3 with HA- UbV$^{Q40F/T66K/V70F}$-PRG C) UCHL1 with HA- UbV$^{Q40F/T66K/V70F}$-VME, D) UCHL1 with HA- UbV$^{Q40F/T66K/V70F}$-PRG.

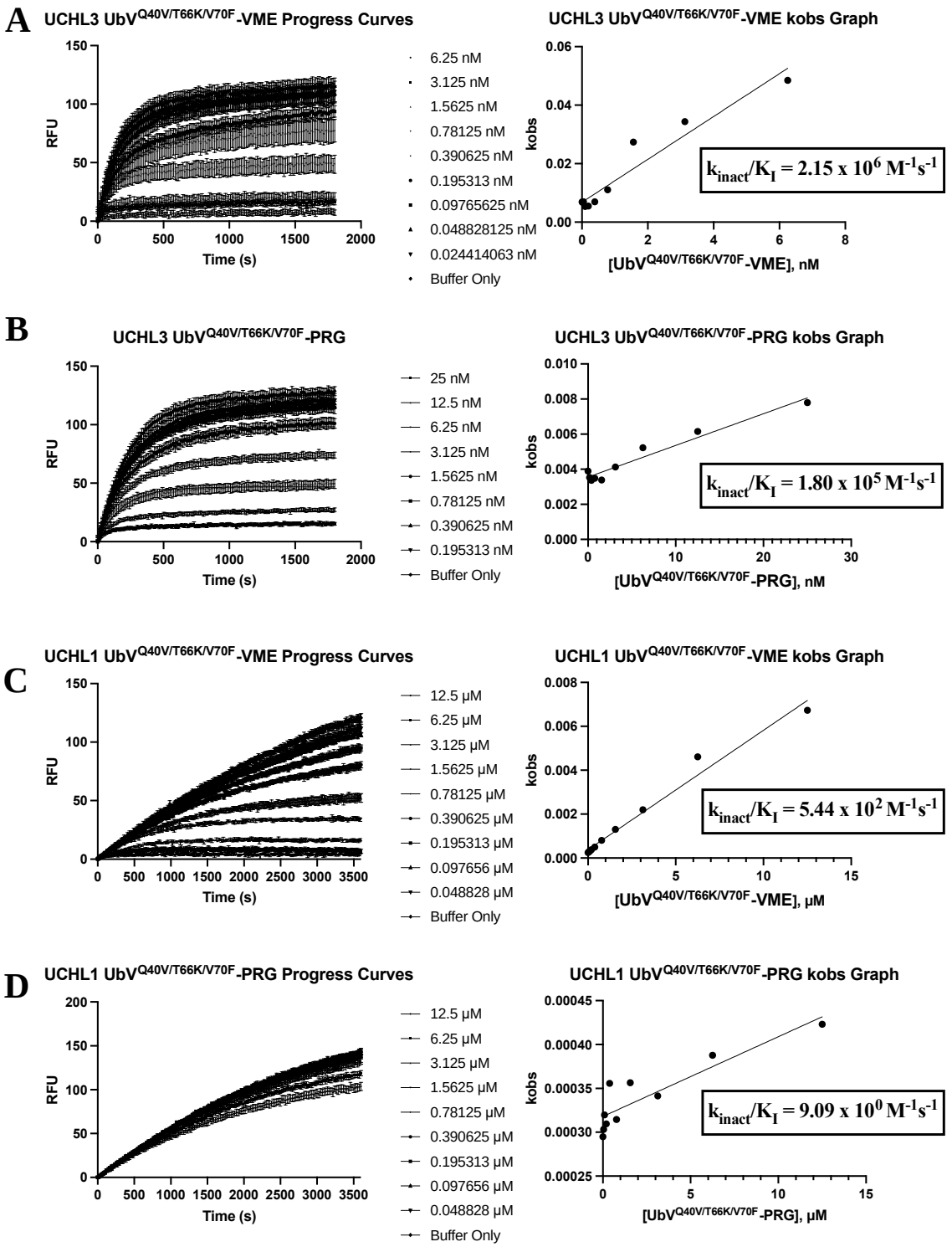

Figure A.25 Progress Curves for UbV$^{Q40V/T66K/V70F}$-ABPs for His-UCHL3 and His-UCHL1 with A) UCHL3 with HA-UbV$^{Q40V/T66K/V70F}$-VME, B) UCHL3 with HA- UbV$^{Q40V/T66K/V70F}$-PRG C) UCHL1 with HA- UbV$^{Q40V/T66K/V70F}$-VME, D) UCHL1 with HA- UbV$^{Q40V/T66K/V70F}$-PRG.

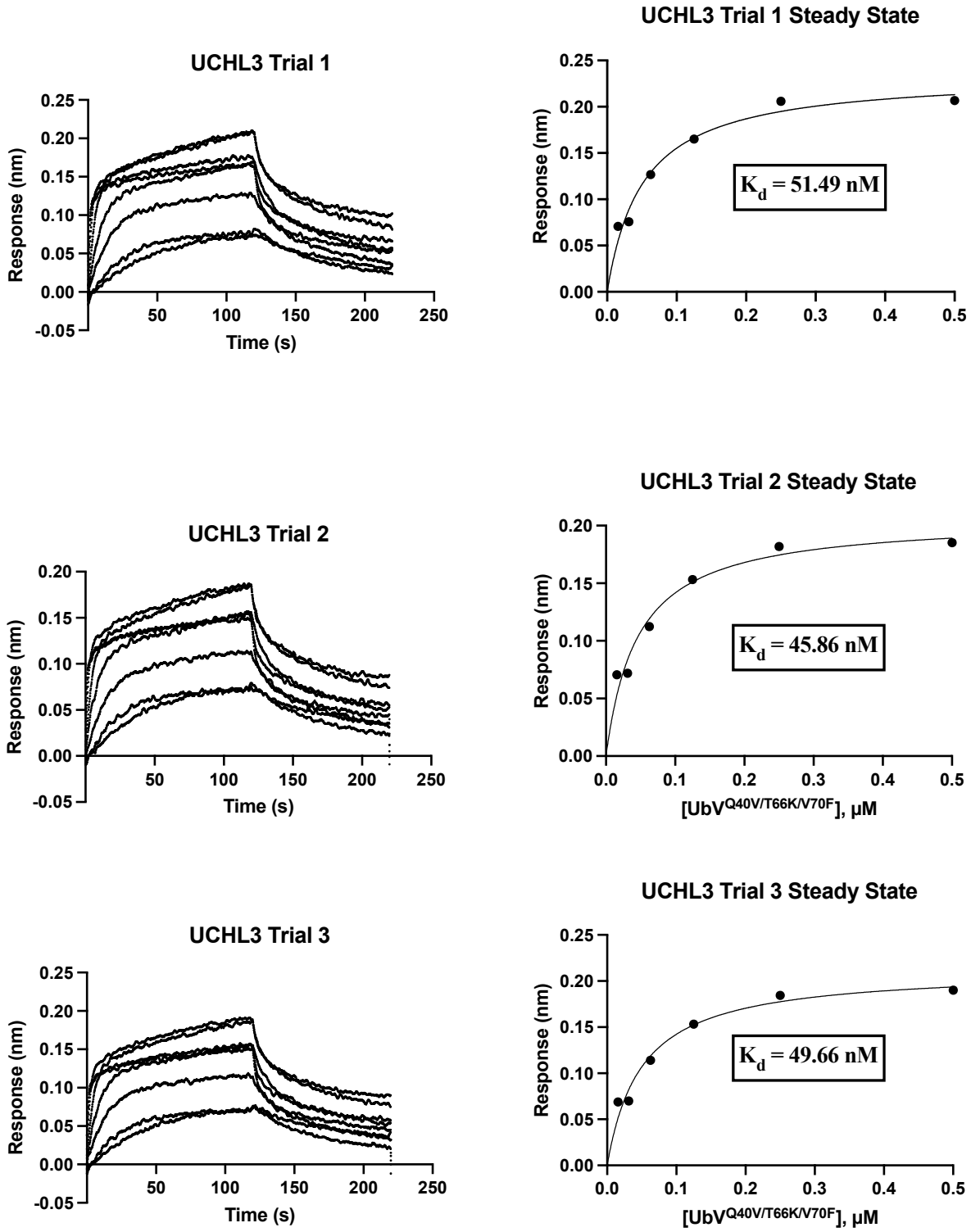

Figure A.26 A) Biolayer Interferometry Association/Dissociation and Steady State Binding Curves for $UbV^{Q40V/T66K/V70F}$ Binding to His-UCHL3. Individual points were averaged values from 110s-115s of the association step for each trial. K_ds determined by fitting to a 1:1 binding model in Prism 8. $UbV^{Q40V/T66K/V70F}$ association lasted for 120 seconds and subsequently dissociated for 100 seconds. Data subtracted from baseline sensogram containing 1x PBS 0.05% v/v Tween 20 with 0.1% w/v BSA (buffer only) wells in loading, association, dissociation, and buffer containing wells.

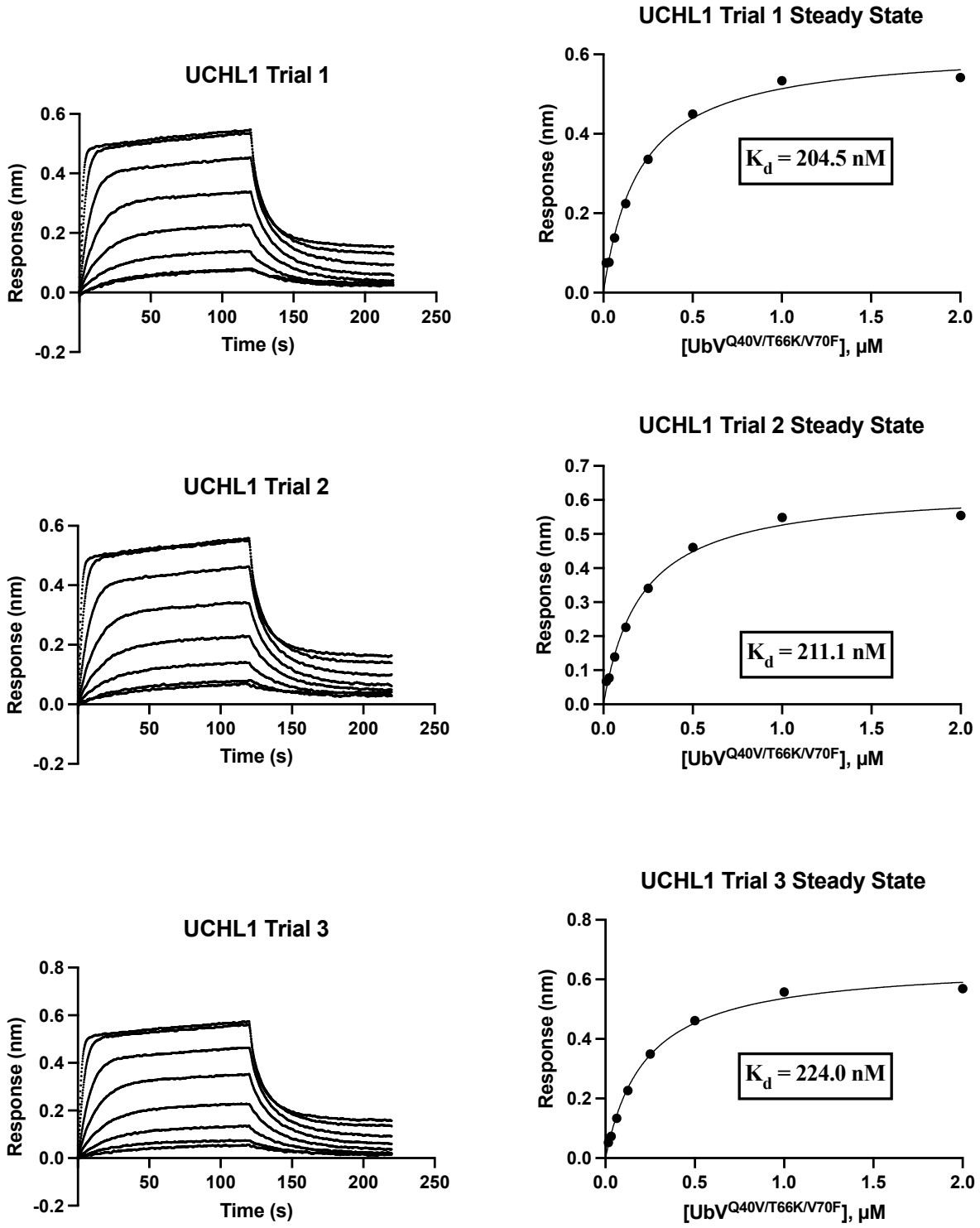

Figure A.27 A) Biolayer Interferometry Association/Dissociation and Steady State Binding Curves for UbV$^{Q40V/T66K/V70F}$ Binding to His-UCHL1. Individual points were averaged values from 110s-115s of the association step for each trial. K_ds determined by fitting to a 1:1 binding model in Prism 8. UbV$^{Q40V/T66K/V70F}$ association lasted for 120 seconds and subsequently dissociated for 100 seconds. Data subtracted from baseline sensorgram containing 1x PBS 0.05% v/v Tween 20 with 0.1% w/v BSA (buffer only) wells in loading, association, dissociation, and buffer containing wells.

REFERENCES

1. Haas, A. L. & Rose, I. A. The mechanism of ubiquitin activating enzyme. A kinetic and equilibrium analysis. *J. Biol. Chem.* **257**, 10329–10337 (1982).

2. Hershko, A., Heller, H., Elias, S. & Ciechanover, A. Components of ubiquitin-protein ligase system. Resolution, affinity purification, and role in protein breakdown. *J. Biol. Chem.* **258**, 8206–8214 (1983).

3. Haas, A. L., Warms, J. V., Hershko, A. & Rose, I. A. Ubiquitin-activating enzyme. Mechanism and role in protein-ubiquitin conjugation. *J. Biol. Chem.* **257**, 2543–2548 (1982).

4. Kulathu, Y. & Komander, D. Atypical ubiquitylation-the unexplored world of polyubiquitin beyond Lys48 and Lys63 linkages. *Nat. Rev. Mol. Cell Biol.* **13**, 508–523 (2012).

5. Pickart, C. M. Targeting of substrates to the 26S proteasome. *FASEB J.* **11**, 1055–1066 (1997).

6. Zhao, Y., Brickner, J. R., Majid, M. C. & Mosammaparast, N. Crosstalk between ubiquitin and other post-translational modifications on chromatin during double-strand break repair. *Trends Cell Biol.* **24**, 426–434 (2014).

7. Xia, Z. P. *et al.* Direct activation of protein kinases by unanchored polyubiquitin chains. *Nature* **461**, 114–119 (2009).

8. French, M. E., Koehler, C. F. & Hunter, T. Emerging functions of branched ubiquitin chains. *Cell Discov.* **7**, 6 (2021).

9. Ohtake, F., Saeki, Y., Ishido, S., Kanno, J. & Tanaka, K. The K48-K63 Branched Ubiquitin Chain Regulates NF-κB Signaling. *Mol. Cell* **64**, 251–266 (2016).

10. Vijay-Kumar, S. Bugg, C. E., & Cook, W.J. Structure of ubiquitin refined at 1.8Å resolution. *J. Mol. Biol.* **194,** 531-544 (1987)

11. Cook, W. J., Jeffrey, L. C., Carson, M., Chen, Z. & Pickart, C. M. Structure of a diubiquitin conjugate and a model for interaction with ubiquitin conjugating enzyme (E2). *J. Biol. Chem.* **267**, 16467–16471 (1992).

12. Tenno, T. *et al.* Structural basis for distinct roles of Lys63- and Lys48-linked polyubiquitin chains. *Genes to Cells* **9**, 865–875 (2004).

13. Varadan, R., Walker, O., Pickart, C. & Fushman, D. Structural properties of polyubiquitin chains in solution. *J. Mol. Biol.* **324**, 637–647 (2002).

14. Eddins, M. J., Varadan, R., Fushman, D., Pickart, C. M. & Wolberger, C. Crystal Structure and Solution NMR Studies of Lys48-linked Tetraubiquitin at Neutral pH. *J. Mol. Biol.* **367**, 204–211 (2007).

15. Bremm, A., Freund, S. M. V. & Komander, D. Lys11-linked ubiquitin chains adopt compact conformations and are preferentially hydrolyzed by the deubiquitinase Cezanne. *Nat. Struct. Mol. Biol.* **17**, 939–947 (2010).

16. Matsumoto, M. L. *et al.* K11-linked polyubiquitination in cell cycle control revealed by a K11 linkage-specific antibody. *Mol. Cell* **39**, 477–484 (2010).

17. Virdee, S., Ye, Y., Nguyen, D. P., Komander, D. & Chin, J. W. Engineered diubiquitin synthesis reveals Lys29-isopeptide specificity of an OTU deubiquitinase. *Nat. Chem. Biol.* **6**, 750–757 (2010).

18. Varadan, R. *et al.* Solution Conformation of Lys63-linked Di-ubiquitin Chain Provides Clues to Functional Diversity of Polyubiquitin Signaling. *J. Biol. Chem.* **279**, 7055–7063 (2004).

19. Komander, D. *et al.* Molecular discrimination of structurally equivalent Lys 63-linked and linear polyubiquitin chains. *EMBO Rep.* **10**, 466–473 (2009).

20. Sims, J. J. & Cohen, R. E. Linkage-Specific Avidity Defines the Lysine 63-Linked Polyubiquitin-Binding Preference of Rap80. *Mol. Cell* **33**, 775–783 (2009).

21. Hewings, D. S., Flygare, J. A., Bogyo, M. & Wertz, I. E. Activity-based probes for the ubiquitin conjugation–deconjugation machinery: new chemistries, new tools, and new insights. *FEBS J.* **284**, 1555–1576 (2017).

22. Kwasna, D. *et al.* Discovery and Characterization of ZUFSP/ZUP1, a Distinct Deubiquitinase Class Important for Genome Stability. *Mol. Cell* **70**, 150-164.e6 (2018).

23. Abdul Rehman, S. A. *et al.* MINDY-1 Is a Member of an Evolutionarily Conserved and Structurally Distinct New Family of Deubiquitinating Enzymes. *Mol. Cell* **63**, 146–155 (2016).

24. Faesen, A. C. *et al.* The differential modulation of USP activity by internal regulatory domains, interactors and eight ubiquitin chain types. *Chem. Biol.* **18**, 1550–1561 (2011).

25. Ritorto, M. S. *et al.* Screening of DUB activity and specificity by MALDI-TOF mass spectrometry. *Nat. Commun.* **5**, (2014).

26. Cooper, E. M. *et al.* K63-specific deubiquitination by two JAMM/MPN+ complexes: BRISC-associated Brcc36 and proteasomal Poh1. *EMBO J.* **28**, 621–631 (2009).

27. Zhou, Z. R., Zhang, Y. H., Liu, S., Song, A. X. & Hu, H. Y. Length of the active-site crossover loop defines the substrate specificity of ubiquitin C-terminal hydrolases for ubiquitin chains. *Biochem. J.* **441**, 143–149 (2012).

28. Wilkinson, K. D. *et al.* The neuron-specific protein PGP 9.5 is a ubiquitin carboxyl-terminal hydrolase. *Science (80-.).* **246**, 670–673 (1989).

29. Bishop, P., Rocca, D. & Henley, J. M. Ubiquitin C-Terminal hydrolase L1 (UCH-L1): Structure, distribution and roles in brain function and dysfunction. *Biochem. J.* **473**, 2453–2462 (2016).

30. Boudreaux, D. A., Maiti, T. K., Davies, C. W. & Das, C. Ubiquitin vinyl methyl ester binding orients the misaligned active site of the ubiquitin hydrolase UCHL1 into productive conformation. *Proc. Natl. Acad. Sci. U. S. A.* **107**, 9117–9122 (2010).

31. Hewitt, C. S., Krabill, A. D., Das, C. & Flaherty, D. P. Development of Ubiquitin Variants with Selectivity for Ubiquitin C-Terminal Hydrolase Deubiquitinases. *Biochemistry* **59**, 37, 3447-3462 (2020).

32. Bilguvar, K. *et al.* Recessive loss of function of the neuronal ubiquitin hydrolase UCHL1 leads to early-onset progressive neurodegeneration. *Proc. Natl. Acad. Sci. U. S. A.* **110**, 3489–3494 (2013).

33. Andersson, F. I. *et al.* The effect of Parkinson's-disease-associated mutations on the deubiquitinating enzyme UCH-L1. *J. Mol. Biol.* **407**, 261–272 (2011).

34. Leroy, E. *et al.* The ubiquitin pathway in Parkinson's disease. *Nature* **395**, 451–452 (1998).

35. Setsuie, R. *et al.* Dopaminergic neuronal loss in transgenic mice expressing the Parkinson's disease-associated UCH-L1 I93M mutant. *Neurochem. Int.* **50**, 119–129 (2007).

36. Yasuda, T. *et al.* Effects of UCH-L1 on α-synuclein over-expression mouse model of Parkinson's disease. *J. Neurochem.* **108**, 932–944 (2009).

37. Zetterberg, M. *et al.* Ubiquitin carboxy-terminal hydrolase L1 (UCHL1) S18Y polymorphism in Alzheimer's disease. *Mol. Neurodegener.* **5**, 1–5 (2010).

38. Liu, H. *et al.* The point mutation UCH-L1 C152A protects primary neurons against cyclopentenone prostaglandin-induced cytotoxicity: Implications for post-ischemic neuronal injury. *Cell Death Dis.* **6**, 1–11 (2015).

39. Kabuta, T. *et al.* Aberrant molecular properties shared by familial Parkinson's disease-associated mutant UCH-L1 and carbonyl-modified UCH-L1. *Hum. Mol. Genet.* **17**, 1482–1496 (2008).

40. Nijman, S. M. B. *et al.* A genomic and functional inventory of deubiquitinating enzymes. *Cell* **123**, 773–786 (2005).

41. Zhang, Y. *et al.* Conformational stabilization of ubiquitin yields potent and selective inhibitors of USP7. *Nat Chem Biol.* **9**, 51-58 (2013).

42. Sanchez-Diaz, P. C. *et al.* Ubiquitin carboxyl-Terminal esterase L1 (UCHL1) is associated with stem-like cancer cell functions in pediatric high-grade glioma. *PLoS One* **12**, 1–19 (2017).

43. Bedekovics, T., Hussain, S., Feldman, A. L. & Galardy, P. J. UCH-L1 is induced in germinal center B cells and identifies patients with aggressive germinal center diffuse large B-cell lymphoma. *Blood* **127**, 1564–1574 (2016).

44. Hussain, S. *et al.* The de-ubiquitinase UCH-L1 is an oncogene that drives the development of lymphoma in vivo by deregulating PHLPP1 and Akt signaling. *Leukemia* **24**, 1641–1655 (2010).

45. Hibi, K. *et al.* PGP9.5 As a candidate tumor marker for non-small-cell lung cancer. *Am. J. Pathol.* **155**, 711–715 (1999).

46. Chen, G. *et al.* Proteomic analysis of lung adenocarcinoma: Identification of a highly expressed set of proteins in tumors. *Clin. Cancer Res.* **8**, 2298–2305 (2002).

47. Hussain, S. *et al.* UCH-L1 bypasses mTOR to promote protein biosynthesis and is required for MYC driven lymphomagenesis in mice. *Blood* **132**, blood-2018-05-848515 (2018).

48. Goto, Y. *et al.* UCHL1 provides diagnostic and antimetastatic strategies due to its deubiquitinating effect on HIF-1α. *Nat. Commun.* **6**, 6153 (2015).

49. Hussain, S. *et al.* Ubiquitin Hydrolase UCH-L1 Destabilizes mTOR Complex 1 by Antagonizing DDB1-CUL4-Mediated Ubiquitination of Raptor. *Mol. Cell. Biol.* **33**, 1188–1197 (2013).

50. Luo, Y. *et al.* UCHL1 promotes invasion of breast cancer cells through activating Akt signlaing pathway. **119**, 691–700 (2017).

51. Kim, H. J. *et al.* Ubiquitin C-terminal hydrolase-L1 increases cancer cell invasion by modulating hydrogen peroxide generated via NADPH oxidase 4. *Oncotarget* **6**, 16287–16303 (2015).

52. Jin, C. *et al.* UCHL1 is a putative tumor suppressor in ovarian cancer cells and contributes to cisplatin resistance. *J. Cancer* **4**, 662–670 (2013).

53. Tangri, A. *et al.* Deubiquitinase UCHL1 maintains protein homeostasis through the PSMA7–APEH–Proteasome axis in high-grade serous ovarian carcinoma. *Mol. Cancer Res.* **19**, 1168–1181 (2021).

54. Ummanni, R. *et al.* Ubiquitin carboxyl-terminal hydrolase 1 (UCHL1) is a potential tumour suppressor in prostate cancer and is frequently silenced by promoter methylation. *Mol. Cancer* **10**, 1–13 (2011).

55. Jang, M. J., Baek, S. H. & Kim, J. H. UCH-L1 promotes cancer metastasis in prostate cancer cells through EMT induction. *Cancer Lett.* **302**, 128–135 (2011).

56. Liu, Y. *et al.* Discovery of Inhibitors that Elucidate the Role of UCH-L1 Activity in the H1299 Lung Cancer Cell Line. **10**, 837–846 (2003).

57. L, C. H. *et al.* Optimization and Anti-Cancer Properties of. (2021).

58. Mermerian, A. H., Case, A., Stein, R. L. & Cuny, G. D. Structure-activity relationship, kinetic mechanism, and selectivity for a new class of ubiquitin C-terminal hydrolase-L1 (UCH-L1) inhibitors. *Bioorganic Med. Chem. Lett.* **17**, 3729–3732 (2007).

59. Davies, C. W. *et al.* The co-crystal structure of ubiquitin carboxy-terminal hydrolase L1 (UCHL1) with a tripeptide fluoromethyl ketone (Z-VAE(OMe)-FMK). *Bioorganic Med. Chem. Lett.* **22**, 3900–3904 (2012).

60. Krabill, A. D. *et al.* Ubiquitin C-Terminal Hydrolase L1: Biochemical and Cellular Characterization of a Covalent Cyanopyrrolidine-Based Inhibitor. *ChemBioChem.* **21**, 712–722 (2020).

61. Panyain, N. *et al.* Discovery of a potent and selective covalent inhibitor and activity-based probe for the deubiquitylating enzyme UCHL1, with anti-fibrotic activity. *J. Am. Chem. Soc.* **142**, 12020–12026 (2020).

62. Jones, A. *et al.* Patent Number WO 2016/046530 A1. (2016).

63. Kemp, M., Stockley, M. & Jones, A. Preparation of cyanopyrrolidines as DUB inhibitors for the treatment of cancer. (2017).

64. Misaghi, S. *et al.* Structure of the ubiquitin hydrolase UCH-L3 complexed with a suicide substrate. *J. Biol. Chem.* **280**, 1512–1520 (2005).

65. Johnston, S. C., Larsen, C. N., Cook, W. J., Wilkinson, K. D. & Hill, C. P. Crystal structure of a deubiquitinating enzyme (human UCH-L3) at 1.8 Å resolution. *EMBO J.* **16**, 3787–3796 (1997).

66. Liao, C. *et al.* UCHL3 Regulates Topoisomerase-Induced Chromosomal Break Repair by Controlling TDP1 Proteostasis. *Cell Rep.* **23**, 3352–3365 (2018).

67. Nishi, R. *et al.* The deubiquitylating enzyme UCHL3 regulates Ku80 retention at sites of DNA damage. *Sci. Rep.* **8**, 1–15 (2018).

68. Yang, R. *et al.* GIAT4RA functions as a tumor suppressor in non-small cell lung cancer by counteracting Uchl3–mediated deubiquitination of LSH. *Oncogene* **38**, 7133–7145 (2019).

69. Luo, K. *et al.* A phosphorylation–deubiquitination cascade regulates the BRCA2–RAD51 axis in homologous recombination. *Genes Dev.* **30**, 2581–2595 (2016).

70. Song, Z. *et al.* UCHL3 promotes pancreatic cancer progression and chemo-resistance through FOXM1 stabilization. *Am. J. Cancer Res.* **9**, 1970–1981 (2019).

71. Zhang, M. H. *et al.* UCHL3 promotes ovarian cancer progression by stabilizing TRAF2 to activate the NF-κB pathway. *Oncogene* **39**, 322–333 (2020).

72. Song, Z. *et al.* A novel UCHL3 inhibitor, perifosine, enhances PARP inhibitor cytotoxicity through inhibition of homologous recombination-mediated DNA double strand break repair. *Cell Death Dis.* **10**, (2019).

73. Gills, J. J. & Dennis, P. A. Perifosine: Update on a novel Akt inhibitor. *Curr. Oncol. Rep.* **11**, 102–110 (2009).

74. Ndubaku, C. & Tsui, V. Inhibiting the deubiquitinating enzymes (DUBs). *J. Med. Chem.* **58**, 1581–1595 (2015).

75. Harrigan, J. A., Jacq, X., Martin, N. M. & Jackson, S. P. Deubiquitylating enzymes and drug discovery: Emerging opportunities. *Nat. Rev. Drug Discov.* **17**, 57–77 (2018).

76. Schauer, N. J., Magin, R. S., Liu, X., Doherty, L. M. & Buhrlage, S. J. Advances in Discovering Deubiquitinating Enzyme (DUB) Inhibitors. *J. Med. Chem.* **63**, 2731–2750 (2020).

77. Ernst, A. *et al.* A Strategy for Modulation of Enzymes in the Ubiquitin System. **209**, 590–596 (2013).

78. Leung, I., Jarvik, N. & Sidhu, S. S. A Highly Diverse and Functional Naïve Ubiquitin Variant Library for Generation of Intracellular Affinity Reagents. *J. Mol. Biol.* **429**, 115–127 (2017).

79. Tencer, A. H., Liang, Q. & Zhuang, Z. Divergence in Ubiquitin Interaction and Catalysis among the Ubiquitin-Specific Protease Family Deubiquitinating Enzymes. *Biochemistry* **55**, 4708–4719 (2016).

80. Zhang, W. *et al.* Generation and Validation of Intracellular Ubiquitin Variant Inhibitors for USP7 and USP10. *J. Mol. Biol.* **429**, 3546–3560 (2017).

81. Teyra, J. *et al.* Structural and Functional Characterization of Ubiquitin Variant Inhibitors of USP15. *Structure* **27**, 590-605.e5 (2019).

82. Gjonaj, L. *et al.* USP7: Combining tools towards selectivity. *Chem. Commun.* **55**, 5075–5078 (2019).

83. Borodovsky, A. *et al.* A novel active site-directed probe specific for deubiquitylating enzymes reveals proteasome association of USP14. *EMBO J.* **20**, 5187–5196 (2001).

84. Borodovsky, A. *et al.* Chemistry-based functional proteomics reveals novel members of the deubiquitinating enzyme family. *Chem. Biol.* **9**, 1149–1159 (2002).

85. de Jong, A. *et al.* Ubiquitin-Based Probes Prepared by Total Synthesis To Profile the Activity of Deubiquitinating Enzymes. *ChemBioChem* **13**, 2251–2258 (2012).

86. Ekkebus, R. *et al.* On terminal alkynes that can react with active-site cysteine nucleophiles in proteases. *J. Am. Chem. Soc.* **135**, 2867–2870 (2013).

87. Gilberto, S. & Peter, M. Dynamic ubiquitin signaling in cell cycle regulation. *J. Cell Biol.* **216**, 2259–2271 (2017).

88. Akutsu, M., Dikic, I. & Bremm, A. Ubiquitin chain diversity at a glance. *J Cell Sci* **129**, 875–880 (2016).

89. Heideker, J. & Wertz, I. E. DUBs, the regulation of cell identity and disease. *Biochem. J.* **465**, 1–26 (2015).

90. Frias-Staheli, N. *et al.* Ovarian tumor domain-containing viral proteases evade ubiquitin- and ISG15-dependent innate immune responses. *Cell Host Microbe* **2**, 404–416 (2007).

91. Edelmann, M. J., Nicholson, B. & Kessler, B. M. Pharmacological targets in the ubiquitin system offer new ways of treating cancer, neurodegenerative disorders and infectious diseases. *Expert Rev. Mol. Med.* **13**, (2011).

92. Sheng, Y. *et al.* Molecular recognition of p53 and MDM2 by USP7/HAUSP. *Nat. Struct. Mol. Biol.* **13**, 285 (2006).

93. Fraile, J. M., Quesada, V., Rodríguez, D., Freije, J. M. P. & López-Otín, C. Deubiquitinases in cancer: new functions and therapeutic options. *Oncogene* **31**, 2373–2388 (2012).

94. Hussain, S., Zhang, Y. & Galardy, P. DUBs and cancer: The role of deubiquitinating enzymes as oncogenes, non-oncogenes and tumor suppressors. *Cell Cycle* **8**, 1688–1697 (2009).

95. Hewings, D. S. *et al.* Reactive-site-centric chemoproteomics identifies a distinct class of deubiquitinase enzymes. *Nat. Commun.* **9**, 1162 (2018).

96. Bishop, P., Rocca, D. & Henley, J. M. Ubiquitin C-terminal hydrolase L1 (UCH-L1): structure, distribution and roles in brain function and dysfunction. *Biochem. J.* **473**, 2453–2462 (2016).

97. Kabuta, T., Furuta, A., Aoki, S., Furuta, K. & Wada, K. Aberrant interaction between Parkinson disease-associated mutant UCH-L1 and the lysosomal receptor for chaperone-mediated autophagy. *J. Biol. Chem.* **283**, 23731–23738 (2008).

98. Choi, J. *et al.* Oxidative Modifications and Down-regulation of Ubiquitin Carboxyl-terminal Hydrolase L1 Associated with Idiopathic Parkinson's and Alzheimer's Diseases. *J. Biol. Chem.* **279**, 13256–13264 (2004).

99. Zhang, M., Cai, F., Zhang, S., Zhang, S. & Song, W. Overexpression of ubiquitin carboxyl-terminal hydrolase L1 (UCHL1) delays Alzheimer's progression in vivo. *Sci. Rep.* **4**, 7298 (2015).

100. Xue, S. & Jia, J. Genetic association between Ubiquitin Carboxy-terminal Hydrolase-L1 gene S18Y polymorphism and sporadic Alzheimer's disease in a Chinese Han population. *Brain Res.* **1087**, 28–32 (2006).

101. Öhrfelt, A. *et al.* Increased Cerebrospinal Fluid Levels of Ubiquitin Carboxyl-Terminal Hydrolase L1 in Patients with Alzheimer's Disease. *Dement. Geriatr. Cogn. Dis. Extra* **6**, 283–294 (2016).

102. Kim, H. J. *et al.* Ubiquitin C-terminal hydrolase-L1 is a key regulator of tumor cell invasion and metastasis. *Oncogene* **28**, 117–127 (2009).

103. Panyain, N. *et al.* Discovery of a potent and selective covalent inhibitor and activity-based probe for the deubiquitylating enzyme UCHL1, with anti-fibrotic activity. *J. Am. Chem. Soc.* (2020).

104. Ndubaku, C. & Tsui, V. Inhibiting the deubiquitinating enzymes (DUBs). *J. Med. Chem.* **58**, 1581–1595 (2015).

105. Reyes Turcu, F. E., H., V. K. & D., W. K. Regulation and Cellular Roles of Ubiquitin Specific Deubiquitinating Enzymes. *Biochem Pharmacol* **78**, 756–765 (2009).

106. Leung, I., Jarvik, N. & Sidhu, S. S. A Highly Diverse and Functional Naïve Ubiquitin Variant Library for Generation of Intracellular Affinity Reagents. *J. Mol. Biol.* **429**, 115–127 (2017).

107. Zhang, W. *et al.* Generation and Validation of Intracellular Ubiquitin Variant Inhibitors for USP7 and USP10. *J. Mol. Biol.* **429**, 3546–3560

108. Zhang, Y. *et al.* Conformational stabilization of ubiquitin yields potent and selective inhibitors of USP7. *Nat. Chem. Biol.* **9**, 51–58 (2013).

109. Boudreaux, D. A., Maiti, T. K., Davies, C. W. & Das, C. Ubiquitin vinyl methyl ester binding orients the misaligned active site of the ubiquitin hydrolase UCHL1 into productive conformation. *Proc. Natl. Acad. Sci.* **107**, 9117–9122 (2010).

110. Misaghi, S. *et al.* Structure of the Ubiquitin Hydrolase UCH-L3 Complexed with a Suicide Substrate *. **280**, 1512–1520 (2005).

111. Hassiepen, U. *et al.* A sensitive fluorescence intensity assay for deubiquitinating proteases using ubiquitin-rhodamine110-glycine as substrate. *Anal. Biochem.* **371**, 201–207 (2007).

112. Buß, O., Rudat, J. & Ochsenreither, K. FoldX as Protein Engineering Tool: Better Than Random Based Approaches? *Comput. Struct. Biotechnol. J.* **16**, 25–33 (2018).

113. Durme, J. Van *et al.* A graphical interface for the FoldX forcefield. **27**, 1711–1712 (2011).

114. Schymkowitz, J. *et al.* The FoldX web server : an online force field. **33**, 382–388 (2005).

115. Liu, Y. & Kuhlman, B. RosettaDesign server for protein design. **34**, 235–238 (2006).

116. Kiel, C., Serrano, L. & Herrmann, C. A detailed thermodynamic analysis of Ras/effector complex interfaces. *J. Mol. Biol.* **340**, 1039–1058 (2004).

117. Szczepek, M. *et al.* Structure-based redesign of the dimerization interface reduces the toxicity of zinc-finger nucleases. *Nat. Biotechnol.* **25**, 786–793 (2007).

118. Eletr, Z. M., Huang, D. T., Duda, D. M., Schulman, B. A. & Kuhlman, B. E2 conjugating enzymes must disengage from their E1 enzymes before E3-dependent ubiquitin and ubiquitin-like transfer. *Nat. Struct. Mol. Biol.* **12**, 933–934 (2005).

119. Broom, A., Jacobi, Z., Trainor, K. & Meiering, E. M. Computational tools help improve protein stability but with a solubility tradeoff. *J. Biol. Chem.* **292**, 14349–14361 (2017).

120. Tian, J., Wu, N., Chu, X. & Fan, Y. Predicting changes in protein thermostability brought about by single- or multi-site mutations. *BMC Bioinformatics* **11**, (2010).

121. Hu, M. *et al.* Crystal structure of a UBP-family deubiquitinating enzyme in isolation and in complex with ubiquitin aldehyde. *Cell* **111**, 1041–1054 (2002).

122. Renatus, M. *et al.* Structural Basis of Ubiquitin Recognition by the Deubiquitinating Protease USP2. *Structure* **14**, 1293–1302 (2006).

123. Hu, M. *et al.* Structure and mechanisms of the proteasome-associated deubiquitinating enzyme USP14. *EMBO J.* **24**, 3747–3756 (2005).

124. Ernst, A. *et al.* A Strategy for Modulation of Enzymes in the Ubiquitin System. *Science (80-.).* **32**, 736–740 (2013).

125. Griffin, P. *et al.* Method for Measuring the Activity of Deubiquitinating Enzymes in Cell Lines and Tissue Samples. *J. Vis. Exp.* 1–7 (2015).

126. Altun, M. *et al.* Activity-based chemical proteomics accelerates inhibitor development for deubiquitylating enzymes. *Chem. Biol.* **18**, 1401–1412 (2011).

127. Love, K. R., Pandya, R. K., Spooner, E. & Ploegh, H. L. Ubiquitin C-terminal electrophiles are activity-based probes for identification and mechanistic study of ubiquitin conjugating machinery. *ACS Chem. Biol.* **4**, 275–287 (2009).

128. Case, A. & Stein, R. L. Mechanistic Studies of Ubiquitin C-Terminal Hydrolase L1. 2443–2452 (2006).

129. Egli, M. & Sarkhel, S. Lone pair-aromatic interactions: To stabilize or not to stabilize. *Acc. Chem. Res.* **40**, 197–205 (2007).

130. Luchansky, S. J., Lansbury, P. T. & Stein, R. L. Substrate Recognition and Catalysis by UCH-L1. *Biochemistry* **45**, 14717–14725 (2006).

131. Krieger, E., Koraimann, G. & Vriend, G. Increasing the precision of comparative models with YASARA NOVA—a self-parameterizing force field. *Proteins Struct. Funct. Bioinforma.* **47**, 393–402 (2002).

132. Resnick, E. *et al.* Rapid Covalent-Probe Discovery by Electrophile-Fragment Screening. *J. Am. Chem. Soc.* **141**, 8951-8968 (2019).

133. Shelley, J. C. *et al.* Epik: a software program for pK a prediction and protonation state generation for drug-like molecules. *J. Comput. Aided. Mol. Des.* **21**, 681–691 (2007).

134. Beard, H., Cholleti, A., Pearlman, D., Sherman, W. & Loving, K. A. Applying physics-based scoring to calculate free energies of binding for single amino acid mutations in protein-protein complexes. *PLoS One* **8**, e82849 (2013).

135. Sirin, S., Pearlman, D. A. & Sherman, W. Physics-based enzyme design: Predicting binding affinity and catalytic activity. *Proteins Struct. Funct. Bioinforma.* **82**, 3397–3409 (2014).

136. Ishida, N. *et al.* Ubiquitylation of Ku80 by RNF126 Promotes Completion of Nonhomologous End Joining-Mediated DNA Repair. *Mol. Cell. Biol.* **37**, e00347-16 (2017).

137. Postow, L. *et al.* Ku80 removal from DNA through double strand break – induced ubiquitylation. **182**, 467–479 (2008).

138. Boudreaux, D. A., Chaney, J., Maiti, T. K. & Das, C. Contribution of active site glutamine to rate enhancement in ubiquitin C-terminal hydrolases. *FEBS J.* **279**, 1106–1118 (2012).

139. Lewis, S. D., Johnson, F. A. & Shafer, J. A. Effect of Cysteine-25 on the Ionization of Histidine-159 in Papain As Determined by Proton Nuclear Magnetic Resonance Spectroscopy. Evidence for a His-159-Cys-25 Ion Pair and Its Possible Role in Catalysis. *Biochemistry* **20**, 48–51 (1981).

140. Morrow, M. E. *et al.* Active site alanine mutations convert deubiquitinases into high-affinity ubiquitin-binding proteins. *EMBO Rep.* **19**, 1–9 (2018).

141. Kattenhorn, L. M., Korbel, G. A., Kessler, B. M., Spooner, E. & Ploegh, H. L. A deubiquitinating enzyme encoded by HSV-1 belongs to a family of cysteine proteases that is conserved across the family Herpesviridae. *Mol. Cell* **19**, 547–557 (2005).

142. Powers, J. C., Asgian, J. L., Ekici, Ö. D. & James, K. E. Irreversible inhibitors of serine, cysteine, and threonine proteases. *Chem. Rev.* **102**, 4639–4750 (2002).

143. Larsen, C. N., Krantz, B. A. & Wilkinson, K. D. Substrate specificity of deubiquitinating enzymes: Ubiquitin C-terminal hydrolases. *Biochemistry* **37**, 3358–3368 (1998).

144. Nakatsu, F. *et al.* A di-leucine signal in the ubiquitin moiety: Possible involvement in ubiqutination-mediated endocytosis. *J. Biol. Chem.* **275**, 26213–26219 (2000).

145. Shih, S. C., Sloper-Mould, K. E. & Hicke, L. Monoubiquitin carries a novel internalization signal that is appended to activated receptors. *EMBO J.* **19**, 187–198 (2000).

146. Osaka, H. *et al.* Ubiquitin carboxy-terminal hydrolase L1 binds to and stabilizes monoubiquitin in neuron. *Hum. Mol. Genet.* **12**, 1945–1958 (2003).

147. Kumar, R. *et al.* S-nitrosylation of UCHL1 induces its structural instability and promotes α-synuclein aggregation. *Sci. Rep.* **7**, 44558 (2017).

148. Koharudin, L. M. I. *et al.* Cyclopentenone prostaglandin-induced unfolding and aggregation of the Parkinson disease-associated UCH-L1. *Proc. Natl. Acad. Sci. U. S. A.* **107**, 6835–6840 (2010).

149. Contu, V. R. *et al.* Endogenous neurotoxic dopamine derivative covalently binds to Parkinson's disease-associated ubiquitin C-terminal hydrolase L1 and alters its structure and function. *J. Neurochem.* **130**, 826–838 (2014).

150. Bishop, P., Rubin, P., Thomson, A. R., Rocca, D. & Henley, J. M. The Ubiquitin C-Terminal Hydrolase L1 (UCH-L1) C terminus plays a key role in protein stability, but its farnesylation is not required for membrane association in primary neurons. *J. Biol. Chem.* **289**, 36140–36149 (2014).

151. Hussain, S. *et al.* A cysteine near the C-terminus of UCH-L1 is dispensable for catalytic activity but is required to promote AKT phosphorylation, eIF4F assembly, and malignant B-cell survival. *Cell Death Discov.* **5**, 1–9 (2019).

152. Nischan, N. *et al.* Covalent attachment of cyclic TAT peptides to GFP results in protein delivery into live cells with immediate bioavailability. *Angew. Chemie - Int. Ed.* **54**, 1950–1953 (2015).

153. Qian, Z. *et al.* Early endosomal escape of a cyclic cell-penetrating peptide allows effective cytosolic cargo delivery. *Biochemistry* **53**, 4034–4046 (2014).

154. Qian, Z. *et al.* Discovery and Mechanism of Highly Efficient Cyclic Cell-Penetrating Peptides. *Biochemistry* **55**, 2601–2612 (2016).

155. Gui, W., Shen, S. & Zhuang, Z. Photocaged Cell-Permeable Ubiquitin Probe for Temporal Profiling of Deubiquitinating Enzymes. *J. Am. Chem. Soc.* **142**, 19493–19501 (2020).

156. Ressler, V. T., Mix, K. A. & Raines, R. T. Esterification Delivers a Functional Enzyme into a Human Cell. *ACS Chem. Biol.* **14**, 599–602 (2019).

157. McGrath, N. A., Andersen, K. A., Davis, A. K. F., Lomax, J. E. & Raines, R. T. Diazo compounds for the bioreversible esterification of proteins. *Chem. Sci.* **6**, 752–755 (2015).

158. Godinat, A. *et al.* A biocompatible 'split luciferin' reaction and its application for non-invasive bioluminescent imaging of protease activity in living animals. *Curr. Protoc. Chem. Biol.* **6**, 169–189 (2014).

159. White, E.H., McCarpa, F., Field, G.F., McElroy, W.D. The structure and synthesis of firefly luciferin. *JACS*. **83**, 2402-2403 (1961).

VITA

Chad Steven Hewitt, son of Steve and Martine Hewitt, was born October 18th, 1993 in Wayzata Minnesota. He was raised in Mound, MN where he graduated from Mound Westonka High School in 2012. Chad went on to the University of St. Thomas where he earned his Bachelor of Science degree majoring in Biochemistry in 2016. Following completion of his degree, he joined the Medicinal Chemistry and Molecular Pharmacology department at Purdue University's College of Pharmacy. In December 2016, he joined Dr. Daniel Flaherty's lab. Chad's work in the Flaherty lab focused on the development and characterization of selective ubiquitin variants for ubiquitin C-terminal hydrolase enzymes (UCHL1 and UCHL3). During his PhD studies, Chad earned the Purdue Graduate School Frederick N. Andrews Fellowship, College of Pharmacy Travel Award, PCCR Travel Award, PGSG Graduate Student Travel Award, and the Chaney Summer Graduate Student Award. In addition to his time in lab, Chad was actively involved in the MCMP graduate student organization as the president and what a member of the College of Pharmacy Graduate Student Council as the MCMP representative. Chad concurrently worked two years at an internship with Purdue Research Foundation Office of Technology Commercialization.

PUBLICATIONS

Nader S. Abutaleb, Alessio Nocentini, **Chad S. Hewitt**, Bruce R. Cooper, Claudiu T. Supuran, Mohamed N. Seleem, Daniel P. Flaherty. Repurposing FDA-Approved Sulfonamide Carbonic Anhydrase Inhibitors for Treatment of Neisseria Gonorrhoeae. J Enzyme Inhib Med Chem. (In Press)

Simone Giovannuzzi, **Chad S. Hewitt**, Fabrizio Carta, Alessio Nocentini, Daniel P. Flaherty, Claudiu T. Supuran. Dithiocarbamates Effectively Inhibit the Alpha Carbonic Anhydrase from Neisseria Gonorrhoeae. J Enzyme Inhib Med Chem. (In Press)

Alessio Nocentini, **Chad S. Hewitt**, Daniel P. Flaherty, Claudiu T. Supeuran. Anion inhibition studies of the α-carbonic anhydrases from Neisseria gonorrhoeae (2021). J Enzyme Inhib Med Chem.

Chad S. Hewitt, Nader S. Abutaleb, Alessio Nocentini, Xufeng Cao, Devon P. Amos, Molly S. Youse, Katrina J. Holly, Anil Marapaka, Weiwei An, Jatinder Kaur, Aaron D. Krabill, Ahmed Elkashif, Amanda L. Graboski, Ahmed Hassan AbdelKhalek, Claudiu T. Supuran, Mohamed N. Seleem, Daniel P. Flaherty Optimization and Antimicrobial Activity of Novel Carbonic Anhydrase Inhibitors to Target Neisseria gonorrhoeae (2021). ACS Infectious Diseases.

Aaron D. Krabill, Hao Chen, Sajjad Hussain, **Chad S. Hewitt**, Ryan D. Imhoff, Chittaranjan Das, Paul J. Galardy, Michael K. Wendt, and Daniel P. Flaherty. Optimization and Anti-Cancer Properties of Fluoromethylketones as Covalent Inhibitors for Ubiquitin C-Terminal Hydrolase L1 (2021). Molecules.

Michael J. Sheedlo, Sebastian Kenny, Ivan Podkorytov, Kwame Brown, Jia Ma, Shalini Iyer, **Chad S. Hewitt**, Trent S. Arbough, Oleg Mikhailovskii, Daniel P. Flaherty, Mark A.Wilson, Nikolai R. Skrynnikov, Chittaranjan Das. Insights into ubiquitin product release in hydrolysis catalyzed by the bacterial deubiquitinase SdeA (2021). Biochemistry.

Chad S. Hewitt, Aaron D. Krabill, Chittaranjan Das, Daniel P. Flaherty. Development of Ubiquitin Variants with Selectivity for Ubiquitin C-Terminal Hydrolase Deubiquitinases (2020). Biochemistry.

Aaron D. Krabill, Hao Chen, Sajjad Hussain, Chao Feng, Ammara Abdullah, **Chad S. Hewitt**, Chittaranjan Das, Uma K. Aryl, Carol Beth Post, Michael K. Wendt, Paul J. Galardy, Daniel P. Flaherty. Ubiquitin C-Terminal Hydrolase L1: Biochemical and Cellular Characterization of a Covalent Cyanopyrrolidine-Based Inhibitor (2019). ChemBioChem.